



NTNU – Trondheim
Norwegian University of
Science and Technology

Wind turbine wake meandering

Susanne Lynum

Master of Energy Use and Energy Planning

Submission date: June 2013

Supervisor: Per-Åge Krogstad, EPT

Norwegian University of Science and Technology
Department of Energy and Process Engineering

EPT-M-2013-78

MASTER THESIS

for

student Susanne Lynum

Spring 2013

Wind turbine wake meandering

*Wake bevegelse bak en vindturbin***Background and objective**

Wind tunnel model tests are very useful in order to verify computer predictions. With access to good experimental data, the modeller may be able to sort out sources of inaccuracy in the model. A direct comparison with experimental data does however require that the experimental data represent the quantities one wishes to check.

For wind turbine predictions it has proven difficult to accurately model the wake behind the rotor. Good measurements exist, but they may not necessarily represent the same quantity as that produced by the predictions. One possible source of error comes from the tendency for the wake to move around in space. When measuring e.g. turbulence in a fixed point in space, this meandering will lead to a smearing out of the steep gradients found in the wake and hence the measured turbulence levels appear to be lower than what is really the case.

In this project we want to find out how important this effect is. Since the wake development is expected to depend on the free stream turbulence, this needs to be varied to see how it affects the smoothing of the data.

The following tasks are to be considered:

- 1) The student should learn to use hot wire anemometry. This may be done by applying the technique to a known flow, e.g. as found in a fully developed pipe flow.
- 2) Using an array of hot wires, simultaneous measurements at multiple nearby points in the wake of a wind turbine should be used to study the meandering of the wake.
- 3) After initial measurements in a low turbulence incoming flow, the measurements should be repeated for a flow that has a free stream turbulence intensity that is typical for atmospheric turbulence.

Within 14 days of receiving the written text on the master thesis, the candidate shall submit a research plan for his project to the department.

When the thesis is evaluated, emphasis is put on processing of the results, and that they are presented in tabular and/or graphic form in a clear manner, and that they are analyzed carefully.

The thesis should be formulated as a research report with summary both in English and Norwegian, conclusion, literature references, table of contents etc. During the preparation of the text, the candidate should make an effort to produce a well-structured and easily readable report. In order to ease the evaluation of the thesis, it is important that the cross-references are correct. In the making of the report, strong emphasis should be placed on both a thorough discussion of the results and an orderly presentation.

The candidate is requested to initiate and keep close contact with his/her academic supervisor(s) throughout the working period. The candidate must follow the rules and regulations of NTNU as well as passive directions given by the Department of Energy and Process Engineering.

Risk assessment of the candidate's work shall be carried out according to the department's procedures. The risk assessment must be documented and included as part of the final report. Events related to the candidate's work adversely affecting the health, safety or security, must be documented and included as part of the final report. If the documentation on risk assessment represents a large number of pages, the full version is to be submitted electronically to the supervisor and an excerpt is included in the report.

Pursuant to “Regulations concerning the supplementary provisions to the technology study program/Master of Science” at NTNU §20, the Department reserves the permission to utilize all the results and data for teaching and research purposes as well as in future publications.

The final report is to be submitted digitally in DAIM. An executive summary of the thesis including title, student's name, supervisor's name, year, department name, and NTNU's logo and name, shall be submitted to the department as a separate pdf file. Based on an agreement with the supervisor, the final report and other material and documents may be given to the supervisor in digital format.

- Work to be done in lab (Water power lab, Fluids engineering lab, Thermal engineering lab)
 Field work

Department of Energy and Process Engineering, 16. January 2013



Olav Bolland
Department Head



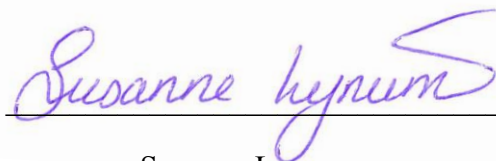
Per-Åge Krogstad
Academic Supervisor

Preference

This master thesis is the last part of the final semester of a two years master's degree in *Energy Use and Energy Planning* at NTNU. The study has been conducted throughout 21 weeks and involved literature research, experiments and analyzing of measurements.

The master thesis main purpose was to study the meandering of the wake of a model wind turbine. This was to be conducted by using an array of hot-wire probes. During this study I ended up with very large amount of data about the wake of model wind turbine, which have been difficult to structure and analyze. One of the main challenges has been to find a correct and foolproof method of analyzing the results. The use of Matlab has also been a challenge, due to my lack of experience with the program. It has also been difficult to narrow down the study since there are numerous ways to explain one singularity. Though, through it all I have learned a great deal about the wake of a wind turbine, turbulence and last, but not at least, Matlab.

I would like to thank my supervisor Per-Åge Krogstad for helpful guidelines and inspiring conversations. Pål Egil Eriksen for motivation and for always being there to help with my frustrations over the use of hot-wire anemometry and experimental setup in the wind tunnel. I would also like to thank Arnt Egil Kolstad for constructing necessary equipment and rigging in the wind tunnel.



Susanne Lynum

10.06.2013 Trondheim

Abstract

In this master thesis the meandering of the wake of a three bladed horizontal axis model wind turbine has been studied. Measurements have been conducted by the use of four hot-wire probes located at multiple nearby points in the wake at $X/D = 1, 3$ and 5 downstream the model wind turbine. The meandering has been studied based on the location of the tip vortices shed by the turbine blades. The experiments were conducted in the wind tunnel at NTNU at the Department of *Energy and Process Engineering*.

The aim of the study was to see the effect on the meandering of the wake of the model turbine when placed in an incoming flow with turbulence intensity typical for atmospheric turbulence, compared to an incoming flow with a low turbulence intensity round 0.3% . The atmospheric turbulence was generated by inserting a grid in the inlet to the test section in the wind tunnel. The grid generated a turbulence intensity round 5.5% and integral length scales of $L_{uuz} = 3.1E-2$ m and $L_{uux} = 6.5E-2$ m at the position of the model wind turbine in the tunnel.

The performance of the model turbine in both incoming flows was calculated based on measurements of the thrust and torque acting on the turbine in a free stream velocity of 10 m/s. The greatest deviation in the performance curve was found at the top of the curve; however the difference between the two cases was minor.

Initial measurements with a single hot-wire probe was conducted in the wake of the turbine to locate the tip vortices. Based on these results, the location to conduct the multiple hot-wire measurements was decided. Already at this stage the effect of the grid turbulence was evident due to the smeared out energy in the flow in the wake caused by diffusion and mixing.

The tip speed ratio (TSR) of the model wind turbine was 6 in the case without grid generated turbulence, and 7 in the case with grid turbulence during the final measurements in the wake. The effect of the change in TSR was evaluated, and it was found that new measurements were not needed. The normal stress based on the velocity measurements in the wake were phase averaged according to the position of the turbine blade using Matlab. When comparing these results with the normal stress calculated directly from the time series, it was found that the tip vortices had merged together or broken up at all measurement point except at $X/D = 1$ downstream the turbine without grid generated turbulence. Using power spectral density function (PSD) the observations were confirmed.

The tip vortices was not equally distributed within the wake and were located $30^\circ, 128^\circ$ and 224° at respectively $z/R = 1.12, 1.15$ and 1.20 . Their diameters were found to be $1.8E-2$ m, $1.4E-2$ m, $2.7E-2$ m in z direction. The location of the peak in the normal stress tended to meander a bit back and forth, mainly directed towards the rotor center, with a distance from $4.5E-3$ m to $1.8E-2$ m, and in the streamwise direction with a total distance of $6.2E-2$ m. The tip vortices seem to meander individually within the wake, and not with the same distance.

Based on the results and observations conducted throughout this study, new measurements should be conducted at a shorter distance to the turbine rotor to be able to compare the meandering of the wake for the two different incoming flows.

Sammendrag

I denne master oppgaven har wake bevegelsen bak en tre-bladet horisontalakset vindturbinmodell blitt studert. Det har blitt utført målinger ved bruk av fire hot-wire prober plassert ved flere nærliggende punkter i waken ved $X/D = 1, 3$ og 5 nedstrøms i waken til vindturbinmodellen. Wake bevegelsen har blitt studert basert på plasseringen av tuppvirvlene kastet av turbin bladene. Eksperimentene har blitt utført i vindtunnelen på NTNU ved instituttet for *Energi- og Prosessteknikk*.

Målet for studiet var å se på effekten av vandringen til waken av en vindturbinmodell som står plassert i en strømning med en turbulensintensitet typisk for atmosfærisk turbulens, og sammenligne med en strømning med lav turbulensintensitet på rundt $0,3\%$. Den atmosfæriske turbulensen ble generert ved å installere et grid i innløpet til testseksjonen i vindtunnelen. Griddet genererte en turbulensintensitet på rundt $5,5\%$ og en integrallengdeskala på $L_{uuz} = 3,1E-2$ m and $L_{uux} = 6,5E-2$ m ved posisjonen til vindturbinen i tunellen.

Ytelsen til vindturbinmodellen ble beregnet for begge strømningene basert på målinger av skyvekraften og dreiemomentet som virket på turbinen med en fristrømhastighet på 10 m/s. Det var en liten forskjell mellom kurvene, og det største avviket i ytelseskurven ble funnet rundt toppen av kurven.

Det ble utført innledende målinger med en enkelt hot-wire probe i waken til turbinen for å lokalisere tuppvirvlene. Basert på disse resultatene ble det bestemt hvor de multiple hot-wiremålingene skulle utføres i waken. Allerede ved dette tidspunktet var det tydelig at gridturbulensen hadde smurt ut energien i strømningen i waken ved diffusjon og miksing.

Tupphastighetsforholdet (TSR) var 6 under målingene uten grid generert turbulens, mens den var 7 under målingene med grid generert turbulens. Effekten av endringen i TSR ble evaluert, og det ble funnet at det ikke var nødvendig å gjennomføre nye målinger. Normalspenningen basert på de målte hastighetene ble fasemidlet i forhold til posisjonen av turbinbladene ved bruk av Matlab. Når disse verdiene ble sammenlignet med normalspenningen beregnet direkte fra tidsseriene, ble det funnet at tuppvirvlene hadde slått seg sammen eller blitt brutt opp ved alle målepunkt unntatt ved $X/D = 1$ nedstrøms turbinen uten grid generert turbulens. Det ble gjennomført en effektspektrumtetthetsfunksjon (PSD) som bekreftet observasjonene.

Tuppvirvlene var ikke likt fordelt i waken, og oppstod ved 30° , 128° og 224° ved henholdsvis $z/R = 1,12$, $1,15$ og $1,20$. Diameterne var $1,8E-2$ m, $1,4E-2$ m, $2,7E-2$ m i z retning. Plasseringen av den høyeste verdien til normalspenningen hadde en tendens til å vandre litt frem og tilbake, hovedsakelig i retning mot rotorsenter med en avstand fra $4,5E-3$ m til $1,8E-2$ m og i strømningsretningen med en total avstand på $6,2E-2$ m. Tuppvirvlene så ut til å vandre individuelt i waken og med ulik avstand.

Basert på resultatene og observasjonene gjort i denne studien burde nye målinger gjennomføres ved en kortere avstand til turbinrotoren for å kunne sammenligne vandringen av waken for de to innkommende strømningene.

Contents

1. Introduction	1
1.1. Earlier work	2
2. Aim of study	5
3. Theory	7
3.1. Wind turbine aerodynamics.....	7
3.2. General equations of fluid flow	9
3.2.1. Reynolds number.....	9
3.2.2. Strouhal number	10
3.2.3. Navier-Stokes equations.....	10
3.3. Atmospheric boundary layer	12
3.3.1. Viscosity and shear stress.....	13
3.3.2. Mean velocity profiles.....	14
3.3.3. Velocity-defect law	15
3.3.4. Nature of the wind.....	15
3.4. Turbulence	17
3.4.1. Turbulent kinetic energy	18
3.4.2. Integral length scale	20
3.4.3. Power spectral density function	21
3.4.4. Grid turbulence.....	23
3.5. Wind turbine wakes	24
3.5.1. Bluff body wakes and wake meandering	28
3.6. Hot-wire.....	29
4. The experiments	33
4.1. Setup and Equipment.....	33
4.1.1. Model wind turbine	33
4.1.2. Wind tunnel.....	35
4.1.3. Grid.....	36
4.1.4. Hot-wire anemometry	36

4.2.	Calculations	37
4.3.	Calibration	38
4.3.1.	Forces	38
4.3.2.	Free stream velocity	39
4.3.3.	Hot-wire	40
4.4.	Experiments	42
4.4.1.	The use of five hot-wire probes.....	42
4.4.2.	Modeling atmospheric conditions in the wind tunnel	43
4.4.3.	Grid turbulence measurements and integral length scale calculations.....	44
4.4.4.	Performance measurements of the model wind turbine	48
4.4.5.	Measurements in the wake of the model wind turbine.....	51
4.4.5.1.	Locating the tip vortices	51
4.4.5.2.	Measurements with hot-wire array	53
4.4.5.3.	Second experiment with hot-wire array.....	56
5.	Main results and discussion	59
5.1.	Time series $X/D = 1$	59
5.2.	Time series $X/D = 3$	66
5.3.	Time series $X/D = 5$	71
5.4.	Time averaged turbulent kinetic energy	74
5.5.	Phase averaging of the measurements	76
5.5.1.	Phase averaged fluctuating velocity, u'	76
5.5.2.	Phase averaged normal stress, $u'u'$	79
5.6.	Study on one tip vortex.....	83
5.6.1.	Without grid generated turbulence, $X/D = 1$	83
5.6.2.	With grid generated turbulence, $X/D = 1$	85
5.7.	Cross correlation of the flow field in the wake	88
5.8.	Power spectral density function, PSD	92
5.8.1.	$X/D = 1$	92
5.8.2.	$X/D = 3$	96
5.9.	Final discussion	97
6.	Conclusion	101

7. Further work	105
Bibliography	i
A. Appendix	iii
A.1 Calibration data	iii
A.1.1. Thrust gauge	iii
A.1.2. Torque gauge	iv
A.1.3. Pressure transducer Pitot probe	v
A.1.4. Pressure transducer contraction	vi
A.1.5. Hot-wire anemometry	vii
A.2. Comparison normal stress	viii
A.3. Uncertainty calculations	xi
A.4. Fully developed pipe flow measurements	xii
A.6. Risk assessment of laboratory setup and experiment	xv

List of figures

Figure 3.1: Wind speed spectrum, Van der Hoven (1957) Brookhaven, New York [10].....	16
Figure 3.2: Normal stresses for the different components in turbulent kinetic energy, (modified) [16]	19
Figure 3.3: General grid	23
Figure 3.4: Flow visualization experiment at TUDelft, showing two revolutions of tip vortices for a two-bladed rotor [2]	24
Figure 3.5: Velocity profile in the wake of a wind turbine	26
Figure 3.6: Flow visualization with smoke grenade in tip, revealing smoke trails for the NREL turbine in the NASA-Ames wind tunnel [2]	27
Figure 3.7: Hot-wire probe	29
Figure 3.8: Hot-wire control circuit, constant current.....	31
Figure 3.9: Hot-wire control circuit, constant temperature	31
Figure 4.1: Model wind turbine.....	33
Figure 4.2: Airfoil S826 [26].....	34
Figure 4.3: Sketch of wind tunnel [29]	35
Figure 4.4: Sketch of a section of the grid with dimensions	36
Figure 4.5: Calibration thrust gauge.....	38
Figure 4.6: Setup hot-wire measurements	40
Figure 4.7: Grid installed in wind tunnel	44
Figure 4.8: Integral length scale compared to von Karman specter	46
Figure 4.9: Integral length scale based on cross correlation between two hot-wire probes.....	47
Figure 4.10: Autocorrelation of hot-wire signal in the center of the wind tunnel.....	47
Figure 4.11: Power coefficient curve, with and without grid turbulence, TSR 1-12	49
Figure 4.12: Thrust coefficient curve, with and without grid turbulence, TSR 1-12.....	50
Figure 4.13: Denomination of the directions according to the model wind turbine	51
Figure 4.14: $X/D = 1$, turbulent kinetic energy with (red line) and without (blue line) grid turbulence, left side	52
Figure 4.15: $X/D = 1$, turbulent kinetic energy with (red line) and without (blue line) grid turbulence, right side	52
Figure 4.16: $X/D = 5$, turbulent kinetic energy with (red line) and without (blue line) grid turbulence, left side	52
Figure 4.17: $X/D = 5$, turbulent kinetic energy with (red line) and without (blue line) grid turbulence, right side	52
Figure 4.18: Rake 1, with distance between hot-wire probes	54
Figure 4.19: Rake 2, with distance between hot-wire probes	54
Figure 4.20: Results from first multiple hot-wire probes measurements	55
Figure 4.21: Picture of hot-wire rake 2 and Pitot probe setup	56
Figure 4.22: Velocity triangle	57
Figure 5.1: $X/D = 1$, Position 1 (a) Five rotations without grid turbulence, (b) Five rotations with grid turbulence	59

Figure 5.2: X/D = 1, Position 1, Contour plot (a) Five rotations without grid turbulence, (b) Five rotations with grid turbulence	60
Figure 5.3: Tip vortex shedding	61
Figure 5.4: X/D = 1, Position 2 (a) Five rotations without grid turbulence, (b) Five rotations with grid turbulence	62
Figure 5.5: X/D = 1, Contour plot, Position 2 (a) Five rotations without grid turbulence, (b) Five rotations with grid turbulence	62
Figure 5.6: X/D = 1, Position 3, (a) Five rotations without grid turbulence, (b) Five rotations with grid turbulence	64
Figure 5.7: X/D = 1, Contour plot, Position 3 (a) Five rotations without grid turbulence, (b) Five rotations with grid turbulence	64
Figure 5.8: X/D = 3, Position 1 (a) Five rotations without grid turbulence, (b) Five rotations with grid turbulence	66
Figure 5.9: X/D = 3, Contour plot, Position 1 (a) Five rotations without grid turbulence, (b) Five rotations with grid turbulence	66
Figure 5.10: X/D = 3, Position 2 (a) Five rotations without grid turbulence, (b) Five rotations with grid turbulence	68
Figure 5.11: X/D = 3, Contour plot, Position 2 (a) Five rotations without grid turbulence, (b) Five rotations with grid turbulence	68
Figure 5.12: X/D = 3, Position 3 (a) Five rotations without grid turbulence, (b) Five rotations with grid turbulence	69
Figure 5.13: X/D = 3, Contour plot, Position 3 (a) Five rotations without grid turbulence, (b) Five rotations with grid turbulence	70
Figure 5.14: X/D = 5, Position 1 (a) Five rotations without grid turbulence, (b) Five rotations with grid turbulence	71
Figure 5.15: X/D = 5, Contour plot, Position 1 (a) Five rotations without grid turbulence, (b) Five rotations with grid turbulence	71
Figure 5.16: X/D = 5, Position 2 (a) Five rotations without grid turbulence, (b) Five rotations with grid turbulence	72
Figure 5.17: X/D = 5, Contour plot, Position 2 (a) Five rotations without grid turbulence, (b) Five rotations with grid turbulence	73
Figure 5.18: X/D=1, turbulent kinetic energy with (red line) and without (blue line) grid turbulence	74
Figure 5.19: X/D=3, turbulent kinetic energy with (red line) and without (blue line) grid turbulence	74
Figure 5.20: X/D=5, turbulent kinetic energy with (red line) and without (blue line) grid turbulence	74
Figure 5.21: X/D = 1, Phase averaged fluctuating velocity without grid turbulence.....	77
Figure 5.22: X/D = 1, Phase averaged fluctuating velocity with grid turbulence.....	77
Figure 5.23: X/D = 3, Phase averaged fluctuating velocity without grid turbulence.....	77
Figure 5.24: X/D = 3, Phase averaged fluctuating velocity with grid turbulence.....	77
Figure 5.25: X/D = 5, Phase averaged fluctuating velocity without grid turbulence.....	77
Figure 5.26: X/D = 5, Phase averaged fluctuating velocity with grid turbulence.....	77
Figure 5.27: X/D = 1, Phase averaged normal stress without grid turbulence.....	80

Figure 5.28: X/D = 1, Phase averaged normal stress with grid turbulence.....	80
Figure 5.29: X/D = 3, Phase averaged normal stress without grid turbulence.....	80
Figure 5.30: X/D = 3, Phase averaged normal stress with grid turbulence.....	80
Figure 5.31: X/D = 5, Phase averaged normal stress without grid turbulence.....	80
Figure 5.32: X/D = 5, Phase averaged normal stress with grid turbulence.....	80
Figure 5.33: Position 1, PDF on the location of one tip vortex, X/D = 1 without grid turbulence.....	83
Figure 5.34: Position 1, Time of which u' maximum was measured with hot-wire probe nr. 3 in each rotation, X/D = 1 without grid turbulence.....	83
Figure 5.35: Position 2, PDF on the location of one tip vortex, X/D = 1 without grid turbulence.....	85
Figure 5.36: Position 2, Time of which u' maximum was measured with hot-wire probe nr. 1 in each rotation, X/D = 1 without grid turbulence.....	85
Figure 5.37: Position 1, PDF on the location of one tip vortex, X/D = 1 with grid turbulence	86
Figure 5.38: Position 1, Time of which u' maximum was measured with hot-wire probe nr. 5 in each rotation, X/D = 1 with grid turbulence.....	86
Figure 5.39: Position 2, PDF on the location of one tip vortex, X/D = 1 with grid turbulence	87
Figure 5.40: Position 2, Time of which u' maximum was measured with hot-wire probe nr. 1 in each rotation, X/D = 1 with grid turbulence.....	87
Figure 5.41: Cross correlation X/D = 1 without grid with z/R = 1.2 as zero point.....	88
Figure 5.42: Cross correlation X/D = 1 with grid generated turbulence with z/R = 1.2 as zero point.....	89
Figure 5.43: Cross correlation of the tip vortex located within the first 100° of rotation.....	90
Figure 5.44: PSD of measurements conducted at z/R=1.050, X/D = 1 with (blue line) and without (red line) grid turbulence.....	93
Figure 5.45: PSD of measurements conducted at z/R=1.133, X/D = 1 with (blue line) and without (red line) grid turbulence.....	93
Figure 5.46: PSD of measurements conducted at z/R=1.201, X/D = 1 with (blue line) and without (red line) grid turbulence.....	93
Figure 5.47: PSD of measurements conducted at z/R=1.13, X/D = 3 with (blue line) and without (red line) grid turbulence.....	96
Figure 5.48: PSD of measurements conducted at z/R=1.21, X/D = 3 with (blue line) and without (red line) grid turbulence.....	96

Figure A.1: Calibration curve for thrust gauge	iii
Figure A.2: Calibration curve for torque gauge	iv
Figure A.3: Calibration curve for the pressure transducer Pitot probe	v
Figure A.4: Calibration curve for the pressure transducer for the contraction of the wind tunnel	vi
Figure A.5: Calibration curve for hot-wire probe	vii
Figure A.6: Normal stress at $X/D = 1$ without grid turbulence, phase averaged	ix
Figure A.7: Normalized normal stress at $X/D = 1$ without grid turbulence, time averaged	ix
Figure A.8: Normal stress at $X/D = 3$ without grid turbulence, phase averaged	ix
Figure A.9: Normalized normal stress at $X/D = 3$ without grid turbulence, time averaged	ix
Figure A.10: Normal stress at $X/D = 5$ without grid turbulence, phase averaged	ix
Figure A.11: Normalized normal stress at $X/D = 5$ without grid turbulence, time averaged	ix
Figure A.12: Normal stress at $X/D = 1$ with grid turbulence, phase averaged	x
Figure A.13: Normalized normal stress at $X/D = 1$ with grid turbulence, time averaged	x
Figure A.14: Normal stress at $X/D = 3$ with grid turbulence, phase averaged	x
Figure A.15: Normalized normal stress at $X/D = 3$ with grid turbulence, time averaged	x
Figure A.16: Normal stress at $X/D = 5$ with grid turbulence, phase averaged	x
Figure A.17: Normalized normal stress at $X/D = 5$ with grid turbulence, time averaged	x
Figure A.18: Normalized velocity profile	xiii
Figure A.19: u^+ versus normalized y coordinate	xiii
Figure A.20: Normalized normal stress as a function of y/R	xiii
Figure A.21: Turbulence intensity based on the friction velocity as a function of y/R	xiii

List of tables

Table 4.1: Suzlon wind turbine VS model wind turbine	43
Table 4.2: Mean values during grid measurements.....	44
Table 4.3: Results from grid turbulence measurements	45
Table 4.4: Mean values during measurements of the performance of the model turbine	48
Table 4.5: Mean values during measurements locating the tip vortices	51
Table 4.6: Mean values during measurements with hot-wire array	54
Table 4.7: Position of hot-wire probes	55
Table 4.8: Mean values during second measurements with hot-wire array	58
Table 5.1: $X/D = 1$, Position 1 of hot-wire probes	59
Table 5.2: $X/D = 1$, Position 2 of hot-wire probes	62
Table 5.3: $X/D = 1$, Position 3 of hot-wire probes	63
Table 5.4: $X/D = 3$, Position 1 of hot-wire probes	66
Table 5.5: $X/D = 3$, Position 2 of hot-wire probes	67
Table 5.6: $X/D = 3$, Position 3 of hot-wire probes	69
Table 5.7: $X/D = 5$, Position 1 of hot-wire probes	71
Table 5.8: $X/D = 5$, Position 2 of hot-wire probes	72
Table 5.9: $X/D = 1$, Position 1 of hot-wire probes	83
Table 5.10: $X/D = 1$, Position 2 of hot-wire probes	84
Table A.1: Calibration data for thrust gauge	iii
Table A.2: Calibration data for torque gauge	iv
Table A.3: Calibration data for pressure transduces Pitot probe.....	v
Table A.4: Calibration data for the pressure transducer for contraction in the wind tunnel	vi
Table A.5: Properties for the measurement in the fully developed pip flow	xii

Nomenclature

A	Area
A	Constant dependent on grid geometry
B	Number of turbine blades
C_P	Power coefficient
C_T	Thrust coefficient
C_{Dv}	Induced drag coefficient
C_d	Drag coefficient, infinite span
C_l	Lift coefficient, infinite span
D	Diameter of model wind turbine
D	Drag force
E_{uu}	Spectral energy density
I	Turbulence intensity
I	Current
L_x	Integral length scale
L_{uux}	Integral length scale x direction
L_{uuz}	Integral length scale z direction
M	Distance between the centerlines of one opening in the grid
Nu	Nusselt number
P	Total wind turbine power
T	Thrust force
T	Temperature
Q	Torque
Re	Reynolds number
Re_{crit}	Critical Reynolds number for transition
R	Radius wind turbine blade
R	Ideal gas constant
R	Resistance
$R_{uu}(\tau)$	Normalized auto-correction function
R_{uu}	Cross correlation
R_w	Resistance in hot-wire at operating temperature
St	Strouhal number
T	Time
T_u	Time scale
T_w	Operating temperature hot-wire
U, V, W	Mean velocity in direction (u, v, w)
U_∞	Free stream velocity
U_{ref}	Reference free stream velocity
U_{rel}	Flow velocity relative to the blade section
V	Voltage
f	Coriolis parameter
f	Frequency
$f_{b,i}$	Body forces due to the Coriolis effect and gravitation
w	Mean angular velocity
c	Chord length of airfoil

d	Drag per unit span
h	Height of boundary layer
h	Heat transfer coefficient
k	Turbulent kinetic energy
K	Thermal conductivity
l	Lift per unit span
l	Characteristic length
p	Pressure
r	Radial position on wind turbine blade
u^*	Friction velocity
u', v', w'	Fluctuating velocity in direction (u, v, w)
$u'u'$	Normal stress
u_i	Instantaneous velocity component in the i^{th} direction
x_i	Spatial coordinates (x, y, z)
z	Height above ground
z	Z direction (horizontal relative to wind tunnel floor)
z_0	Surface roughness

Greek symbols

α	Angle of attack
θ_p	Pitch angle
δ	Boundary layer thickness
ω	Rotational speed of wind turbine
ρ	Density
μ	Dynamic viscosity
ν	Kinematic viscosity
σ	Solidity
σ_u	Standard derivation of the fluctuations
Γ	Vortex strength
λ	Tip speed ratio
λ	Latitude
τ	Viscous shear stress
τ	Time lag
κ	von Karman constant
$\Phi_{uu}(f)$	Normalized power spectrum

1. Introduction

One of the greatest challenges in the 21st century is climate change, and its most severe impacts may be avoided if the current energy systems were transformed. In the last decades there has been an increasing investment and interest in renewable energy production due to the climate change. Renewable energy production is known to reduce greenhouse gas emissions and thereby reduce the impacts on global warming.

In 2008 it was estimated that approximately 19 % of the global electricity supply was contributed by the use of renewable energy. In 2010 renewable energy accounted for approximately half of the estimated 194 GW of the new electricity capacity added globally, which was up almost 8 % since 2009. In 2010, renewable energy delivered close to 20 % of global electricity supply and global wind power capacity increased the most by 39 GW. This is over three times the 11.5 GW of wind energy added worldwide five years earlier. The total existing wind power capacity in the end of 2010 was estimated to 2.0-2.5 % of the global electricity consumption. [1]

Wind energy is a growing renewable energy source worldwide. In 2010 at least 52 countries increased their total existing capacity and 83 countries now use wind power on commercial basis. The European Union installed nearly 9.5 GW in 2010, and countries such as Denmark and Portugal met their electricity demand with respectively 22 % and 21 % with wind power. [1]

Even though wind power increase as a renewable energy resource, and have several environmental benefits compared to the conventional electricity production in a global perspective, it has its negative externalities. Wind energy production will create noise and the turbines may interfere with living organism populations, and some will find wind turbines as a visual pollution. Another challenge in wind energy production is the variations in the wind and the influence the wind turbines have on each other when placed in a wind farm. The variations in the wind can make the energy production unstable if the turbine is not controlled according to the conditions, and the wake from a turbine can cause fatigue loads on a turbine further downstream in a wind farm. Another unfortunate consequence of using wind turbines in wind farm is that the wind turbines within the farm will produce less power due to the disturbed flow caused by the upstream turbines. It is therefore crucial to know how the wake of a turbine behaves and develops downstream, and to be able to predict the flow conditions by conducting simulations.

1.1. Earlier work

When airflow passes through a rotating wind turbine rotor, the kinetic energy in the wind is extracted and converted to mechanical energy. This results in a field with reduced wind velocity and an interrupted airflow behind the rotor, which is termed the wake of the wind turbine.

The research on wind turbine wakes has been ongoing since the late 1970s [2], and in the last decade it has increased even more as the turbines are installed in wind farms. The wake of a turbine is known to affect the downstream turbine and cause fatigue loads. Two primary characteristics of the wake are of special interest when considering the downstream wind turbine; the turbulence intensity and the velocity deficit.

The airflow in the wake of a horizontal-axis wind turbine is a complex turbulent flow, but several studies have shown characteristics in the flow. There are rotational motion induced by the turbine blades, longitudinal and radial pressure gradients and vortices shed by the tip and root of the blade, generating spiral vortices. There have also been observed unsteady behavior of the wake, where the whole wake oscillates randomly. This unsteady behavior is termed wake meandering.

Studies of the wake meandering phenomenon have resulted in two main possible explanations of its formulation. One deal with the intrinsic instabilities in the wake characterized by a periodic vortex shedding appearing in the wake, and the other is based on how large scale turbulent eddies in the atmospheric boundary layer affect the wake. Medici and Alfredsson conducted a study in 2006 on the meandering phenomenon in a wind tunnel with a rotating wind turbine model [3]. Their study showed a periodic spectral signature of the vortex shedding, which can be compared to those who appear in bluff body wakes. In another study, also conducted by Medici and Alfredsson in 2007, it was found that the meandering of the wake is related to the tip speed ratio and thrust coefficient of the turbine [4]. It was also proven that an increasing thrust coefficient is needed when increasing the tip speed ratio to obtain a meandering motion of the wake.

Due to the fact that the wake meandering is, among other, believed to be caused by large scale turbulent eddies found in the atmospheric boundary layer (ABL), several studies have been conducted by the use of the actuator disk concept. Scaling down a wind turbine to a static porous disk, and physical modeling an atmospheric boundary layer in a wind tunnel, has been the experimental setup in many studies. In 2011, G. España, S. Aubrun, S. Layer and P. Devinant conducted a study based on this concept [5]. Their aim was to prove the role of the large atmospheric turbulent scales on the meandering phenomenon. They conducted measurements in both a quite rough ABL, with turbulent integral length scales of about 10 times the disk diameter, and in HIT (homogeneous and isotropic turbulent) conditions where the integral length scales were 3-10 times smaller than the disk diameter. In the rough ABL, random oscillations of the wake were observed, while in the HIT conditions, no meandering was observed.

However, in studies conducted using this kind of experimental setup, the influence by the tip vortices in the wake of the turbine and the rotational motion of the wake are omitted.

In 2012, S. Aubrun, T. F. Tchouaké, G. España, G. Larsen, J. Mann and F. Bingöl conducted a study where they compared wind tunnel experiments and field experiments on wind turbine wake meandering [6]. They found that the wind tunnel data representing the standard derivation of the instantaneous wake center locations and wake widths, showed systematically more variability than the corresponding for the field experiments, although the turbulence intensity and the turbulence length scales were approximately similar. From this they concluded that the content of the turbulent eddies responsible for the meandering is more pronounced in the wind tunnel. In their final conclusion they stated that the turbulence spectra must be carefully compared to ensure that field and wind tunnel data are obtained under similar conditions.

Studies have shown that the wake deficits measured in the field are often smaller than those from wind tunnel experiments when comparing wind tunnel wake measurements with available field data. It is believed that the difference is caused by the variability of the wind, particular wind direction, which gives rise to wake meandering. This means that a measured deficit averaged over a few minutes will in fact be averaged over a portion of the wake profile. [7]

At the Institute of Fluid Mechanics at NTNU, there have been conducted various studies on the flow around airfoils and on wind turbine models for many years. Currently, there are several experimental studies carried out on small scale wind turbine models in the wind tunnel at the institute.

One of the wind turbine models, the one used in this study, has turbine blades designed at NTNU using the BEM (Blade Element Momentum) method. The design point for the turbine blades is a tip speed ratio of 5 and an angle of attack of 7.0° , with corresponding lift and drag coefficients of 1.2756 and 1.35E-2 respectively. The rotor has a diameter of 0.9 m, and the blades are machined from aluminum.

2. Aim of study

The need for good predications of the wind turbine wake is required when developing a wind farm. The effect of the wake from an upstream turbine within a wind farm can be a fundamental factor when considering life expectancy and maintenance cost of the turbines. However, to model the wake accurately has proven to be difficult.

Wind tunnel model test are very useful in order to verify computer predications. Though, a direct comparison with experimental data requires that the experimental data represent the quantities that one wishes to check. There exists many good measurements on the wake of a turbine, but they may not represent the same quantities as produced by the predications. The tendency of the wake to move around in space, often termed wake meandering, may be a source of error to the difficulty of modeling the wake accurately.

In this master thesis the wake meandering phenomenon will be studied on a model wind turbine using a hot-wire array. There have been conducted many experiments on the wake meandering phenomenon, but most of them are based on single point measurements. When measuring turbulence in a fixed point in space, the meandering of the wake will lead to a smearing out of the steep gradients found in the wake. This will result in a measured turbulence level that appears lower than what is really the case.

The experiments in this master thesis will be conducted in the wind tunnel at the Department of *Energy and Process Engineering* at NTNU. After initial measurements at multiple nearby points in the wake of the model wind turbine in a low turbulence incoming flow, the same measurements will be conducted when the turbine is placed in a flow with free stream turbulence intensity typical for atmospheric turbulence. Further, the wake meandering will be studied for the two cases based on the position of the tip vortices. This will be performed to be able to see how the wake development changes with free stream turbulence, and to see how this affects the smoothing of the data.

It is crucial to use a correct measurement technique in order to establish trustworthy results when conducting an experiment in a wind tunnel. Thus, as an introduction to the measurement techniques when utilizing hot-wire anemometry, an experiment will be conducted on a fully developed pipe flow at an early stage of the thesis. Further, these techniques will be used when conducting simultaneous measurements at multiple nearby points in the wake of the model wind turbine, in both a low turbulence incoming flow and in a flow that has free stream turbulence intensity typical for atmospheric turbulence. The atmospheric turbulence will be generated by installing a grid in the wind tunnel.

To be able to comprehend grid generated turbulence, how the flow field in the wake behaves and how it is affected by turbulence, a study concerning wind turbine aerodynamics, fluid flows, turbulence and wakes will be conducted in an early stage in the thesis. This will be presented as an opening in the report, before the technique, experimental setup and results are presented. The results of the main measurements and the appurtenant discussion will be combined in one chapter. This will give a better overview when discussing and comparing the results. At the end of the report, a conclusion will be conducted based on the analysis, with some remarks on further work.

Since model wind turbine in question in this thesis is a three bladed horizontal axis turbine, the literature regarding wind turbine aerodynamics and wake structure is based on these kinds of turbines.

During the measurements in the wind tunnel it is assumed that the incoming flow is uniform distributed, and that the boundary layer created from the floor and sidewalls in the tunnel don't affect the flow passing the model wind turbine rotor. The uncertainty regarding the use of hot-wire anemometry in the experiments will not be discussed or valuated in the thesis due to the difficulty of stating an accurate uncertainty. Though, it is crucial to keep in mind that there are numerous sources of error and uncertainties in experiments which can affect the results.

3. Theory

There are many features that affect wind turbine performance and the predications of its behavior. In this chapter there are given an introduction to the general theory concerning the aerodynamics of a wind turbine and governing equations for fluid flows. Further, turbulence both in the atmosphere and grid generated are accounted for, before the complex behavior in the wake of a wind turbine is studied. A study on hot-wire anemometry will also be conducted.

3.1. Wind turbine aerodynamics

The most common design of wind turbines today is the horizontal axis wind turbine (HAWT), where the axis of rotation is parallel to the ground. These kinds of turbines are often placed in a wind farm to increase the energy production from a specific site. This will of course increase the investment and the turbines downstream in the farm will have poorer wind conditions due to the altered air flow caused by the upstream wind turbines.

A wind turbine is a device that converts the kinetic energy in the wind to mechanical energy. The amount of available kinetic energy in the wind per unit time for a given area A , normal to the wind direction, is given by;

$$P = \frac{1}{2} \rho A U_{\infty}^3 \quad (3.1)$$

where ρ is the air density and U_{∞} is the free stream wind velocity. This can be shown from the continuity equation of fluid mechanics. However, it is not possible for the wind turbine to utilize all the energy in the wind. In 1919 Albert Betz proved that the maximum power that can be extracted from the wind is 59.3 % (16/27) of the kinetic energy in the wind. This is due to that the air has to move past the turbine rotor and thus cannot stand still behind the turbine. The limit is referred to as Betz limit and is only theoretical. For a modern horizontal axis wind turbine, a maximum of about 45 % of the available wind energy is extracted.

To determine the efficiency of a wind turbine, the ratio between the power extracted and the available power is calculated. This ratio is normally denoted the power coefficient, C_P , and is given by;

$$C_p = \frac{P_{extracted}}{P_{available}} = \frac{Q\omega}{\frac{1}{2}\rho AU_\infty^3} \quad (3.2)$$

where Q is the torque of the turbine, which is an estimate of the force in the rotational direction, ω is the rotational speed of the turbine rotor and A is the rotor area.

The wind also generates a thrust force, T , on the wind turbine. This is the load the turbine needs to withstand in the axial direction. The thrust coefficient, C_T , is normally expressed by;

$$C_T = \frac{T}{\frac{1}{2}\rho U_\infty^2 A} \quad (3.3)$$

From the power equation it can be seen that the wind speed is a determining factor for the amount of energy in the wind. The wind speed will also influence the tip speed ratio (TSR) to the turbine. Tip speed ratio is given the symbol λ , and is governed by the equation;

$$\lambda = \frac{\omega R}{U_\infty} \quad (3.4)$$

where ω is the rotational speed of the rotor, R is the radius of the rotor and U_∞ is the free stream wind velocity. Tip speed ratio is an important design parameter for the turbine. Generally a wind turbine is not optimized for a certain wind speed, but an ideal tip speed ratio. This is done with the idea that if the wind speed changes from what the turbine is designed for, one can change the rotational speed and still obtain an optimum C_p and the designed tip speed ratio.

In the study conducted by Medici and Alfredsson in 2006 it was found that both the thrust of the turbine and the tip speed ratio influence the wake meandering behind a wind turbine [4]. They found, among other factors, that the thrust force needed to be increased when increasing the tip speed ratio in order to obtain a meandering motion of the wake. The phenomenon *wake meandering* will be clarified in Section 3.5.

The aim with the shape of an airfoil, creating the turbine blade, is to have a high lift-to-drag ratio. By obtaining a high lift-to-drag ratio throughout the wingspan of a turbine blade, the power extraction can be optimized. Lift is generated by the difference in dynamic pressure that arises when the airflow passes the airfoil. The flow velocity over the airfoil increases over the convex surface. This result in a lower average pressure on the suction side of the airfoil compared with the concave side of the airfoil. The lift force is defined perpendicular to the direction of the relative wind. Lift per unit span, l , of the airfoil is normally expressed by;

$$l = \frac{1}{2}\rho U_\infty^2 c C_l \quad (3.5)$$

where c is the airfoil chord length, and C_l is the sectional lift coefficient.

An airfoil is subjected to two different kinds of drag forces that opposes the direction of the flow when moving through a fluid; form drag caused by pressure, and skin friction drag caused by shear stress. When an airfoil is immersed in a free stream flow, there will be a pressure difference between the front and back of the object. This will push, or drag, the object in the flow direction. The form drag is dependent on the shape of the body, hence the name form drag. Skin friction drag is dependent on the roughness of the object. If an object has a smooth surface the shear forces, and hence the skin friction drag, will be lower than an object with a rough surface. For an airfoil the pressure drag will vary with the flow direction relative to the airfoil.

Skin friction drag along the surface of an airfoil is often the main drag component for normal operating conditions of a wind turbine. This is created between the fluid and the surface of the body. Drag per unit span, d , on an airfoil is normally expressed by;

$$d = \frac{1}{2} \rho U_{\infty}^2 c C_d \quad (3.6)$$

where U_{∞} is the free stream velocity, c is the chord length of the airfoil and C_d is the sectional drag coefficient. The drag force is defined to be parallel to the direction of the relative wind, and related to the thrust force acting on the wind turbine.

The angle between the relative wind and the chord line of an airfoil is termed the angle of attack. The angle of attack is an important parameter in performance calculations.

[8]

3.2. General equations of fluid flow

In this section governing equations concerning fluid flow will be presented. These equations and flow properties are fundamental in the predications on the flow concerning wind turbine wakes.

3.2.1. Reynolds number

Reynolds number can be used to determine if a flow is laminar, in transition or turbulent. It is a dimensionless parameter and is a measure of the ratio of inertia forces to viscous forces. A low Reynolds number corresponds to a laminar flow and a high Reynolds number to a turbulent flow. A number in-between, Re_{crit} , indicate that the flow is in a transition from laminar to turbulent flow. The Reynolds number is normally defined by a characteristic length, l , and relative velocity, U_{rel} , to the kinematic viscosity, ν , of the fluid;

$$Re = \frac{U_{rel} l}{\nu} \quad (3.7)$$

3.2.2. Strouhal number

When a solid body is immersed in a free stream flow, it might arise a periodic vortex shedding with an oscillatory pattern in its wake. This pattern can be described by the dimensionless Strouhal number, St . The Strouhal number is given by;

$$St = \frac{fl}{U_\infty} \quad (3.8)$$

where the f is the frequency of the vortex shedding, l is the characteristic length and U_∞ is the free stream velocity.

3.2.3. Navier-Stokes equations

The set of Navier-Stokes equations is the most basic set of equations used to describe the motion of fluid substances. The solution of the set is normally termed a velocity field or flow field and describes the velocity of a fluid at a given point in time and space. The equations arise from applying the assumption that the fluid stress is the sum of a diffusing viscous term and a pressure term together with Newton's second law to fluid motion. For a Newtonian fluid, with constant density and viscosity, the motion can be described by;

$$\frac{\partial u_i}{\partial t} + u_j \frac{\partial u_i}{\partial x_j} = -\frac{1}{\rho} \frac{\partial p}{\partial x_i} + \nu \frac{\partial^2 u_i}{\partial x_j^2} + f_{b,i} \quad (3.9)$$

$$\frac{\partial u_i}{\partial x_i} = 0 \quad (3.10)$$

where u_i is the instantaneous velocity component in the i^{th} direction and t is time. p is the pressure and $f_{b,i}$ are body forces due to the Coriolis effect and gravitation. x_i corresponds to the spatial coordinates (x, y, z) and are independent variables. ν is the kinematic viscosity given by $\nu = \mu/\rho$. The first Equation (3.9) concerns the conservation of momentum, while the second Equation (3.10) is the continuity equation. This set of equations gives four equations with four unknowns if density, ρ , and dynamic viscosity, μ , are known.

In a turbulent flow the detailed velocity and pressure field is not reproducible due to the rapid fluctuations in time and space. Hence, the instantaneous values are split into two components; a mean value and a fluctuating part;

$$u = U + u' \quad v = V + v' \quad w = W + w' \quad p = P + p' \quad (3.11)$$

where the mean value, here represented only in U direction, is defined by;

$$U = \frac{1}{T} \int_{t=t_0}^{t=t_0+T} u dt \quad (3.12)$$

The mean of the fluctuating part is zero, while the standard derivation of the fluctuations gives the so called *root mean square* (rms) value;

$$\sigma_u = \sqrt{\overline{u'^2}} = \sqrt{\frac{1}{T} \int_{t=t_0}^{t=t_0+T} u'^2 dt} \quad (3.13)$$

When substituting the instantaneous components in Equation (3.11) with the sum of the mean value and the fluctuating part and taking the time average (as in Equation (3.12)) one obtain the so called Reynolds average Navier-Stokes (RANS) equations;

$$\frac{\partial U_i}{\partial t} + U_j \frac{\partial U_i}{\partial x_j} = -\frac{1}{\rho} \frac{\partial P}{\partial x_i} + \nu \frac{\partial^2 U_i}{\partial x_j^2} + F_{b,i} - \frac{\partial(\overline{u'_i u'_j})}{\partial x_j} \quad (3.14)$$

$$\frac{\partial U_i}{\partial x_i} = 0 \quad (3.15)$$

Equation (3.14) is quite similar to the original Navier-Stokes equation for conservation of momentum, except for the last term which represents the influence of the turbulent stresses on the mean motion. The term can also be written as $\frac{1}{\rho} \frac{\tau_{ij}}{\partial x_j}$, giving $\tau_{ij} = -\rho \overline{u'_i u'_j}$ which is termed the Reynolds stress. This introduces six new unknowns to the original four in the Navier-Stokes equation set. When solving this set of equations in simulations it is normally used transport equations for the Reynolds stresses. In this study $u'u'$ will be used and referred to as the normal stress of the flow.

Solving the Navier-Stokes equations accurately is difficult. Turbulent flows are highly unsteady, and a plot of the velocity as a function of time at most points in the flow would appear random to an observer unfamiliar with these flows. There are three dimensional motions where the instantaneous field fluctuates rapidly in all three spatial dimensions. Solving this set of equations is thus time-consuming, expensive and requires huge amount of data capacity. This makes experiments crucial in the growth and progress of wind energy.

[9]

In Section 3.4 the structure and properties in turbulent flows will be clarified.

3.3. Atmospheric boundary layer

In this section it is given a general overview of how the atmospheric boundary layer is built up. This is studied to know how the flow field surrounding a full scale wind turbine affects both the performance and wake development of the turbine. To get a better understanding of boundary layer flow, properties such as shear stress and friction velocity will also be studied. This section is intended as a fundament and introduction turbulent flows and thus, the wake behind a wind turbine.

The planetary, or the atmospheric boundary layer (ABL), is known as where the flow is affected by surface friction. It is normally divided into different regions in which the layer is influenced by various parameters; molecular layer, surface layer and Ekman layer. The molecular layer includes the lowest millimeters of the ABL, where the structure of scalars, such as temperature, is strongly influenced by molecular properties. However, the momentum is not influenced, unless the surface is unusually smooth, which can appear over waters in weak winds.

Above the first millimeters of the ABL, the flow is affected by a vertical temperature gradient and surface friction. The effects of the earth's rotations, the Coriolis force, and the vertical variation of stress can be neglected and the wind direction is nearly constant. This layer is normally termed the surface layer. The region is approximately 30 m high, but varies a great deal depending on the stratification. For instance, at night the fluxes can be weak and the stratification quite strong, leading to a narrow surface layer.

At higher altitudes, the flow is affected by the Coriolis force, temperature gradients and friction. In these conditions the wind direction change significantly with height, and it forms the outer region of the ABL normally termed the Ekman layer. The height of the Ekman layer is dependent on many factors, and the boundary between the free atmosphere and the ABL has been observed to be at 20 m up to 5 km above the earth's surface. Parameters that influence the height of the layer are, among other, orography, surface roughness, wind speed, temperature and the rate of heating and cooling of the surface.

In unstable or neutral air the turning of the wind can be neglected in a region of the Ekman layer. It is therefore often convenient to subdivide the Ekman layer into two regions; below 150 m the earth's rotation is important, but the turning of the wind can be neglected. This is only useful in the absence of hydrostatically stable air, where the turning of the wind may start at much lower altitudes. The region below 150 m is often termed the tower layer, and it is found that many of the relationships developed for the surface layer is applicable in this part of the Ekman layer.

When adiabatic cooling of the air as it rises is such that it remains in thermal equilibrium with its surroundings, the conditions in the atmosphere is termed neutral. This is often the case in strong winds, and the effects of the surface roughness and the Coriolis force have a sufficient effect on the boundary layer properties at these conditions.

The surface roughness is characterized by a roughness length z_0 and is in the order from 1.0E-3 for flat desert and rough sea, to 0.7 for cities and forests [10]. The Coriolis force is defined by a Coriolis parameter f ;

$$f = 2\Omega \sin(|\lambda|) \quad (3.16)$$

where f is the rotation of the earth represented as an angular velocity Ω and λ is the latitude. Further, the height of the boundary layer (at temperate latitudes) is given by;

$$h = \frac{u_*}{6f} \quad (3.17)$$

Here, u_* is the friction velocity defined by;

$$\frac{u_*}{U_{mean}(z)} = \frac{\kappa}{\ln\left(\frac{z}{z_0}\right) + \Psi} \quad (3.18)$$

where κ is the von Karman constant, and Ψ is a function dependent on the stability. The function is positive for stable conditions, giving high wind shear, and negative for unstable conditions, giving rise to low wind shear. z_0 is the surface roughness length and z is height above the ground.

[10-12]

The friction velocity can also be expressed by shear stress, which will be presented in the next section.

3.3.1. Viscosity and shear stress

When fluid passes over a solid surface, the viscosity of the fluid will influence the flow. Viscosity may be thought of as a measure of fluid friction and describes the fluids internal resistance to flow. The viscosity will slow down the fluid such that the velocity of the fluid relative to the surface of the solid will be zero, which is termed the no-slip condition. This region of the fluid then transfers momentum to adjacent layers through the action of viscosity and creates a thin layer of fluid with slightly higher velocity than the inner flow. The velocity of the fluid will gradually increase with increasing distance to the surface, up to the value that corresponds to the external “frictionless” flow. The transfer of momentum creates a velocity gradient normal to the solid surface. The region between zero velocity and the external frictionless flow is termed the boundary layer. The boundary layer can be either laminar, in transition or turbulent.

When fluid moves along any solid boundary it will incur a shear stress on that boundary. Shear stress is proportional to the velocity gradient normal to the wall, and is given by the elementary law of fluid friction;

$$\mathcal{T}(y) = \mu \frac{\partial U}{\partial y} \quad (3.19)$$

where μ is the dynamic viscosity of the fluid.

As long as the fluid viscosity and the velocity gradient at the solid surface are known, the friction caused by the shear stress can be calculated;

$$\mathcal{T}_w = \mu \left. \frac{\partial U}{\partial y} \right|_{wall} \quad (3.20)$$

Integrated along the wall, one can find the shear stress causing a viscous friction force on the wall when exposed to a fluid flow. The friction velocity can then be expressed by;

$$u_* = \sqrt{\frac{\tau_w}{\rho}} \quad (3.21)$$

where ρ is the fluid density. The friction velocity is thus a characteristic velocity and not a flow velocity.

[13]

3.3.2. Mean velocity profiles

In the atmospheric boundary layer, the vertical wind profile for the mean streamwise velocities can be expressed by the power law;

$$\frac{U(z)}{U(z_{ref})} = \left(\frac{z}{z_{ref}} \right)^\alpha \quad (3.22)$$

This law is often used in micrometeorology, where z_{ref} is a chosen reference height. However, $z_{ref}=10$ m is often used due to uncertainties related to the gradient height in the atmospheric boundary layer. The exponent, α , is a factor that mainly depends on the roughness for aerodynamically rough surfaces. For aerodynamically smooth surfaces it depends on the Reynolds number. The power law is seen to give a good description of the velocity profile for a wide range of velocities, while the flow near the ground is not well represented.

The logarithmic law is another law describing the vertical mean velocity profile in the streamwise direction, and can be written in two ways;

$$\frac{U}{u_*} = \frac{1}{\kappa} \ln \left(\frac{Z_z u_*}{\nu} \right) + C_0 - \frac{\Delta U}{u_*} \quad (3.23)$$

$$\frac{U}{u_*} = \frac{1}{\kappa} \ln \left(\frac{Z_z}{Z_0} \right) \quad (3.24)$$

This law applies to a turbulent boundary layer and it is a physical basis for the use of this law, unlike for the power law. κ is the von Karman's constant, normally equal 0.41, u_* is the friction velocity, z_0 is the roughness length and C_0 is a constant, generally $C_0 \approx 5.2$.

The law can be derived in different ways, but it is generally derived by asymptotical fitting. This requires that the velocity profile in the outer layer match the velocity profile in the sub layer in the overlap region. The law is universal for smooth surfaces and is shifted downwards with increasing surface roughness.

[14, 15]

3.3.3. Velocity-defect law

The flow in the outer layer, mentioned in the previous section, is independent of viscosity. Thus, the deviation between the free stream velocity and the mean velocity in the outer layer is given by the velocity-defect law;

$$\frac{U_e - U}{u_*} = G(\eta) \quad (3.25)$$

Here η represents Z_z/δ . Z_z is a parameter used for very rough surfaces as the height above a new zero level, and defined by $z-d_0$, where z is the height above ground and d_0 is a displacement height. u_* is the friction velocity.

[14]

3.3.4. Nature of the wind

The energy available in the wind varies with the cube of the wind speed. Wind is highly variable, both in space and time, dependent on how one consider the wind. The wind variation can be considered on many time- and space scales, ranging from a large-scale global circulation pattern to turbulence at one specific point.

The origin of the wind is the differential surface heating of the earth caused by sun energy. Warm air rises to the atmosphere, circulates and cools down, before it sinks back to cooler places. The Coriolis force affects the large-scale motion of the air and the result is a global circulation pattern of the air. The non-uniformity of the earth's surface interrupt the circulation pattern, leading to a chaotic airflow witch gives the daily unpredictable variations at particular locations. The wind speed in the ABL increases with height above the surface, thus local regions of increased wind speed is often found on top of mountains and hills. The different heating of land and sea also cause considerable local variations in the wind speed. Along the coastal line it is often seen a local circulation of air, from the land out to the sea and back again, caused by the warm sea and cooler land. The process is reversed, air moving from the sea and onshore, when the land is warmer that the sea. As the land heats up and cools down more rapidly than the sea, this pattern of land and sea breezes tends to reverse every 24 hours.

The variation in the wind can be represented on many time-scales; annual, seasonal, monthly and diurnal, to mention some. On an even shorter time-scale, typically less than 10 minutes, the variation, or fluctuation in the wind speed is termed turbulence.

Figure 3.1 show a wind-speed spectrum for long- and short-term records for Brookhaven in New York created in 1957 by Van der Hoven. It clearly states the frequency content corresponding to some of the time-scales mentioned above.

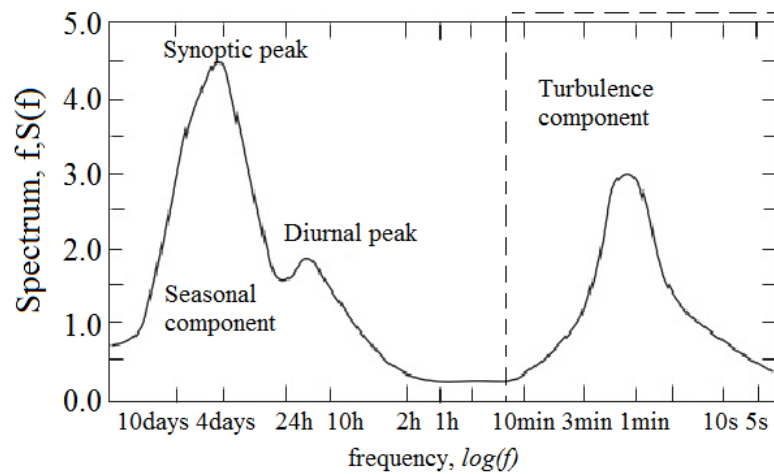


Figure 3.1: Wind speed spectrum, Van der Hoven (1957) Brookhaven, New York [10]

The wind can be thought of as consisting of a mean wind speed, depending on the time-scale (monthly, diurnal etc.), with turbulent fluctuations superimposed, as seen in Section 3.2.3.

[10]

3.4. Turbulence

As seen in the frequency spectrum in the previous section, turbulence has a relatively fast time-scale compared to the rest. There are mainly two effects that generate turbulence; friction and thermal effects. The friction against any surface causes the flow to alter its behavior, as explained in Section 3.3.1, leading to a chaotic and unpredictable flow. The thermal effects can cause the air to move both vertical and horizontal due to the change in density. The result is a complex flow, with motions in three dimensions, which cannot be represented in a simple manner. It is however possible to formulate a set of differential equations describing the process and integrate the expressions forward in time, starting from certain initial- and boundary conditions. Small changes or mistakes in the conditions can evolve to great differences between the predications and the real flow, thus it's more useful to describe the turbulence in terms of statistical properties. Turbulence intensity is a statistical property describing the overall level of turbulence in the flow;

$$I = \frac{\sigma}{U_{mean}} \quad (3.26)$$

where σ is the standard variation of the wind speed variations about the mean wind speed U_{mean} . The mean velocity of the wind is often taken as an average over 10 minutes to 1 hour.

Since the turbulent properties vary in three dimensions it is common to denote the parameters according to a reference system with components u (longitudinal), v (lateral) and w (vertical). The longitudinal component of the turbulent intensity then becomes I_u and the standard deviation σ_u . Turbulence intensity depends on the surface roughness and especially in a neutral atmosphere.

Most of the fluid flows in the nature and in engineering applications are turbulent. As a fluid flow passes an obstacle, e.g. a sphere, the flow tends to separate from the obstacle and form a "shadow" of turbulent flow behind it. In this shadow the flow is unpredictable and fluctuates in all three dimensions, i.e. the flow is turbulent. The fluctuations occur in a wide range of time- and length scales in physical space. Turbulence is in other words a multi-scale problem with highly nonlinear coupling between these scales. However, the flow is not totally chaotic when studying high-Reynolds number turbulent flows. When investigating a flow separation from e.g. a sphere, the flow rolls up in eddies downstream the separation. These eddies tends to either merge together to form a greater eddy and at the same time create a new and smaller eddy in their intersection, or to break up in smaller eddies. If the eddies preserves a certain spatial structure, i.e. eddies can be found further downstream with approximately the same shape, it is termed a coherent structure. Examples of coherent structures are the so called horseshoe vortices and vorticity tubes, often called worms or filaments. The analysis of these coherent structures is important due to their significance to the transport and mixing of the flow.

When the flow becomes unstable, the large flow structures in the turbulent flow break up in smaller and smaller eddies, until they are diffused into heat due to viscous effects. In this way the turbulent kinetic energy is handed down from large eddies to progressively smaller and smaller eddies. This effect is termed the energy cascade.

As mentioned, the instantaneous velocity field in a turbulent flow is unpredictable; however it is possible to distinguish distinct statistical features such as average velocity. This makes it possible to characterize scales of statistical correlations. The instantaneous velocity, $u(x,t)$, can be divided into a mean value, U , and a fluctuating value, u' as shown in Equation (3.11).

The root mean square (rms) values of the velocity components in a turbulent flow, see Equation (3.13), are of particular importance in turbulent flows, since it gives information regarding the fluctuating part of the flow. The rms values can be easily measured with a velocity probe sensitive to the turbulent fluctuations, e.g. a hot-wire anemometer.

[9, 10]

3.4.1. Turbulent kinetic energy

The kinetic energy per unit mass associated with turbulence is given the symbol k , and is defined as;

$$k = \frac{1}{2} (\overline{u'^2} + \overline{v'^2} + \overline{w'^2}) \quad (3.27)$$

The turbulence intensity, I , see Equation (3.26), is linked to the turbulent kinetic energy by;

$$I = \frac{\left(\frac{2}{3}k\right)^{1/2}}{U_{ref}} \quad (3.28)$$

where U_{ref} is a reference mean flow velocity. [9]

In Figure 3.2 previous measurements conducted in the wake of the model wind turbine in question in this master thesis is represented. The figure shows the measurements of the turbulent energy and normal stress distributions measured along a horizontal diagonal.

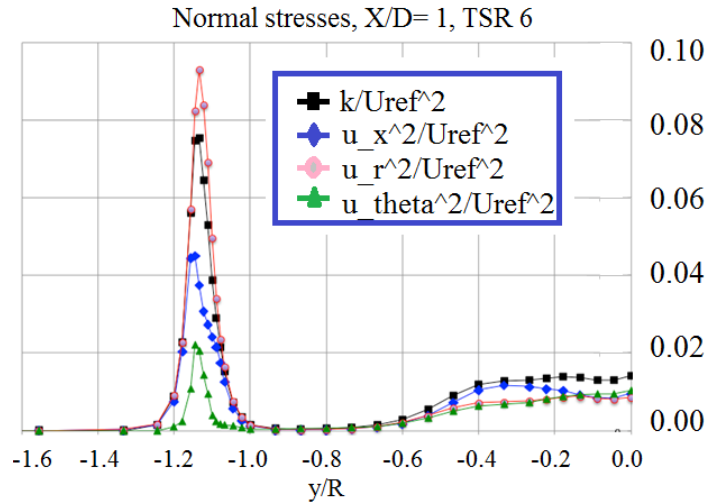


Figure 3.2: Normal stresses for the different components in turbulent kinetic energy, (modified) [16]

The green line represents the normalized normal stress (normalized by U_{ref}^2) in the circumferential direction, u_{theta}^2 , the blue line in the streamwise direction, u_x^2 , and the pink line represents the normalized normal stress in radial direction, u_r^2 . The black line represents the turbulent kinetic energy, k , normalized by the same U_{ref}^2 as the normal stresses. It is clear that the turbulent energy is some kind of mean, according to Equation (3.27), of the three components of the normal stresses. When comparing the level of the normal stresses with the turbulent energy in the figure, the normal stress in the streamwise direction is a factor of round 1.5 lower than the turbulent energy. Thus, a correlation between the normal stress in the streamwise direction and the turbulent energy is found to be approximately;

$$k = \frac{3}{2}(u'u') \quad (3.29)$$

During the measurements conducted in the thesis, only the normal stress in the streamwise direction, $u_x'^2$, will be measured/calculated.

[16, 17]

3.4.2. Integral length scale

The fluctuating part of the velocity at time t can be related to the corresponding value at the time $t + \tau$ by the normalized auto-correlation function $R_{uu}(\tau)$ for a time series $u'(t)$. This function then provides information about the correlation of the time series with itself for different time lags τ , and can be used to find the integral length scale associated with the average eddy size of the turbulence;

$$R_{uu}(\tau) = \frac{1}{\sigma^2 T} \int_{t=t_0}^{t=t_0+\tau} u(t)u(t + \tau)dt \quad (3.30)$$

The function decreases to 0 as τ increases, and has its maximum at 1 when $\tau=0$. When integrating Equation (3.30) from zero time lag to the first zero crossing one obtain the integral time scale T_u ;

$$T_u = \int_{\tau=0}^{\tau=\tau_{cross}} R_{uu}(\tau)d\tau \quad (3.31)$$

This time scale provides a measure of the duration over which velocities are correlated, and can further be used to find the integral length scale xL_u at a given point;

$$^xL_u = T_u U_{mean} \quad (3.32)$$

where the U_{mean} is the streamwise mean velocity.

The integral length scale provides a measure of the extent of the region over which velocities are appreciably correlated. In other words, the average size of eddies in the streamwise direction, indicating the scales of eddies containing the major part of the kinetic energy.

The cross correlation between two measurement points in a flow can also be obtained by the use of Equation (3.30). Instead of using time lag, one of the time series, or measurement points, are used as a reference, while the other time series is used as the delay expression. This will give a delay as the distance between the two measurement points, and hence the cross correlation between the two points in the flow. Further, a time delay can be used on the second time series, and thus obtain a cross correlation both in space and time.

The integral length scale in the vertical direction, L_{uuz} , is normally shorter than in the streamwise direction L_{uux} . The ratio between them, L_{uux}/L_{uuz} , is usually found to be 2. [18]

There have been suggested several relationships on how the surface roughness and the length scale are related. It is known that the integral length scale in the atmospheric boundary layer decreases with increasing surface roughness, and that it increases with increasing height up to 200-300 m above the ground. A recommended relationship, given by ESDU, is commonly used to estimate the integral length scale in an atmospheric boundary layer;

$${}^xL_u = 25 \frac{z^{0.35}}{z_0^{0.063}} \quad (3.33)$$

where z is the height above ground and z_0 is the surface roughness.

The length scale to the energy-containing eddies can also be defined by using an energy spectrum. In an energy spectrum the wave number is the domain and it indicates how the energy is distributed over length scales (inverse wave number).

[15, 17]

3.4.3. Power spectral density function

The strength of the variation in a time series as a function of frequency can be described by using power spectral density function (PSD). The dimension of the function is represented by power per unit of frequency, and when analyzing a velocity time series the unit will be m^2/s . PSD clearly show at which frequencies the variations are strong, and at which frequencies variations are weak. The computation of PSD is done by using a Fast Fourier Transform (FFT). PDS can be very useful for detecting and identifying oscillatory signals in a time series and to find their amplitudes.

When considering the time series of velocity, the spectral energy density, E_{uu} , can be integrated over all frequencies by;

$$\sigma_u^2 = \int_0^\infty E_{uu}(f) df \quad (3.34)$$

This can further be normalized, giving the normalized power spectrum;

$$\Phi_{uu}(f) = \frac{E_{uu}(f)}{\sigma_u^2} \quad (3.35)$$

It is common to rewrite the normalized power spectrum to give a total area under the curve Φ_{uu} versus f equal to 1;

$$\int_0^\infty \Phi_{uu}(f) df = \int_0^\infty f \Phi_{uu}(f) d[\ln f] = 1 \quad (3.36)$$

This way the area under the curve between two frequencies correspond to the fraction of the variance contained in that range of frequencies. However, the wide range of values will result in a figure where the data is compressed to the axis. By modifying the curve by plotting $f \Phi_{uu}$ versus $\ln f$ the curve will be readable, and the characteristics of the area under the curve will be conserved.

The peaks that occur in the power spectral density function represent something repeating in a time series. In the wake of a three blades horizontal axis wind turbine it is normal to obtain three distinct peaks; one at the rotational frequency of the turbine, another at two times the rotational frequency and one at three times the rotational frequency. These are the so called $3P$'s. The first peak represents something occurring once within every rotation of the turbine, the second peak something occurring two times and the third something occurring three times within every rotation.

The turbulence spectra must, according to the Kolmogorov law, approach an asymptotic limit proportional to $f^{-5/3}$ at high frequencies. When plotting the range of frequencies as $\ln f$ versus $\ln f \Phi_{uu}$ the sub range of the spectrum will be proportional to this limit, which can be seen as a straight line with slope $-5/3$. There are two commonly used models for the spectrum of the longitudinal component of turbulence that tends to this asymptotic limit; von Karman spectra and Kaimal. Both models use a length scale L_u . They are defined as given in Equation (3.37) and (3.38) respectively.

von Karman;

$$\frac{f E_{uu}(f)}{\sigma_u^2} = \frac{4f \frac{L_{2u}}{U_{mean}}}{\left(1 + 70.8 \left(f \frac{L_{2u}}{U_{mean}}\right)^2\right)^{\frac{5}{6}}} \quad (3.37)$$

Kaimal;

$$\frac{f E_{uu}(f)}{\sigma_u^2} = \frac{4f \frac{L_{1u}}{U_{mean}}}{\left(1 + 6f \frac{L_{1u}}{U_{mean}}\right)^{\frac{5}{3}}} \quad (3.38)$$

Here, the length scales L_{1u} and L_{2u} must be related by the ratio $L_{1u} = 2.329L_{2u}$ to have the same high-frequency asymptotic limit. f is the frequency and U_{mean} is the mean wind speed at the point of interest in the above expressions.

The von Karman spectrum coincides well with description of turbulence in wind tunnels, while the Kaimal spectrum gives a better fit to empirical observations of atmospheric turbulence. Thus, it have been suggested that the von Karman spectrum gives a good representation of atmospheric turbulence above about 150 m.

[10, 18, 19]

3.4.4. Grid turbulence

In a flow with no mean velocity gradients, there will be no production of turbulence, and as a result homogenous turbulence will decay. In a wind tunnel, a good approximation to decaying of homogenous turbulence can be achieved by placing a grid in a uniform flow. This will create a flow where the statistics of the flow only will vary in the direction of the flow, and the turbulence will evolve with time, $t = x/U_{mean}$, where t is time, x is the position downstream the grid, and U_{mean} is the mean velocity of the flow.

It is found that the normal stresses and the turbulent kinetic energy in a flow with grid turbulence decay as power laws. This can be written as;

$$\frac{k}{U_{mean}^2} = A \left(\frac{x - x_0}{M} \right)^{-n} \quad (3.39)$$

where k is the turbulent kinetic energy, U_{mean} is the mean velocity of the flow, A is a constant dependent on the geometry of the grid (C_p) and the Reynolds number, n is a decay exponent with values typical in the range between 1.15 and 1.45, x specifies the position downstream the grid, and M is the distance between the centerlines of one opening in the grid, see Figure 3.3.

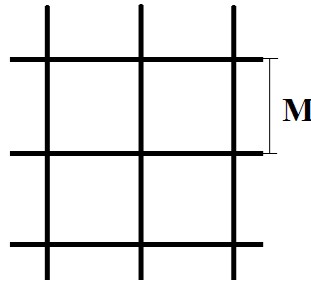


Figure 3.3: General grid

The Reynolds number of the flow will decrease as the turbulence decays downstream the grid, and eventually the viscous effects will dominate, unless there are other turbulence production mechanisms introduced to the flow.

[17]

3.5. Wind turbine wakes

The wake of a wind turbine can be defined as the region behind a wind turbine where the wind velocity has decreased compared to the free stream velocity upstream the turbine. Immediately behind the turbine, the region with the reduced wind speed will be slightly larger than the turbine itself. The wake is in principal generated by the loss of momentum due to the force on the fluid by the wind turbine, directed in the upstream direction. The reduction in the velocity is in other words directly related to the thrust coefficient of the turbine.

The wake of a wind turbine is a highly complex flow, influenced by numerous properties, e.g. the shape of the turbine blades and turbine, operating condition, loads acting on the turbine blades, surrounding turbulence and the velocity profile of the upstream air. However, some of the properties give the wake of the turbine its characteristics such as the tip and root vortices.

When air passes over a blade, the air will try to even out the pressure difference over the blade, resulting in a flow going from the high pressure side, passing the tip of the blade to the low pressure side. This will give a reduced lift force towards the tip of the blade. Further, there will be induced spanwise velocity components over the blade. This will create vortex sheets behind the blade, which tend to roll up in large wingtip vortices distributed along the span with low pressures and high velocities. The downwash has the effect of “tilting” the undisturbed air so that the effective angle of attack is reduced. This results in an additional drag component known as induced- or vortex drag, or drag-due-to-lift. Figure 3.4 visualizes two revolutions of tip vortices for a two-bladed rotor.

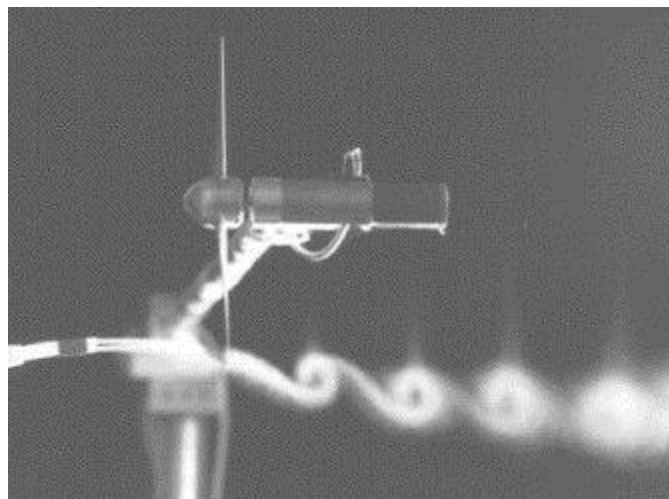


Figure 3.4: Flow visualization experiment at TUDelft, showing two revolutions of tip vortices for a two-bladed rotor [2]

The lift force generated by the blades on a wind turbine can be attributed to a distributed bound vortex by the Kutta-Joukowski law. This bound vortex causes the pressure difference over the turbine blades and thus the lift force, by creating a jump in the tangential velocity over the blades. The Kutta-Joukowski law can be used to describe the strength of the tip vortices created by the blades;

$$\Gamma = \frac{L}{\rho U_\infty} \quad (3.40)$$

where Γ is the strength of the vortex, L is the lift force, U_∞ is the free stream velocity and ρ is the air density. The strength of the tip vortices is, among other influences, dependent on the loads acting on the turbine blades. [20]

The tip vortex in the wake is known to first decrease in diameter, due to vortex stretching as a result of wake expansion, and then increase in diameter due to viscous effects [21]. The tip vortices follow a helical path with rotation opposite of the rotor. This is due to the fact that the airflow gives torque to the wind turbine, and as a result, an angular momentum to the flow in the wake of the turbine. The energy extraction then creates some kinetic energy which will rotate the wake in the opposite direction to the rotor. The tip and root vortices give a periodic upstream boundary condition to the wake, while downstream in the wake the tip and root vortices may interact and pair with each other, or break up.

The tip vortices have been found to significantly affect the turbulent structures in the wake, and also have a strong influence on the wind turbine rotor as a whole [2]. Tip vortices spirals shed from blades with different pitch angle tend to have their own path and transport velocity. This might result in that one or two tip vortices catches up with the other after a few revolutions, and thus become entwined as one. The merging of the tip vortices is possible due to that they rotate in the same direction. [2]

The turbulent flow in the wake of a wind turbine is, as mentioned, complex. The velocity destabilizations in the wake is a combined result of turbulence contribution originating from the wake generated shear, conventional background atmospheric turbulence, blade bound vorticity effects and the meandering movement of the wake. The turbulence in the wake which is generated by the turbine is of relatively high frequency and decays rather quickly, and the length scale of the turbulence introduced by the wake is in the order of the rotor diameter [7]. In 1983, Bossanyi developed a theoretical model which describes how this turbulence might decay. As explained in previously sections, large eddies give rise to smaller eddies, thus the turbulent energy moves to higher and higher frequencies, until it dissipates as heat. The model developed by Bossanyi predicts a faster rate of decay in high ambient turbulence intensities and in low winds.

The wake of a wind turbine is typically divided into two regions; near and far wake, where the near wake is the region up to approximately one rotor diameter downstream the turbine. In this region the presence of the rotor is apparent by the blade aerodynamics, number of blades, 3-dimensional effects and the tip vortices, determining the performance of the turbine. The far wake is the area beyond the near wake. Figure 3.5 shows how the wake of a wind turbine might be divided into a near and far wake.

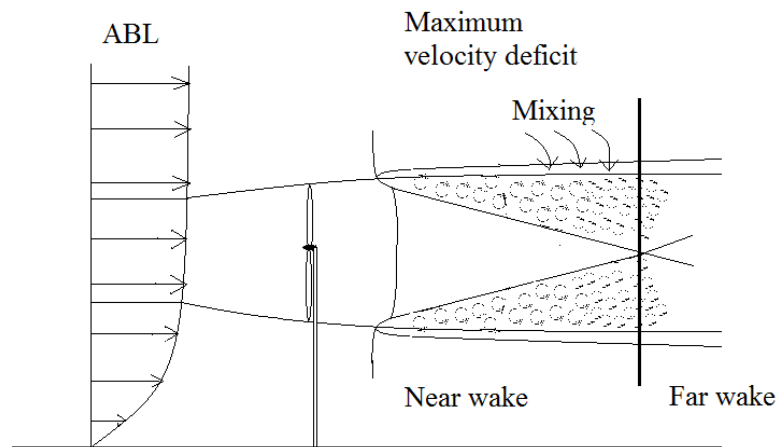


Figure 3.5: Velocity profile in the wake of a wind turbine

The velocity difference between the air outside and inside the wake creates a shear layer. In this shear layer there are formed eddies and the layer thickens when moving downstream in the wake. In the near wake, when conducting single point measurements of the wake profile, it appears two peaks with higher turbulence intensity which, in the far wake, is no longer evident, see Figure 3.5. The wake and the surrounding flow will start to mix, and the region of the mixing will spread inwards to the center of the wake, as well as outwards which makes the width of the wake increase. In this way the wake becomes broader, but shallower until the flow has fully recovered far downstream the turbine, and the velocity deficit in the wake is eroded. The diffusion of the kinetic energy is thus greatest in radial direction when dividing the diffusion into streamwise and radial direction. The diffusion in radial direction will therefore contribute most to the diffusion, which then will smear out the velocity gradients when a wind turbine is exposed to a turbulent incoming flow.

Figure 3.6 visualizes a smoke trail from the tip of the blade when smoke is emanated from the tip of the turbine blade. From this smoke trail it is not clear whether the smoke trail reveals the path of the tip vortex or some streamline in the tip region. However, it illustrates how the outer region of the wake of a wind turbine evolves downstream the turbine. In this figure the wake hardly expands. This is due to a very low thrust value during the experiment.

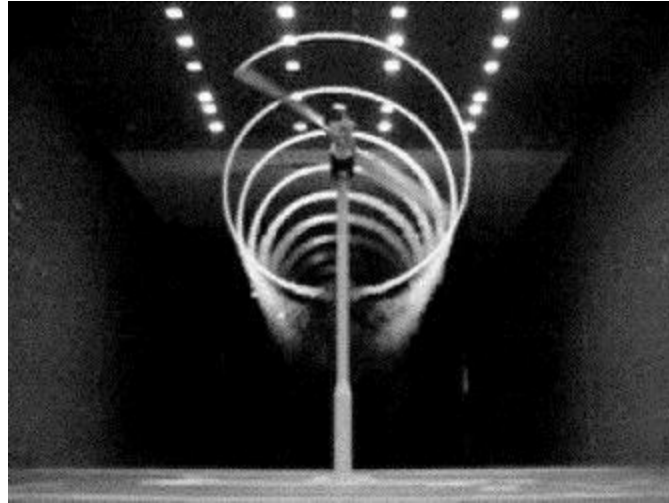


Figure 3.6: Flow visualization with smoke grenade in tip, revealing smoke trails for the NREL turbine in the NASA-Ames wind tunnel [2]

The maximum velocity deficit has been estimated to be attained after 1-2 diameters, or even further downstream at low ambient turbulence levels, and the expansion region length about 1 diameter [22]. In 2006, D. Medici and P. H. Alfredsson conducted measurements on a wind turbine wake where they studied the velocity field in the wake of a two-bladed model wind turbine under different conditions [3]. One of their findings was that the wake is substantially changed by the presence of free stream turbulence. The wake of the model turbine had a faster recovery of the velocity defects due to a higher energy mixing and a shorter persistence of the tip vortices when the turbine was subjected to free stream turbulence.

The forces acting on the turbine affects the wake of the wind turbine. For instance, a higher thrust force acting on the rotor will result in a lower velocity in the wake, and thus greater shear between the flow velocities outside and inside the wake. This means that a changed tip speed ratio or pitch angle will change the total momentum deficit in the wake. E.g. a higher thrust coefficient will result in a larger the wake expansion.

[17, 20]

3.5.1. Bluff body wakes and wake meandering

The wake of a wind turbine can be viewed as a wake of a bluff body. A bluff body wake has the characteristics of self-similarity far downstream, at round 50 diameters, and the development of the wake downstream can be described by an appropriate normalization. The wake “remembers” the shape of the solid body in the form of the larger eddies that travels downstream. The large scale vortex shedding from the body is connected to a wake meandering, described by the Strouhal number. However, in the wake of a wind turbine the tip vortices shield the wind turbine wake and will decay turbulent mixing.

In many cases it appears vortical structures in the wake of a solid body due to instability processes. An example of such a vortical structure is the well-known von Karman vortex street, which appears in the wake of a circular cylinder when the Reynolds number exceeds 44. It has been shown that the shedding frequency of the von Karman vortex street can be expressed by the non-dimensional Strouhal number, and is found to be constant over a wide range of Reynolds numbers. [23]

The term wake meandering is used for large scale movements of the entire wake. The meandering phenomenon is important due to possible increased fatigue and extreme loads in wind farms by causing the wake to sweep in and out of the rotor plane of downstream turbines. The meandering phenomenon is not well understood, but there are believed to be two main possible reasons for its formation. As mentioned, atmospheric turbulence consists of eddies of different size, and it is suggested that the meandering is caused by eddies whom are large compared to the size of the wake, transporting the wake as a whole. The smaller eddies, smaller than the rotor diameter, is then believed to be responsible for diffusive effects in the wake only. The second suggestion is based on that the instinct instabilities in the wake is characterized by a periodic vortex shedding within the wake, as observed in the wake of a bluff body. In 2012, España, Aubrun, Loyer and Devinant conducted a wind tunnel study of the wake meandering downstream of a modeled wind turbine [24]. The study was based on a modeled wind turbine by the actuator disk concept in a wind tunnel with modeled atmospheric boundary layer. Based on their experimental setup, the results showed that the wake meandering is certainly inextricably linked to the large turbulent eddies in the atmospheric boundary layer. However, further investigation on the meandering phenomenon is necessary.

[3, 20]

3.6. Hot-wire

The measurements in the wake of the model wind turbine in this master thesis is to be conducted with a hot-wire array. A hot-wire anemometer is a measuring device used for many years in fluid mechanics as a research tool, despite its intrusiveness in the flow stream.

The hot-wire anemometer has the ability to describe the turbulent behavior in a flow stream in detail. It consists of the sensor, an electrically heated wire exposed to the fluid flow, and electric equipment which transforms the output of the sensor to an electric signal. The wire is soldered to two support needles, and is normally in the size of 1-3 mm in length and 5 μm in diameter, see Figure 3.7.

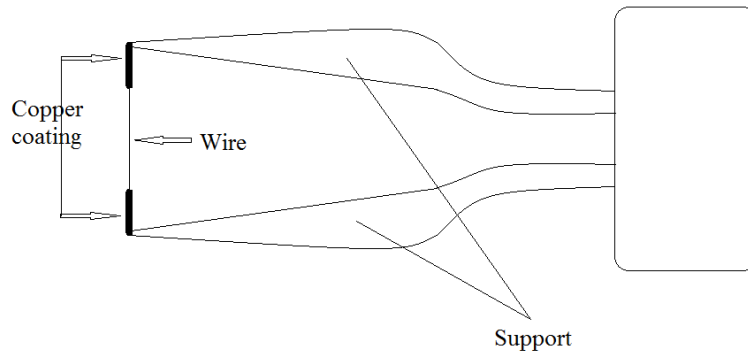


Figure 3.7: Hot-wire probe

Using the principle of heat transfer, derived from Fourier's law and the conservation of energy, the velocity of the airflow can be determined by;

$$\text{Supply} = I^2 R_w = \pi D l h (T_w - T_a) = \text{Dissipation} \quad (3.41)$$

where I is the current running through the wire, R_w is the resistance at operating temperature T_w , h is the heat transfer coefficient and D and l is the diameter and length of the wire. The heat transfer coefficient is related to the thermal conductivity of the fluid, k , by the Nusselt number given by;

$$Nu = \frac{hD}{k} \quad (3.42)$$

Combining Equation (3.41) and (3.42) gives;

$$I^2 R_w = \pi l k (T_w - T_a) Nu \quad (3.43)$$

As the fluid passes the heated wire it will cool down the wire by heat transfer, which will be a function of the fluid velocity. This will give a relationship between the fluid velocity and the electrical output which can be detected by an electronic circuit.

The Nusselt number is again a function of the Reynolds number and Prandtl's number. There have been conducted many investigations on how these characteristic properties in the flow are related and it has been tried to derive a universal expression for the cooling of cylinders. This has led to numerous expressions for the Nusselt number based on different ranges of Reynolds numbers. Even though one has failed to derive one universal expression, the numerous investigations have shown a similarity in the expressions for the Nusselt number;

$$Nu = A + BU^n \quad (3.44)$$

In this term A is the natural convection term and BU^n is forced convection. When considering that the wire resistance is a function of its temperature, an expression for the resistance in the wire can be derived;

$$R_w = R_a[1 + b_1(T_w - T_a)] \quad (3.45)$$

Combining Equation (3.43), (3.44) and (3.45) one obtains the expression;

$$b_1 \frac{I^2 R_w R_a}{R_w - R_a} = A + BU^2 \quad (3.46)$$

An actual value of the heat transfer can be obtained by this expression, either by keeping I constant or R_w constant in the control circuit.

As seen from the above expression, there are two basic methods of using a hot-wire anemometer as a measuring device; constant current and constant temperature. The constant current method, see Figure 3.8, is as obvious as it sounds, constant current supply through a measurement bridge. In the bridge there are two equal resistors, RI , and an adjustable resistance R , which is set to be equal to the resistance of the warm hot-wire (usually 1.8 times the cold wire). By increasing the supplied current the bridge will become balanced. As the fluid passes the hot-wire, the resistance in the wire will change due to heat transfer and the bridge will become unbalanced. This will give a voltage output which is linked to the velocity by the expressions seen above, and the hot-wire anemometry is ready to be calibrated when balanced.

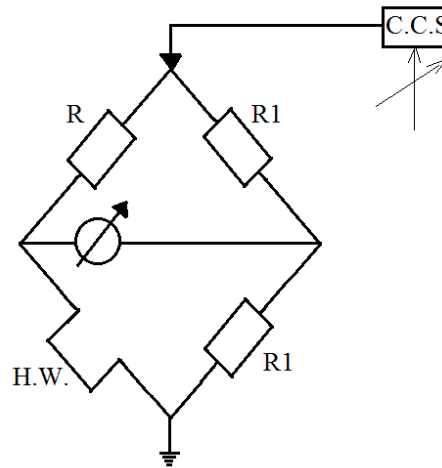


Figure 3.8: Hot-wire control circuit, constant current

When using the constant temperature method, the temperature, and thus the resistance in the wire are held constant by varying the supplied current, see Figure 3.9. The level of supplied current is determined by monitoring the voltage over the bridge and keeping the bridge balanced. The output from the bridge is amplified and the amplified output, used to keep the wire temperature constant, is then a function of the fluid velocity. As when using the constant current method the wire is calibrated by adjusting the resistance R , normally to $1.8 \cdot R_{HW,C}$, depending on the desired wire temperature.

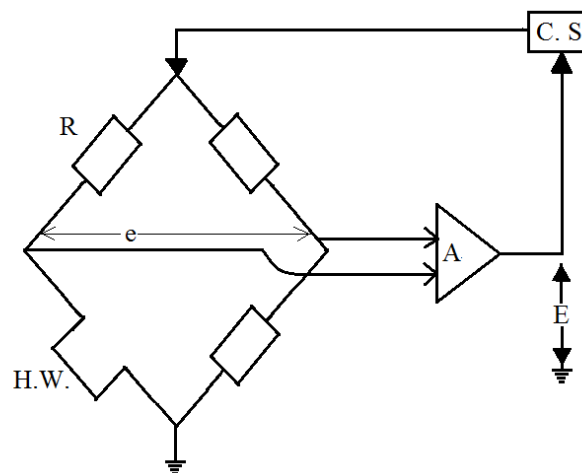


Figure 3.9: Hot-wire control circuit, constant temperature

The constant temperature method is normally the preferred method, due to its high frequency response compared to the constant current method. When using hot-wire anemometer the aim is normally to detect and follow the rapid velocity fluctuations in the flow. Using the constant current method, the actual change in the velocity will not be as good described since the response of the sensor will lag behind due to the thermal inertia in the sensor. This can cause a problem when determining the frequency response of the system.

When using the constant temperature method, the temperature variation in the wire is much smaller, leading to an almost negligible thermal inertia in the wire when determining the frequency response.

When conducting measurements with hot-wire probes it is important to optimize the anemometer response to the mean fluid velocity at which the probe is likely to operate. The instantaneous velocity of a flow can be found if the frequency response is flat over a region that covers all the spectrum of frequencies of interest. Before initiating hot-wire measurements it is also important to investigate if there is any noise on the signal. The hot-wire is sensitive to noise, both white and from other electrical instruments, thus a low-pass filter is often used to filtrate frequencies above the region of interest.

In the experiments conducted in this master thesis, the constant temperature method will be used.

[25]

4. The experiments

During this master thesis there have been conducted many initial measurements in order to get the correct conditions in the wind tunnel, and to prepare for the final measurements in the wake of the model wind turbine. In this chapter, the initial experiments with a description of the method and results will be presented after an introduction to the equipment and setup used during the experiments in this study.

The results from the final experiment will be presented and discussed in Chapter 5.

4.1. Setup and Equipment

The signals, or the acquiring voltage from the equipment, were monitored with an oscilloscope to be able to detect any abnormal behavior during the measurements.

4.1.1. Model wind turbine

The wind turbine in question is a three bladed horizontal axis turbine. The rotor of the turbine is connected to a nacelle which is placed on top of a tower made out of four cylinders of different size, mounted on top of each other, see Figure 4.1. The height of the tower is 0.725 m above the wind tunnel floor, and the front area of the tower is approximately $5.6E-2 \text{ m}^2$. The nacelle is circular and has a diameter of $9.0E-2 \text{ m}$ and is 0.43 m long.



Figure 4.1: Model wind turbine

The blades are connected to an almost semi spherical hub with a diameter of $9.0E-2$ m placed in front of the nacelle. The diameter of the rotor is 0.894 m and the lengths of the blades are 0.45 m. The blades can be pitched about the blade quarter chord with pitch angle θ_p . The center of the rotor is 0.817 m above floor level in the wind tunnel. At the rear of the nacelle is a cap that is linked to the rotor. The cap is formed like a sphere, with a diameter of $9.6E-2$ m, and is connected to a transmission belt that transfers the moment of a generator located under the floor of the wind tunnel. This mechanism makes it possible to control the rotational speed of the rotor by having the generator connected to a full-frequency converter. The moment on the transmission axis is measured by a torque gauge located inside the nacelle and the acquiring voltage is logged by a computer during experiments, using the program LabView.

The forces acting on the wind turbine is measured by a force plate which the model wind turbine is placed upon. The force plate is placed underneath the wind tunnel and can measure forces in three dimensions. During the experiments in this thesis, only the thrust force will be measured by this force plate.

The pitch angle of the blades was adjusted to 0° by using a protractor before initiating the measurements. The blades of the turbine use the NREL (National Renewable Energy Laboratory) S826 airfoil along the entire span. The NREL S826 airfoil, see Figure 4.2, is designed for a Reynolds number of $2.0E+6$, and with two primary objectives; a high maximum lift coefficient, insensitive to leading-edge roughness, and a low profile-drag coefficient. [26]

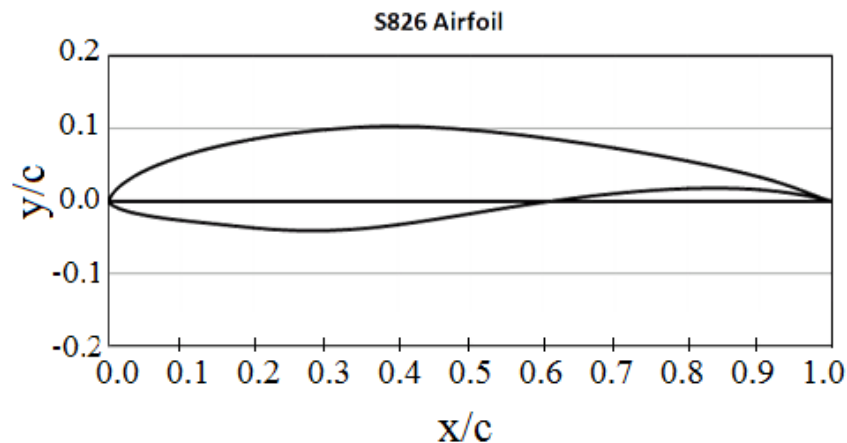


Figure 4.2: Airfoil S826 [26]

To achieve an airfoil that is insensitive to leading-edge roughness, the profile is highly curved on the suction side close to the leading edge, resulting in a suction peak to appear. This will give a boundary layer that is turbulent over most of the suction side by promoting transition close to the leading edge independent of free stream turbulence and roughness. [26]

The blades on the wind turbine model is designed for an angle of attack of 7.0° at a tip speed ratio 5, with corresponding lift and drag coefficients of 1.2756 and $1.35E-2$ respectively. [27]

The model blockage ratio, defined as the rotor swept area of the turbine divided by the cross-sectional area of the wind tunnel, is 13 %. The recommended maximum is 10 % to avoid tunnel interference on the wake expansion, thus the ratio during this experiment is a bit high. [28]

4.1.2. Wind tunnel

The wind tunnel has a test section that is 2.7 m wide, 11.1 m long and 1.9 m high. A sketch of the tunnel is given in Figure 4.3. Since the model turbine is developed for testing at NTNU, the dimensions of the turbine and the wind tunnel is a good match. The tip of blades on the turbine is at a distance of 0.37 m from the nearest wall. This distance should be long enough to prevent the boundary layers caused by the wind tunnel walls to affect the performance of the turbine.

To measure the free stream velocity, the venturi effect was used. The wind tunnel has a contraction upstream of the test section, $A_1/A_2 = 4.36$, and the pressure difference was measured using pitot tubes, pressure transducer and a alcohol manometer.

The temperature in the wind tunnel during the experiments was measured by the use of a regular digital thermometer placed on the wall inside the wind tunnel. During the experiment it was a temperature rise in the tunnel, which is a result of the heat generated by the wind tunnel fan. The total atmospheric pressure was found by a precision mercury manometer.

The free stream velocity during the measurements involving the wind turbine was set to round 10 m/s. This is based on previous experiments conducted in the wind tunnel. [18]

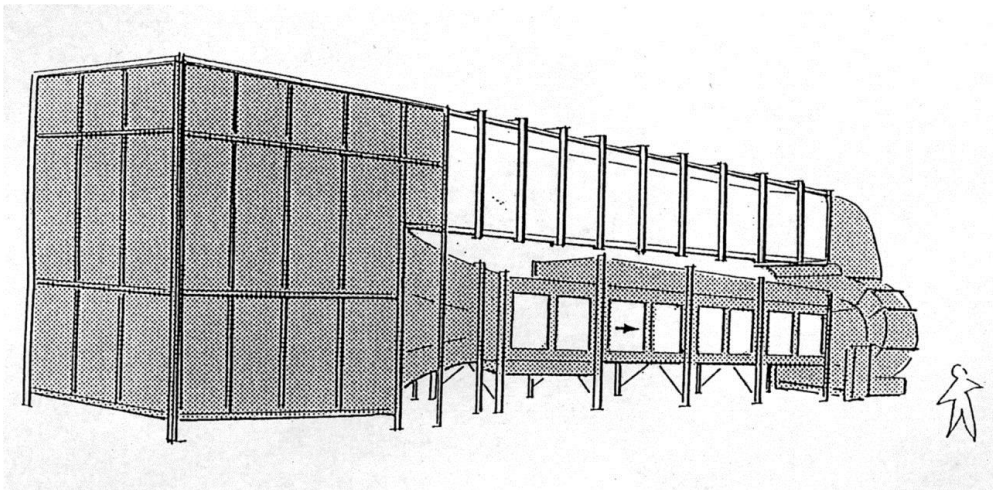


Figure 4.3: Sketch of wind tunnel [29]

4.1.3. Grid

A grid was placed in the inlet to the test section to create a free stream with turbulence intensity typical for atmospheric turbulence intensity in the wind tunnel. Figure 4.4 shows a sketch of the grid with its dimensions.

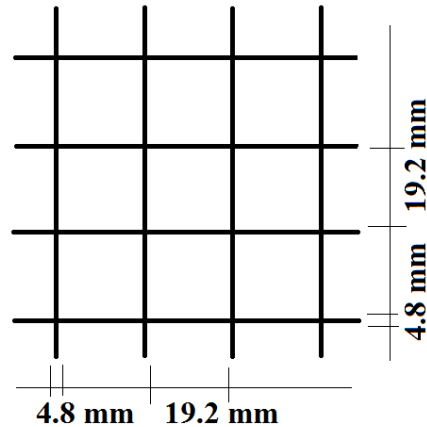


Figure 4.4: Sketch of a section of the grid with dimensions

The boards have a width of 4.8×10^{-2} m and the width of the openings are 0.192 m x 0.192 m, giving a mesh size of $M = 0.24$ m. There are in total 10×7 boards, which give a total of 11×8 openings, and a solidity of 0.33 (blocked area / total area). The drag coefficient across the grid was approximately $C_D \approx 2$. The turbulence generated by the grid is expected to be more or less homogeneous in front of the model wind turbine.

When referring to the case without grid turbulence during the report, the grid was laid down on the wind tunnel floor in the front of the model wind turbine. This will create a boundary layer which will grow downstream in the test section. The thickness of this boundary layer is unknown and it might affect the experimental results. This effect is neglected when analyzing the measurements, and can thus be a source of error in the data.

4.1.4. Hot-wire anemometry

The hot-wire probes used during the experiments were all made from 10 % rhodium and 90 % platinum. The wires have a diameter of $5 \mu\text{m}$ and a length of 1 mm, which gives an L/D ratio equal 200 . The cold resistance in the wires varied from 5.6Ω to 5.7Ω . The temperature of the wires was set to 300°C and 350°C giving a overheat ratio of 1.4732 and 1.5577 respectively, when the ambient temperature was 20° .

The hot-wire probes were all connected to anemometers which generates the voltage signal (balancing the bridge). The anemometers included both filter and amplifier. The signals from the anemometers were carefully supervised on oscilloscope during measurements, as well as being logged in LabView.

4.2. Calculations

During the measurements and the treatment of the data there were some calculations that were repeated for several experiments;

The total atmospheric pressure was found by using equation;

$$P = \rho gh \quad (4.1)$$

Using the pressure and the logged temperature in the wind tunnel during the experiment, the density of the air was calculated by;

$$\rho_{air} = \frac{P}{RT} \quad (4.2)$$

Further, the free stream velocity was calculated using the pressure difference measured using the Pitot probe, the rate between the areas of the contraction in the wind tunnel and the density;

$$U_{\infty} = \sqrt{\frac{2\Delta P}{\rho(1 - \frac{A_2}{A_1})^2}} \quad (4.3)$$

During most of the measurements the acquiring voltage from the Pitot probes in the contraction was used to calculate the free stream velocity.

The rotational velocity, RPM, logged using LabView, the reference velocity, U_{ref} , and the radius, R , were used to find the tip speed ratio by;

$$\lambda = \frac{\frac{2\pi RPM}{60} * R}{U_{ref}} \quad (4.4)$$

A free stream Reynolds number was obtained using the rotor diameter, the free stream velocity calculated upstream of the turbine and ideal gas law;

$$Re = \frac{U_{\infty} d P}{\mu R T} \quad (4.5)$$

where the dynamic viscosity was calculated based on Sutherland's equation;

$$\mu = 1.458 * 10^{-6} \frac{T^{1.5}}{T + 110.4} \quad (4.6)$$

This formula is valid for temperatures below 3000K when the air is independent of pressure [13].

Most of these calculations were computed during the experiments and an overview of the results is given in the sections describing the experiments.

4.3. Calibration

4.3.1. Forces

The force plate used to measure the thrust force acting on the turbine needed to be calibrated. To get a calibration curve that covered the maximum expected thrust force, $C_{T,max}$ was calculated based on earlier measurements conducted on the turbine to find T_{max} . Using Equation (3.3) with $U = 10$ m/s and $C_{T,max} = 2.4$, the maximum thrust was found to be almost 92 N, which can be rounded up to 10 kg. This result was used to determine the maximum weight needed in the calibration.

For the calibration of the force plate, weights in a range between 0.5 kg to 10 kg were used in both ascending and descending order. Figure 4.5 shows a picture from the calibration process of the force plate. LabView was used to log the acquiring voltage at a frequency of 100 Hz in 30 seconds, resulting in a total number of 3000 samples. The calibration coefficient was found to be 8.3019 N/V. The calibration data and the appurtenant calibration curve can be found in Appendix A.1.1.



Figure 4.5: Calibration thrust gauge

When calibrating the torque gauge, the maximum expected torque was found to be approximately 2 Nm based on earlier measurements conducted on the turbine. Dividing this by the radius of the rotor, $R = 0.45$ m, gives a maximum value of 4 N, which is equal to approximately 400 grams.

In the calibration of the torque, weights in the range between 0.05 kg to 0.5 kg were used. The weights were placed on a small weight connected on the tip of the turbine blade. The measurements for the calibration curve were conducted by first increasing the weights, and then decreasing with the same weights to account for hysteresis. The acquiring voltage was logged in LabView using the same frequency and sampling time as when calibrating the thrust gauge. The calibration coefficient was found to be -0.2062 Nm/V. The calibration curve and data can be found in Appendix A.1.2

4.3.2. Free stream velocity

The free stream velocity was measured using a Pitot probe placed on a traverse inside the wind tunnel, and the contraction of the wind tunnel was used as a reference. Both the pressure transducer for the Pitot probe and the contraction of the wind tunnel was calibrated using an inclined alcohol manometer, see Appendix A.1.3. and A.1.4. for the calibration data.

To find the correct free stream velocity where the turbine was placed in the tunnel during measurements, the same pressure transducer was used to calibrate both the Pitot probe on the traverse and in the contraction of the wind tunnel. Since the velocity given by the contraction corresponds to the velocity at the inlet to the test section, and the turbine was placed 3.75 m downstream of the inlet (decided after initial measurements), the velocity calculated based on the contraction needed to be corrected. When calculating the power- and thrust coefficients the free stream velocity is needed, and it is also necessary to have a reference free stream velocity to the measurements conducted in the wake of the turbine. Calibration data can be found in appendix A.1.3. and A.1.4.

Velocity measurements from the Pitot probe placed at $x = 3.75$ m in an empty tunnel and the contraction was conducted both with and without the grid installed in the inlet to the test section. The relationship between the two was $U_{\text{pitot}}=U_{\text{contraction}}/0.99$ without the grid, and $U_{\text{pitot}}=U_{\text{contraction}}/1.15$ with the grid installed. U_{pitot} will then represent the free stream velocity where the turbine was placed in the tunnel, and will be used as U_{ref} . The ratios between the velocities are given together with the calibration data for the contraction of the wind tunnel.

An uncertainty analysis was conducted on the reference velocity. This gave an estimated uncertainty of ± 0.6 % with a confidence interval of 95 %. The method used to estimate the uncertainty is given in appendix A.3.

4.3.3. Hot-wire

A sketch of the setup used during the hot-wire calibration and measurements is given in Figure 4.6. The figure only illustrates the use of one hot-wire probe.

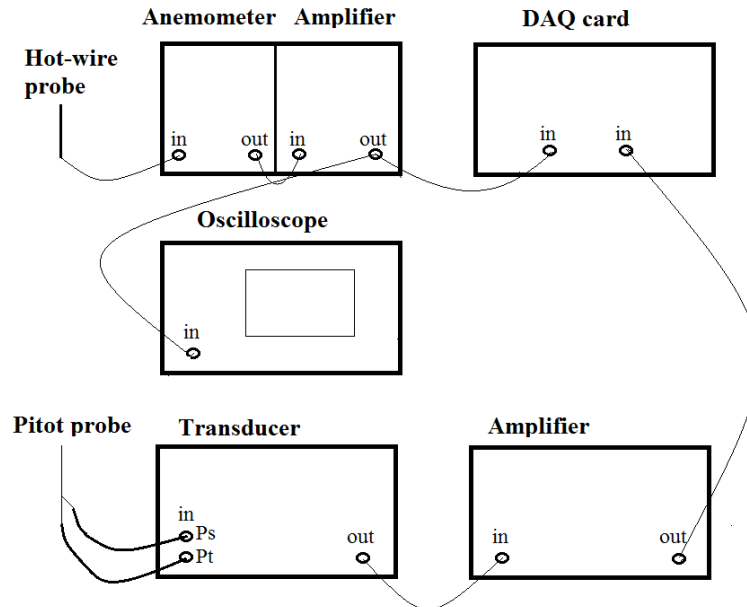


Figure 4.6: Setup hot-wire measurements

The Pitot probe attached to the traverse in the wind tunnel was used to calibrate the hot-wire anemometry. When calibrating the hot-wire anemometry, a cup mounted on a stand was placed around the hot-wire probe when taking zero point measurements in order to eliminate any disturbances in the wind tunnel.

When calibrating several hot-wire probes attached to a rake, a garbage can was used in the same way during the zero point measurements. It was taken two zero point measurements, the first at last calibration point, for each calibration of the hot-wire anemometry. The probes were calibrated every second hour, due to drift in the temperature in the wind tunnel, and that the wire has a tendency to attract dust, which can affect the measurements. The hot-wire will also “get old” due to that the heat will slowly change the crystal structure in the wire, which will affect the resistance in the wire. [18]

After the zero point measurement, the wind speed in the wind tunnel was gradually increased up to round 20 m/s, and measurements were taken at different velocities. The sampling frequency used during the calibration of the hot-wire probes was 20 kHz and a sampling time and 45 seconds.

For all experiments involving the use of with hot-wire anemometry, in-house programs were used for fitting polynomials to the velocity calibration data and converting the acquiring voltage from the hot-wire probes to time series of velocities vectors. These two programs, *utilp* for calibration and *hwconv* for conversion, have been used as standard programs at the institute for many years. The programs are written in Fortran and include temperature correction.

The calibration curve of a hot-wire is non-linear, and has approximately the shape of 4th order polynomial with maximum sensitivity at low velocities. An example of a calibration curve, with calibration coefficients, is given in Appendix A.1.5. The calibration coefficients are found by best fit calculations.

4.4. Experiments

In order to learn a correct measurement technique using hot-wire anemometry, an initial experiment was carried out on a fully developed pipe flow with known results. The experiment was intended as a learning step, where the goal was both to learn how to calibrate the hot-wire anemometry and measure correctly, and to treat the data reasonable. The results were approved by the supervisor before initiating the measurements on the wind turbine model in the wind tunnel. An overview of the results is given in Appendix A.4.

4.4.1. The use of five hot-wire probes

To comprehend how the wake of the model turbine behaves and to be able to detect any meandering, the measurements are based on the position of the tip vortices in the wake. Using 5 hot-wire probes attached to a rake, positioned horizontal relative to the wind tunnel floor, the normal stress, $u'u'$, in the area round the tip vortices can be mapped. Comparing the measurements from one revolution of the wind turbine rotor with the next will make it possible to detect any oscillating movements in the tip vortices, and hence of the wake.

The diameter of the vortices, and width of the location of the three tip vortices in the wake, need to be known in order to be sure to cover the whole area where the tip vortices might meander within the rotations. When using only one hot-wire probe, the results will be a smeared out image of the behavior of the wake. Hence, if the wake of the wind turbine meanders, the centerline velocity deficit measured by an observer will become less than the stationary value, because the measurement point sweeps across a region of the wake profile during the averaging period of the measurement [7]. By using five hot-wire probes, a wider area of the wake can be covered in one measurement, and thus the movement of the vortices can be studied within the measurement range. Using cross correlation between the time series given by the hot-wire probe measurements, one can obtain an indication of how well the flow field at one place in the flow is correlated to another point the flow field in the wake.

By studying the normal stress distribution over the measurement area given by the five hot-wire probes within each rotation of the turbine, a study on the stability in the tip vortices, and hence the wake, can be conducted.

In all the experiments involving the use of hot-wire anemometry, the probes were pointed perpendicular to the mean flow to measure properties in the streamwise direction. All the probes were positioned horizontal relative to the floor of the wind tunnel.

4.4.2. Modeling atmospheric conditions in the wind tunnel

In order to simulate the situation for a full scale wind turbine subjected to atmospheric turbulence, the normal operating conditions needed to be specified. In this master thesis, the simulation of atmospheric conditions in the wind tunnel is based on properties from a full scale wind turbine (tower height, diameter, efficiency etc.) and finding the length scale and turbulence intensity for its typical conditions from theory. Further, the length scale was scaled down to fit the model wind turbine. The model wind turbine has an efficiency round 45 %, so finding a real size wind turbine with the same efficiency was desirable.

Suzlon manufacturer delivers a wind turbine with an efficiency of around 45 % at 11 m/s [30]. The diameter of the turbine is 64 m and at a wind speed of 11 m/s it produces 1.19 MW. The height of the hub is 74.5 m above the ground. Based on the height of the hub and the relationship given by ESDU (Equation (3.33)), the integral length scale was found to be 174.7 m for this turbine in atmospheric conditions, with a surface roughness of 1.0E-3 (sea surface roughness [15]). This is thus only an estimate and seems a bit over predicted. A length scale closer to 100 m would probably be more reasonable [18].

The turbulence intensity offshore at 90 m height is dependent on the surface roughness, but based on a study conducted by Matthias Turk and Stefan Emeis the mean turbulence intensity varies round 4-6 % [31].

The full scale wind turbine and the model wind turbine are scale according to the height of the turbines. The dimensions of the turbines with the scale are represented in Table 4.1.

Table 4.1: Suzlon wind turbine VS model wind turbine

Dimension	Suzlon S66 Mark II - 1.25 MW	Model wind turbine	Scale
MW	1.19	-	-
Diameter [m]	64	0.9	9/640
Tower height [m]	74.5	0.725	29/2980
Efficiency [%]	45	45	1

Using 29/2980 as scaling parameter, the downscaled integral length scale should be 1.7 m for the atmospheric conditions created in the wind tunnel in order to satisfy the correct integral length scale according to the size of the model wind turbine and the recommended relationship given by ESDU. This is however a long integral length scale, and thus not likely to achieve in the wind tunnel due to the restricted size of the tunnel.

4.4.3. Grid turbulence measurements and integral length scale calculations

It was conducted calculations on the geometry of a grid that produces an integral length scale of 1.7 m and turbulence intensity round 4-6 %. The results gave a grid geometry close to an already existing grid at the institute which was used instead of creating a new grid. Figure 4.7 shows a picture taken inside the wind tunnel of the grid and the model wind turbine. The grid covers the whole inlet to the test section, and the dimensions were given in Section 4.1.3.



Figure 4.7: Grid installed in wind tunnel

To measure the integral length scale and turbulence intensity produced by the grid, numerous measurements were taken downstream the grid in the test section. In order to measure the velocity fluctuations and thereby finding the turbulence intensity and properties required to estimate the integral length scale, a hot-wire probe was used. The hot-wire probe was placed in the center of an opening in the grid, 0.775 m above the floor of the wind tunnel, and 1.36 m from each sidewall of the test section. This was done to avoid the vortices shed by the boards of the grid and any disturbances from the boundary layer created by the walls. This height is also close to the height of the center of the turbine rotor. Using a traverse installed in the wind tunnel, the hot-wire probe was traversed downstream with a 0.5 m increment from 0.0 m down to 8.5 m behind the grid. The conditions during the measurements are given in Table 4.2.

Table 4.2: Mean values during grid measurements

Mean values	
Free stream velocity [m/s] (mean value in test section)	8.3
Patm [Pa]	100887.3
ρ [kg/m ³]	1.182
Temperature [°C]	24.5

The acquiring voltage from the hot-wire anemometer, together with the acquiring voltage from the contraction and Pitot probe during the measurements, were logged at 20 kHz, using a filter at 10 kHz (Nyquist theorem), at a sampling time of 60 seconds. The turbulence intensities at each location downstream the grid is given in Table 4.3. Based on these results, the desired turbulence intensity of 4-6 % is located round 3.5 m to 4.0 m downstream of the grid, with a free stream velocity at 8.3 m/s. The mean, maximum and minimum velocities at each location are also given in the table, as well as the normal stress $u'u'$.

Table 4.3: Results from grid turbulence measurements

Distance from grid [m]	U_{mean} [m/s]	U_{max} [m/s]	U_{min} [m/s]	$u'u'$ [m/s] ²	Turbulence [%]
0	15.597	16.540	14.081	0.108	2.108
0.5	9.657	21.781	0.846	6.03	25.429
1	8.821	16.166	2.35	2.091	16.392
1.5	8.512	13.315	4.871	0.949	11.448
2	8.395	12.291	5.437	0.561	8.925
2.5	8.328	11.367	6.026	0.382	7.423
3	8.313	10.814	6.193	0.289	6.462
3.5	8.285	11.065	6.316	0.233	5.83
4	8.281	10.534	6.559	0.189	5.254
4.5	8.302	10.238	6.773	0.157	4.768
5	8.295	9.921	6.822	0.139	4.5
5.5	8.273	9.916	6.785	0.121	4.212
6	8.265	9.764	7.025	0.107	3.955
6.5	8.241	9.577	6.976	0.093	3.704
7	8.244	9.563	7.029	0.085	3.537
7.5	8.191	9.448	6.944	0.078	3.399
8	8.185	9.809	7.098	0.076	3.364
8.5	8.186	9.323	7.174	0.069	3.2

The turbulence intensity does not change significantly with the free stream wind speed. Thus, the fact that the measurements was conducted with a mean free stream velocity at 8.3 m/s, and not 10 m/s as the measurement on the model wind turbine were to be conducted, will not give a significant change the turbulence intensity.

As stated in the theory, grid generated turbulence in a wind tunnel will decay downstream with increasing distance to the grid. This is clearly seen in Table 4.3, where the turbulence intensity is at 25 % at $x = 0.5$ m and 3.2 % at $x = 8.5$ downstream the grid.

To find the integral length scale produced by the grid, the hot-wire probe was traversed in the horizontal direction at $x = 3.5$ m behind the grid, which is where the turbulence intensity produced by the grid is as desired. The probe was traversed from the center of the tunnel, 0.778 m above the wind tunnel floor, with an increment of 0.10 m.

Also during these measurements were the acquiring voltage from the hot-wire anemometry, contraction and Pitot probe logged at a sampling frequency of 20 kHz during a sampling time of 60 seconds, using a filter of 10 kHz. The free stream velocity in the wind tunnel was increased to 10 m/s during these measurements. The temperature, atmospheric pressure and air density during the measurements were the same as for the previous measurements, and are given in Table 4.2.

Using an in-house program, *Spec-mac-big-ASCII*, it was calculated a power density spectrum from the time series to the hot-wire anemometry using Fast Fourier Transform. The frequency and $\Phi_{uu}(f)$ for the time series from the hot-wire anemometry was then obtained. Using Equation (3.37) for the von Karman specter and adjusting the integral length scale, an integral length scale of $L_{uux} = 0.12$ m was found. The two spectrums are given in Figure 4.8.

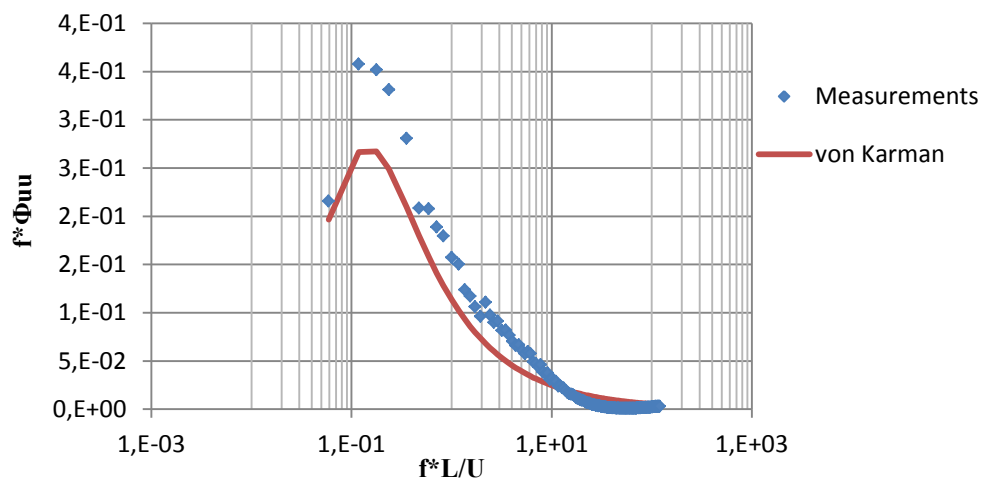


Figure 4.8: Integral length scale compared to von Karman specter

In the figure, $f\Phi_{uu}$ is plotted as a function of the normalized frequency $X = fL/U$ on a semi-log axis.

The length scale was found by adjusting L in such a way that the curves from the measurements and the von Karman specter corresponds, and is just an estimate. In order to get a more accurate integral length scale, additional measurements were conducted using two hot-wire probes simultaneously. One of the probes was places in the center of the wind tunnel, while the other was traversed in the horizontal direction, perpendicular to the streamwise direction. Also during these measurements the sampling frequency was 20 kHz and the filter frequency was 10 kHz, and samples were taken is a time of 60 seconds. The cross correlation between the signals from the two hot-wire probes, calculated using Equation (3.30), is given in Figure 4.9.

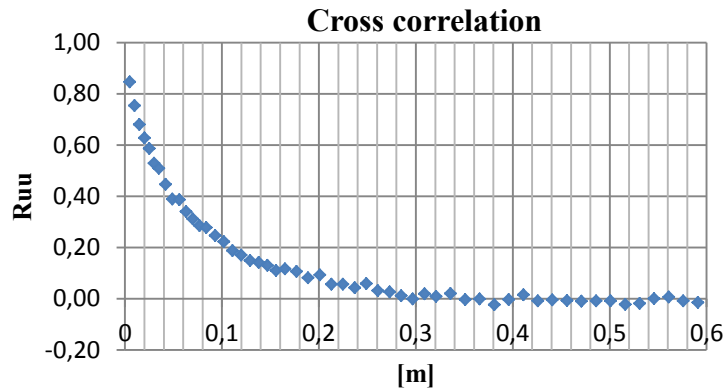


Figure 4.9: Integral length scale based on cross correlation between two hot-wire probes

By integrating the area beneath the curve given by the cross correlation, the integral length scale in z-direction, L_{uu_z} , was found to be $3.1E-2$ m. The integral length scale produced by the grid in z-direction was in other words smaller than the length scale in the streamwise direction (x-direction) found by using the von Karman specter, which is as expected.

The autocorrelation for the hot-wire probe placed in the center of the tunnel is given in Figure 4.10. This was also used to find the integral length scale in the streamwise direction in addition to the use of the von Karman specter.

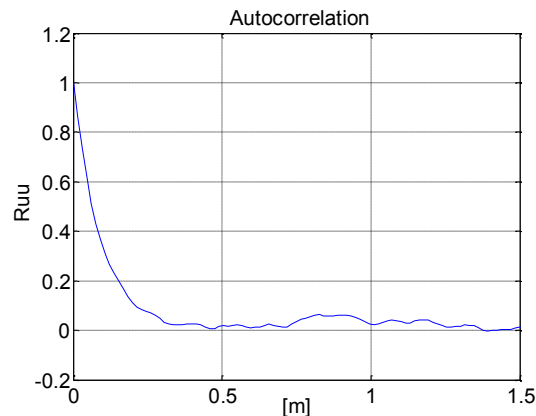


Figure 4.10: Autocorrelation of hot-wire signal in the center of the wind tunnel

Integrating the area beneath the curve, the integral length scale in the streamwise direction was found to be $L_{uu_x} = 6.5E-2$ m, which is $5.5E-2$ m lower than the integral length scale found by using the von Karman specter.

The relationship between the two integral length scales, L_{uu_x} and L_{uu_z} , found by using auto- and cross correlation corresponds to the theory. The ratio between L_{uu_x} and L_{uu_z} is 2.1 which is close to the theory stating the ratio should be 2. The fact that the integral length scale produced by the grid is at least 15 times smaller than the one expected for a full scale wind turbine, result in that a smaller part of the model wind turbine will be affected by the vortices compared to the full-scale turbine. Hence, the turbulence generated in the wind tunnel will probably have a weaker effect on the performance and wake development of the model wind turbine compared to a full scale turbine placed in an atmospheric boundary layer.

As mentioned in the introduction, S. Aubrun et al. found that the content of the turbulent eddies responsible for the meandering is more pronounced in wind tunnel experiments than in field experiments. Thus, the fact that the integral length scale produced by the grid is smaller than the one expected in atmospheric conditions might give a more realistic incoming flow.

4.4.4. Performance measurements of the model wind turbine

The performance of the wind turbine, with and without grid generated turbulence, was measured to find the tip speed ratio where the grid turbulence gave the greatest deviation in the performance of the turbine. At this point it is thought that the turbulence affects the wake the most, as the performance of the wind turbine affects the behavior of the wake. The rotational speed of the turbine was varied to obtain the different tip speed ratios, while the free stream velocity was kept constant. The conditions during the experiment are given in Table 4.4.

Table 4.4: Mean values during measurements of the performance of the model turbine

Mean values	
Free stream velocity, Without grid [m/s]	10.7
Free stream velocity, With grid [m/s]	10.4
Patm [Pa]	101405.7
Re [-]	3.95E+06
ρ [kg/m ³]	1.18
Temperature [°C]	25.8

The initial measurements conducted to find the relationship between the velocity calculated based on the contraction of the wind tunnel versus the one measured at $x = 3.75$ m downstream the grid with a Pitot probe, as described in Section 4.3.2, gave the relationships $U_{x=3.75} = U_{\text{contraction}}/0.99$ without the grid, and $U_{x=3.75} = U_{\text{contraction}}/1.15$ with the grid installed. The velocities in Table 4.4 are corrected with these relationships, and are the once used in the calculations of the power and thrust coefficients.

The acquiring voltage for thrust, torque, temperature, pressure difference and RPM were logged in LabView using a frequency of 100 Hz and a sampling time of 60 seconds, resulting in a total number of 6000 samples for each tip speed ratio from 1 to 12. Both mean values and standard deviation values were collected during the measurements. The power and thrust coefficients were calculated using Equations (3.2) and (3.3). The results are shown in Figure 4.11 and Figure 4.12 respectively.

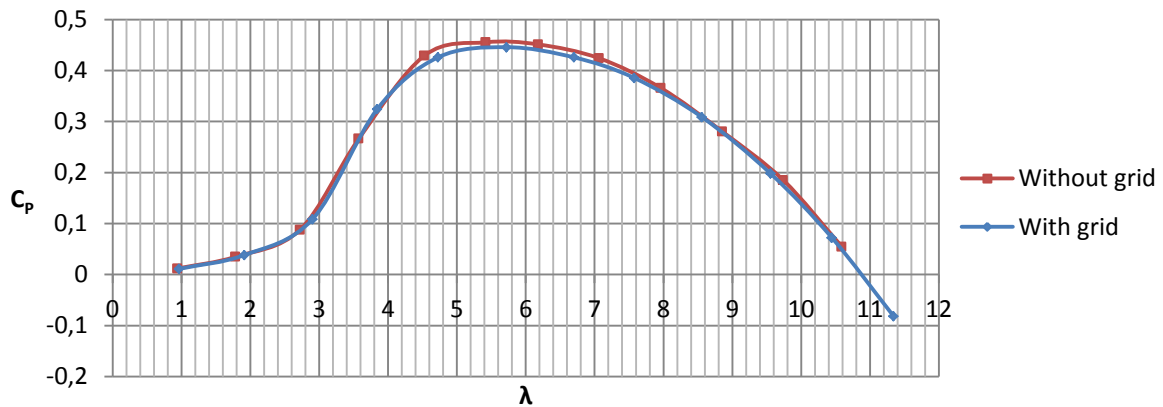


Figure 4.11: Power coefficient curve, with and without grid turbulence, TSR 1-12

Figure 4.11 show that the greatest deviation between the performance curves is in the area on the top of the power curve. Based on these results, tip speed ratio 6 was chosen as the tip speed ratio to conduct the rest of the experiments. The calculated maximum power coefficient was 0.455 at tip speed ratio 5.42 without grid generated turbulence, and 0.446 at tip speed ratio 5.72 with grid turbulence. In other words, the grid turbulence slightly decreased the efficiency of the turbine, with approximately 2.4 %.

The reason for the deviation between the C_p curves is likely due to that the flow conditions over the wind turbine blades is altered, resulting in a lower lift force and increased drag force on the turbine blades. At the top of the power coefficient curve the flow over the turbine blades is most crucial. As mentioned in the theory, the blades of a wind turbine are often designed for specific tip speed ratio. At this TSR the flow over the blade is equally distributed, giving an almost constant spanwise angle of attack and a maximum lift-to-drag ratio. When the TSR is increased or decreased, part of the blade will eventually become stalled (the airflow separates from the blade) and the lift force acting on this section of the blade is lost. Thus, it was as expected that the deviation between the curves would be greatest round the designed tip speed ratio 5.

The turbulent incoming flow will also make the flow in the boundary layer surrounding the turbine blades go from a laminar flow to a turbulent flow at a faster rate. This will increase the boundary layer thickness and hence the drag force action of the blade, which again will decrease the power extraction of the turbine. It can also be shown that a turbulent flow will increase the relative velocity of the blades, and thus increase the power extraction. When considering the power coefficient curves, it seems that the increased drag has affected the power extraction the most.

An uncertainty calculation was conducted on the power coefficients. This gave an uncertainty of ± 1.0 % without grid and ± 0.9 % with grid, with confidence interval of 95 %, for the selected tip speed ratio. The method for the analysis is given in Appendix A.3.

Figure 4.12 show the calculated thrust coefficients for the turbine with and without grid turbulence. To account for the thrust force acting on the tower, the calculated thrust coefficient was reduced with $4.1E-3$. This value is based on earlier experiments conducted on the model wind turbine [32].

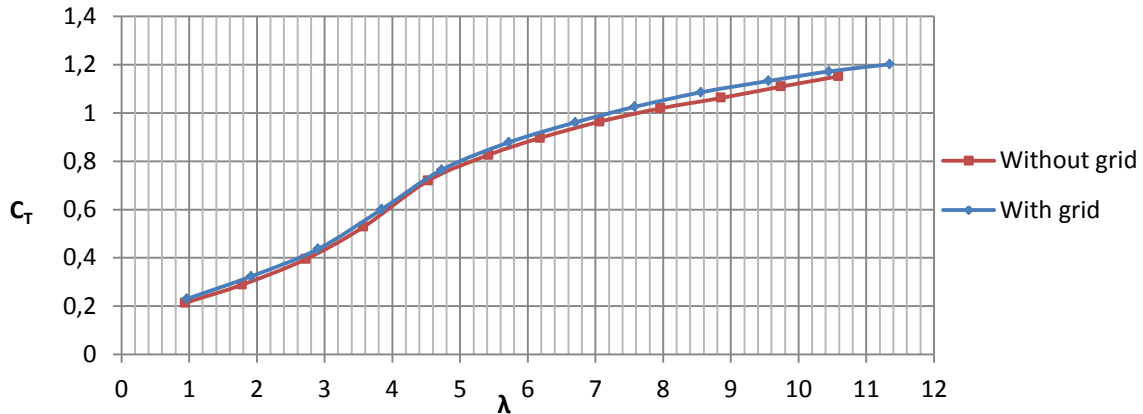


Figure 4.12: Thrust coefficient curve, with and without grid turbulence, TSR 1-12

The figure shows that the thrust force acting on the turbine is increased when the grid is installed in the wind tunnel. This is an effect of the turbulence in the free stream caused by the grid. The instability in the flow results in a greater load on the turbine. The thrust coefficient at the tip speed ratio giving the highest power coefficient without grid turbulence was calculated to 0.86 and 0.66 with grid turbulence.

The increased thrust force is mainly due to increased drag on the turbine, which will decrease the velocity in the wake of the turbine. This corresponds to the slightly decreased power coefficient when the turbine was placed in an incoming flow with turbulence intensity typical for atmospheric turbulence.

As mentioned, Medici and Alfredsson conducted an experiment where they compared the thrust force on a model wind turbine and the meandering of the wake [4]. When comparing the thrust coefficient obtained during these measurements with their results from the experiment, the thrust on the turbine should be high enough to create meandering of the wake.

4.4.5. Measurements in the wake of the model wind turbine

During this thesis there have been conducted numerous measurements in the wake of the turbine leading up to the final measurements. In this section the results from the initial measurements will be presented. The dominations of the directions used when presenting the results are illustrated in Figure 4.13. It also illustrates the experimental setup in the wind tunnel used during the measurements.

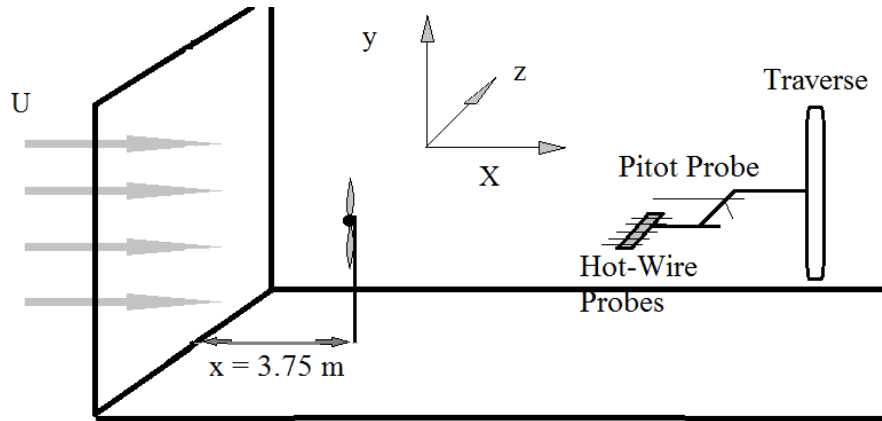


Figure 4.13: Denomination of the directions according to the model wind turbine

4.4.5.1. Locating the tip vortices

In order to find the right spacing of the hot-wire probes for detecting any meandering of the wake, measurements were conducted to find the location and width of the turbulent peaks downstream the wind turbine. The model turbine was placed at $x = 3.75$ m downstream the inlet of the test section, and measurements using only one hot-wire probe was conducted at $X/D = 1$ (D is the rotor diameter) and $X/D = 5$ downstream the turbine rotor, with and without the grid installed in the wind tunnel.

The conditions during the measurements are given in Table 4.5.

Table 4.5: Mean values during measurements locating the tip vortices

Mean values	
Free stream velocity [m/s]	10.7
Patm [Pa]	101405.7
Re [-]	4.20E+06
ρ [kg/m ³]	1.19
Temperature [°C]	22.8

The signals from the thrust and torque gauge, hot-wire probe, contraction and Pitot probe were logged at a sampling frequency of 13 kHz in 60 seconds, giving a total of 780 000 samples at each measurement point. It was used a filter of 6.5 kHz, satisfying the Nyquist theorem.

The tip speed ratio of the turbine was set to 6, based on the results given in Section 4.4.4. Using the traverse, the hot-wire probe was traversed with an increment of $2.0E-2$ m, from 0.27 m to 0.63 m from the rotor center. Measurements were taken on both sides of the turbine. Figure 4.14, Figure 4.15, Figure 4.16 and Figure 4.17 show the results from the measurements given as the turbulent kinetic energy at each measurement point. The turbulent kinetic energy is calculated based on the normal stress obtained from the program *hwconv* and Equation (3.29). In all the figures the red line represents the measurements with grid generated turbulence, and the blue without grid generated turbulence. The distance to the rotor center given in the figures is normalized by the radius of the model wind turbine, $R = 0.45$ m. The sides are named according to when facing the grid.

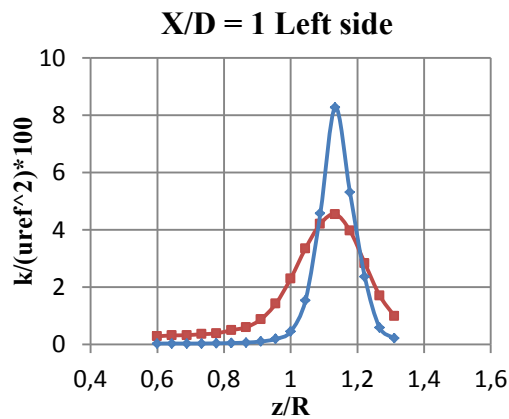


Figure 4.14: $X/D = 1$, turbulent kinetic energy with (red line) and without (blue line) grid turbulence, left side

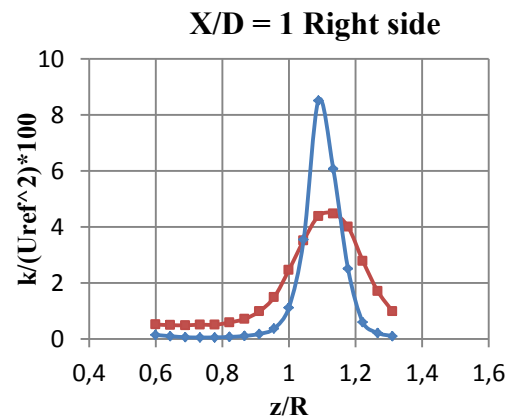


Figure 4.15: $X/D = 1$, turbulent kinetic energy with (red line) and without (blue line) grid turbulence, right side

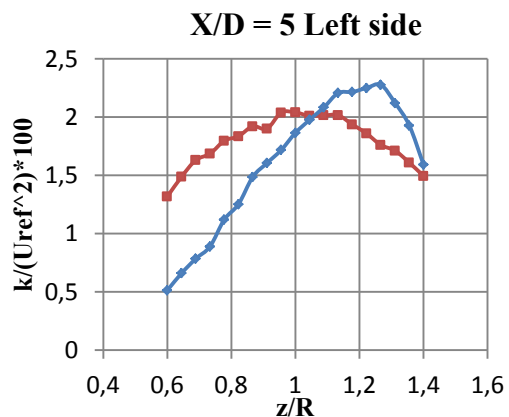


Figure 4.16: $X/D = 5$, turbulent kinetic energy with (red line) and without (blue line) grid turbulence, left side

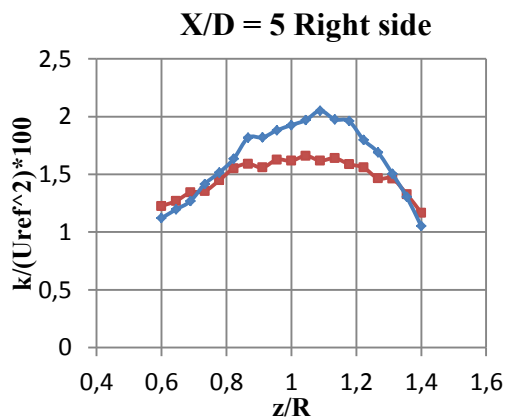


Figure 4.17: $X/D = 5$, turbulent kinetic energy with (red line) and without (blue line) grid turbulence, right side

At $X/D = 1$ downstream the turbine, the effect of installing a grid in the wind tunnel is clear. The peak in the turbulent kinetic energy is much wider with an incoming flow with turbulence intensity round 5.5 %, and the maximum value of the turbulent kinetic energy is decreased with a factor a bit under two compared to the case with an incoming flow with low turbulence intensity. However, the area beneath the curves seems to be in the same order.

This indicates that the energy in the flow is smeared out due to the incoming flow with turbulence intensity typical for atmospheric turbulence. This is as expected when considering the theory given in Chapter 3.

At $X/D = 5$ downstream the turbine, the peaks in the energy are not that obvious. Both measurements, with and without grid generated turbulence, give a wide profile with a much lower value of the turbulent kinetic energy compared to $X/D = 1$. This can be an indication that the tip vortices have merged together/broken up. However, at the right side of the turbine at $X/D = 5$, the turbulent kinetic energy is decreased when the grid is installed. This might indicate that the tip vortices are not fully broken up at $X/D = 5$ without grid turbulence, since it is some congestion of the energy in the wake. In general, the energy in the wake has been smeared out over much wider area.

Based on these results, the tip vortices seems to be located between $z/R = 0.95$ to $z/R = 1.27$ at $X/D = 1$ without the grid, and $z/R = 0.90$ to $z/R = 1.30$ with grid generated turbulence. At $X/D = 5$ one might guess that the tip vortices is located a bit farther from the rotor center, if they exists, due to the expansion of the wake downstream the turbine. The small peak in the turbulent kinetic energy at the left side at $X/D = 5$ may be an indication that if the tip vortices still exist, they exists in an area between $z/R = 1.10$ to $z/R = 1.35$. However, the turbulent kinetic energy is not symmetric as seen in the figures.

Previous measurements have also shown an unsymmetrical behavior in the wake of the model wind turbine. This it is believed to be caused by either the tower of the turbine and/or a banner that the placed on one of the sidewalls in the wind tunnel (on the right side when facing the grid).

4.4.5.2. Measurements with hot-wire array

The main measurements in the wake, which is used to study the wake meandering, were conducted using 5 hot-wire probes attached to a rake. The distance between the probes was decided based on the results when locating the tip vortices behind the turbine, given in the previous section. Since the diameter of the tip vortices were a bit uncertain, a gradually increasing distance between the probes was chosen in hope of detecting all three tip vortices with at least two probes at the same time and to cover the area where the tip vortices might meander. The measurements was to be cross correlated at a later stage to see how the well the occurrences in the flow field were related.

The minimum distance was set to $1.60E-2$ m and a maximum distance of 0.25 m. A sketch of the rake is given in Figure 4.18. Hot-wire probe 1 was placed closest to the rotor center. The distance between the probes was measured with a micrometer.

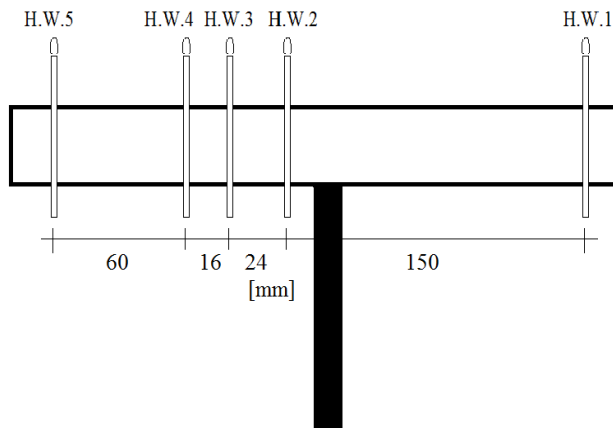


Figure 4.18: Rake 1, with distance between hot-wire probes

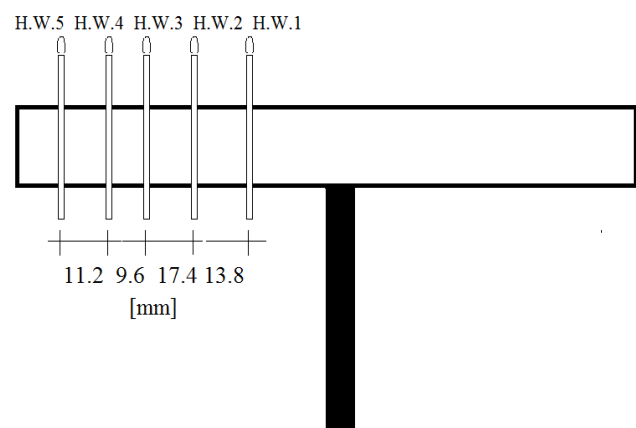


Figure 4.19: Rake 2, with distance between hot-wire probes

The rake was attached to the traverse in the wind tunnel together with the Pitot probe, which made it possible to move the hot-wire probes and the Pitot probe in all three directions during measurements. The measurements were carried out at $X/D = 1, 3,$ and 5 downstream the wind turbine rotor at rotor height, and samples were taken in an area of $z/R=0.45$ to $z/R=1.70$ in the horizontal direction relative to the wind tunnel floor, with an increment of $2.0E-2$ m.

The tip speed ratio of the model wind turbine was set to 6. The acquiring voltage from the hot-wire probes was logged at a frequency of 20 kHz at a sampling time of 60 seconds, giving a total of $1.2E+6$ samples per hot-wire probe. The signal was filtered at 10 kHz. A ramp generator was used to signal every rotation of the turbine. This signal was logged simultaneously as the acquiring voltage from the hot-wire anemometers and stored in the same time series. This makes it possible to pick out data from only one rotation of the turbine at a later stage. The acquiring voltage from the Pitot probe, contraction and the temperature during the measurements were sampled at the same sampling frequency and stored as mean values for each measurement point.

The conditions during the measurements are given in Table 4.6.

Table 4.6: Mean values during measurements with hot-wire array

Mean values	
Free stream velocity [m/s]	11.0
Patm [Pa]	101400.6
Re [-]	4.23E+06
ρ [kg/m ³]	1.19
Temperature [°C]	22.2

During the experiments one of the hot-wire probes broke, resulting in that the minimum distance between two probes was $2.4E-2$ m when conducting the experiment. In Figure 4.20, the normal stress, $u'u'$, from the four remaining probes are plotted.

The z positions of the probes are given in Table 4.7. Based on the measurements locating the tip vortices, these locations should cover the area in the wake where the tip vortices are located.

Table 4.7: Position of hot-wire probes

	HW 1	HW 2	HW 3	HW 5
Distance from rotor center [m]	0.640	0.490	0.466	0.390
z/R	1.4	1.1	1.0	0.9

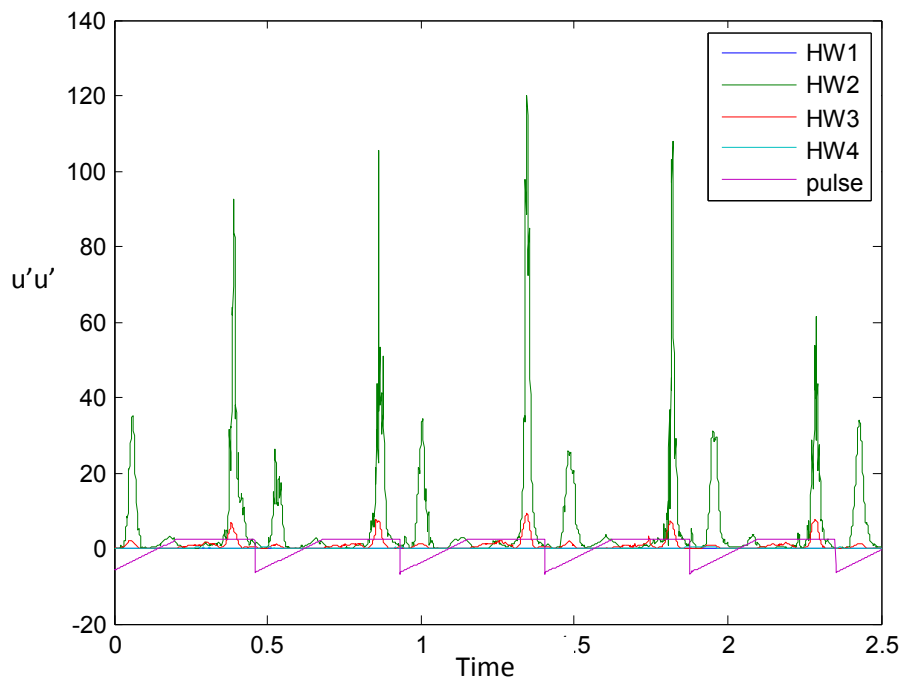


Figure 4.20: Results from first multiple hot-wire probes measurements

The figure shows the four hot-wire signals as well as the pulse signal measured at $X/D = 1$ downstream the turbine without grid generated turbulence in the wind tunnel. Each drop in the pulse signal indicates a new rotation of the turbine. In other words, the figure shows 5 whole rotations of the turbine.

As seen from the figure, none of the hot-wire probes detected all three tip vortices in one rotation, which would have been represented as three distinct peaks in the normal stress within one rotation. In this figure there is only sign of two tip vortices in the flow, which indicate that the tip vortices is not equally shed from the wind turbine blades. It is likely to believe that one of the tip vortices is located between two of the hot-wire probes, and thus is not detected with the rake.

From the results it appeared like the diameter of the tip vortices are smaller than first assumed. After studying previous measurements conducted in the wake of the turbine, the diameter was thought to be in the area of $1.8E-2$ m to $2.2E-2$ m [33].

Based on this it was decided to conduct a new experiment with a narrower distance between the probes. A sketch of the new rake, with the new distances between the probes, is given in Figure 4.19.

4.4.5.3. Second experiment with hot-wire array

Also in the second experiment were the measurements carried out at $X/D = 1, 3,$ and 5 downstream the turbine at rotor height. Samples were taken in an area of $z/R=0.67$ to $z/R=1.64$ at $X/D = 1,$ of $z/R=0.44$ to $z/R=1.64$ at $X/D = 3,$ of $z/R=0.43$ to $z/R=1.71$ at $X/D = 5$ in the horizontal direction relative to the wind tunnel floor. In this experiment the increment between the measurement points was increased to $3.5E-2$ m between each measurement due to the narrow distance between the probes. It was used the same sampling frequency and setup as the in fist experiment conducted with rake number 1. The measurements were only executed on the left side in the wake of the turbine when facing the inlet to the test section in the wind tunnel.

Figure 4.21 shows a picture of the setup of the hot-wire rake, with the five hot-wire probes and the Pitot probe attached to a bar on the traverse, used during the measurements in the wake of the model wind turbine.

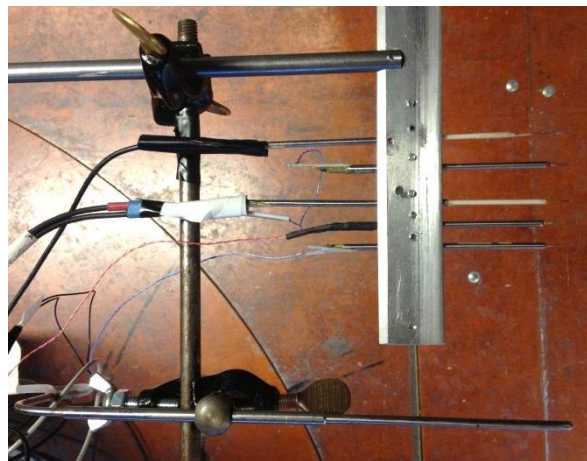


Figure 4.21: Picture of hot-wire rake 2 and Pitot probe setup

In the experiment without the grid installed in the wind tunnel, the rotational speed of the model wind turbine varied round 1300 rpm. This provides a number of round 940 samples per rotation using a sampling frequency of 20 kHz. When conducting the measurements with the grid installed, the turbine was set to a rotational speed of round 1500 rpm, which gives a number of round 810 samples per rotation when using the same sampling frequency.

The fact that there was a difference between the rotational speed of the wind turbine during the two experiments was not intended, and was discovered at a late stage in the master thesis. The calculated tip speed ratio based on the conditions during the two measurements gave a tip speed ratio of 6 during the measurements without the grid installed and close to 7 for the measurements with the grid turbulence.

To estimate the error, or the influence this will have on the results, the spanwise angle of attack over the turbine blade was calculated for the two scenarios. The calculations showed a decrease of round 40 % in the spanwise angle of attack at the root of the blade, while for the tip of the blade, the decrease was round 15 %. This means that the change in the tip speed ratio will increase the loads on the root of the blade more than on the tip of the blade. Thus, the increased tip speed ratio will not affect the tip vortices as much. The velocity in the wake will decrease, as the drag force increase at the root, which can result in a more rapidly expanding wake. The lift force acting on the turbine blade will also decrease, which might affect the strength of the tip vortices, as seen from Equation (3.40). However, the increased tip speed ratio is hopefully not that great that the flow field in the wake will be significantly altered between the two cases.

The angle of which the tip vortices travel downstream in the wake in the two cases can be calculated by using the velocity triangle. A sketch is given in Figure 4.22.

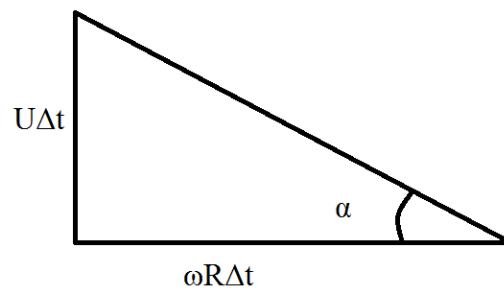


Figure 4.22: Velocity triangle

Using the free stream velocity during the measurements without grid generated turbulence, U_{ref} , the radius of the turbine, R , the rotational speed, ω , and the time Δt , the angle was calculated to 9.45° . This is the same angle as obtained when taking the inverse of the tip speed ratio;

$$\frac{1}{\lambda} = 9.46^\circ$$

Calculating the angle of which the wake expands with the tip speed ratio used during the measurements with grid turbulence, $\lambda=7$, gives $\alpha=8.13^\circ$. The wake will in other words expand with a narrower angle in this case.

The conditions during the second measurements conducted with an hot-wire array are given in Table 4.8. The turbine was placed $x = 3.75$ m behind the inlet to the test section, giving a turbulence intensity of round 5.5 % in the incoming flow when the grid was installed. The integral length scales at this position were, as found previously, $L_{uux} = 6.5E-2$ m and $L_{uuz} = 3.1E-2$ m. The incoming freestream without grid generated turbulence has previously been measured to be uniform within ± 1 % measured over the area swept by the rotor, and the turbulence intensity to 0.3 % [34].

Table 4.8: Mean values during second measurements with hot-wire array

Mean values	
Free stream velocity, both with and without grid [m/s]	10.2
Patm [Pa]	100542
Re [-]	3.54E+06
ρ [kg/m³]	1.173
Temperature [°C]	27.3

At a rather late state in the master thesis, when analyzing the results, it was revealed that hot-wire probe number four gave incorrect values. The measurements conducted with hot-wire four is therefore excluded in the analysis of the measurements.

The results from the second measurements will be presented and discussed in Chapter 5.

5. Main results and discussion

In this chapter the results from the measurements conducted both with and without grid generated turbulence with rake number two will be presented. The results of the measurements for both cases will be presented side by side in order to see the effect of the grid turbulence more clearly. In the end of the chapter there will be a short summary and final discussion of the results seen in this chapter.

The time series chosen in the first part of this chapter are chosen on the basis of the initial measurements indicating the location of the tip vortices in the wake.

5.1. Time series $X/D = 1$

The values presented in this section all represents five rotations of the model wind turbine.

Figure 5.1 (a) and (b) and Figure 5.2 (a) and (b) shows the normal stress, $u'u'$, for five rotations of the wind turbine rotor, measured at $X/D = 1$ downstream the turbine with and without grid turbulence. The drops in the pulse signal in Figure 5.1 (a) and (b) indicate the start of a new rotation of the turbine. The location of the probes in z direction is given in Table 5.1.

Table 5.1: $X/D = 1$, Position 1 of hot-wire probes

	HW 1	HW 2	HW 3	HW 5
Distance from rotor center [m]	0.475	0.4888	0.5056	0.5264
z/R	1.056	1.086	1.124	1.170

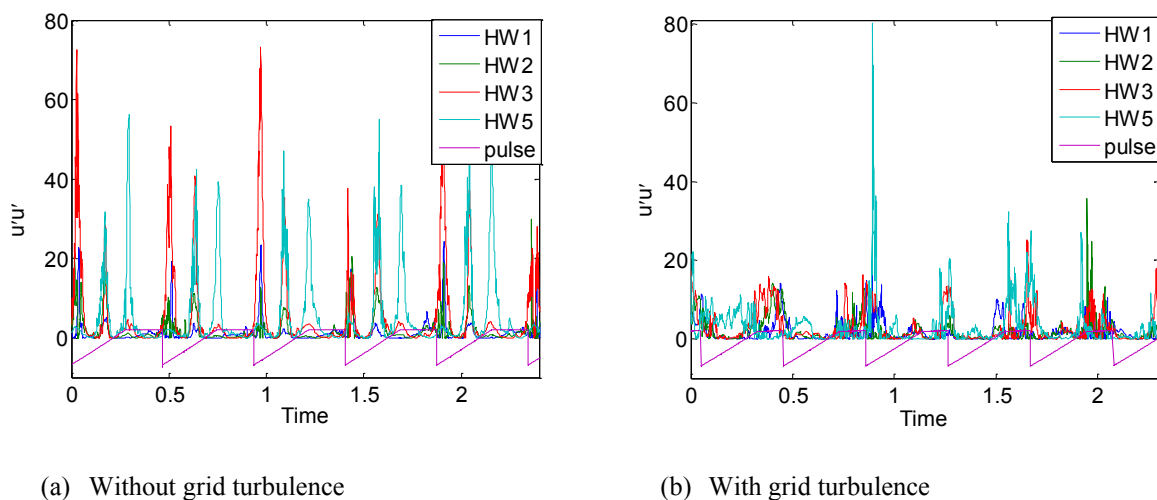


Figure 5.1: $X/D = 1$, Position 1 (a) Five rotations without grid turbulence, (b) Five rotations with grid turbulence

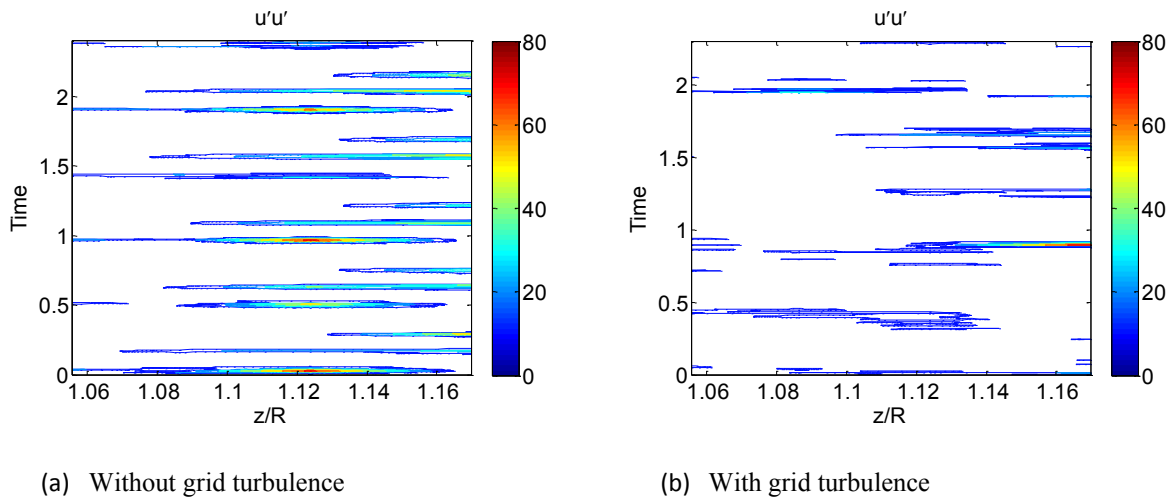


Figure 5.2: $X/D = 1$, Position 1, Contour plot (a) Five rotations without grid turbulence, (b) Five rotations with grid turbulence

In Figure 5.1(a) the presence of the three tip vortices within each rotation is quite clear compared to Figure 4.16, which represented the measurements conducted with the rake number one. However, the amplitudes of the normal stress and the distance between them are a bit varying. This might indicate the loads on the rotor blades are unequal, and thus be the cause to why only two of the tip vortices were detected in the first experiment. If this is the case, it will cause the tip vortices to be shed in different courses out from the tip of the blade (clarified in a later section). The unequal loads can for instance be a consequence of deformation/damages on the rotor blades and/or different pitch angle on the turbine blades.

When comparing Figure 5.1 (a) and (b), it is quite clear that the turbulence has affected the wake of the turbine, even though the integral length scale was smaller than desired in order to satisfy the downscaled atmospheric conditions, though the turbulence intensity is at a correct level. There are no longer clear peaks indicating the presence of the tip vortices, and no evident structure within the rotations. In general, the amplitudes of normal stress are decreased when the turbine is placed in the turbulent incoming flow. However, there is one peak that stands out which has the same amplitude as the measurements conducted without turbulence. One of the effects of the decreased amplitudes of normal stress is a normal stress that is more spread out over the range of z/R given by these time series. This can be seen as the noisier signal in Figure 5.1 (b).

Figure 5.2 (a) and (b) visualizes the peaks in the normal stress as a function of the distance to the rotor center, z/R . The figures represent the same measurement points and the same five rotations as in Figure 5.1 (a) and (b). The division into the five rotations can be done by comparing the time at which the pulse signal drops in Figure 5.1 (a) and (b), with the time given in Figure 5.2 (a) and (b). (Each rotation is a bit under 0.5 in the time scale).

In Figure 5.2 (a) the three tip vortices within each rotation is quite clear, represented by the accumulated normal stress. The figure also shows a repeating pattern within each rotation. However, the tip vortices seem to be shifted a bit to the right. This coincides with the different loads on the blades mentioned earlier.

Figure 5.3 illustrates how different loads on the rotor blades can cause the tip vortices to be shed in different direction, and thus, be the reason for the tip vortices to be shifted to the right in Figure 5.2 (a).

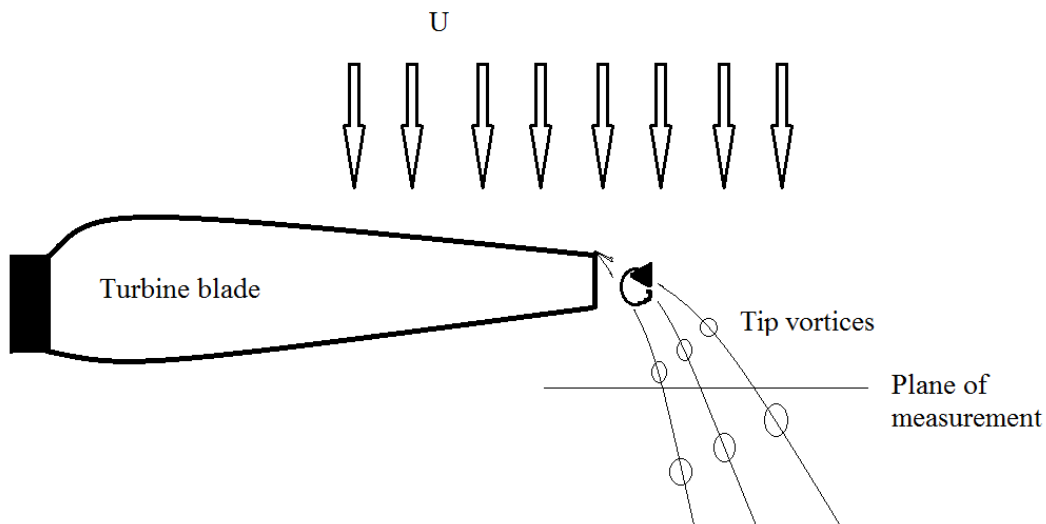


Figure 5.3: Tip vortex shedding

As mentioned in the Chapter 3, the tip vortices might follow their own path with unequal transport velocities if the pitch angle of the turbine blades is unequal. Since the fine setting of the pitch angle on the turbine blades was done with a protractor, it might be some uncertainty related to this angle. This might be the reason for the tip vortices to be shed unequal.

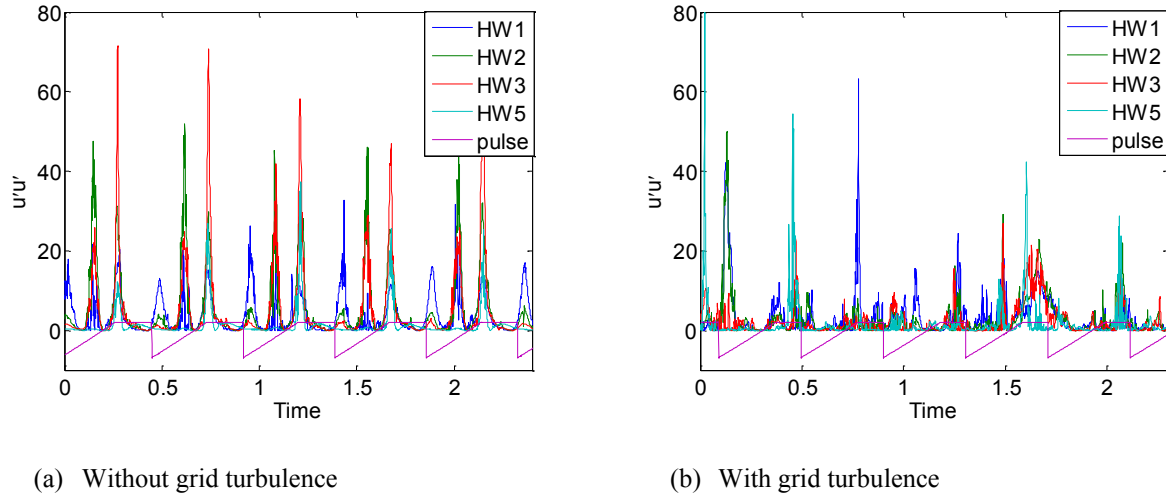
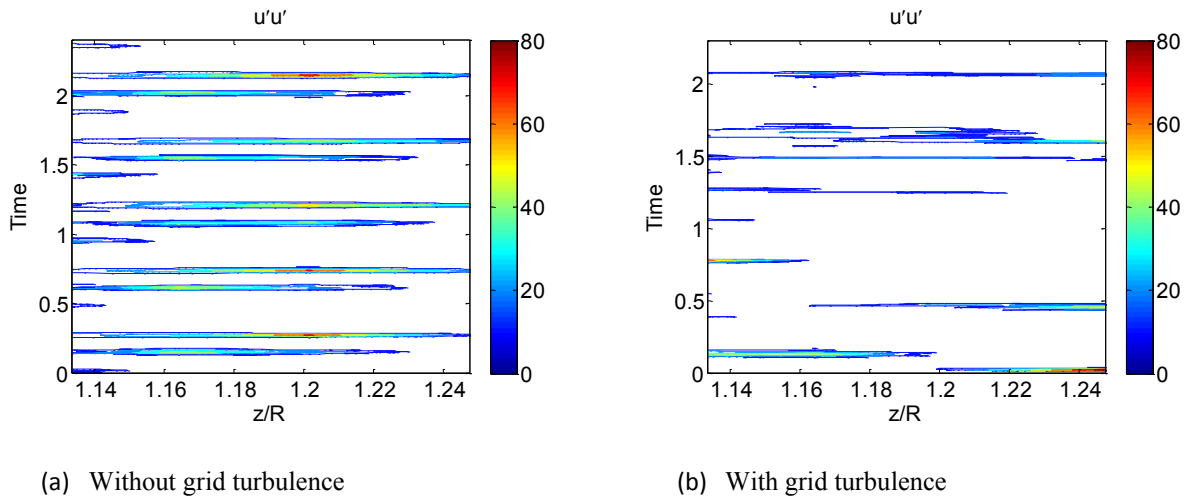
One of the tip vortices in Figure 5.2 (a) seems to be located round $z/R = 1.12$ in each rotation. The center of the vortex is located between $z/R = 1.10$ to $z/R = 1.14$, which is a distance of $1.80E-2$ m. The tip vortex center is defined as where the normal stress is higher than the mean value of the normal stress, which in other words is when the normal stress has a value over 40 in Figure 5.2 (a). This indicates that the size of the tip vortex is smaller than expected and as first assumed when conducting the measurements with rake 1. The center of the other two vortices is not that evident in this figure, and thus the sizes of them difficult to state.

Figure 5.2 (b) illustrate what was seen in the plot representing the normal stress with grid turbulence in Figure 5.1 (b). There is no evident repeating pattern between the rotations, which makes it difficult to state if there are three single tip vortices present in the wake, or if they already have merged together.

When keeping in mind that the wake might expand faster in an incoming flow with higher turbulence intensity, the same plot, but at a location further from the center of the rotor is given in Figure 5.4 (a) and (b). The positions of the probes are given in Table 5.2.

Table 5.2: $X/D = 1$, Position 2 of hot-wire probes

	HW 1	HW 2	HW 3	HW 5
Distance from rotor center [m]	0.510	0.5238	0.5406	0.5614
z/R	1.133	1.164	1.201	1.248

Figure 5.4: $X/D = 1$, Position 2 (a) Five rotations without grid turbulence, (b) Five rotations with grid turbulenceFigure 5.5: $X/D = 1$, Contour plot, Position 2 (a) Five rotations without grid turbulence, (b) Five rotations with grid turbulence

In Figure 5.4 (a) the presence of the three tip vortices are still quite evident in the case when the turbine is placed in a flow with low turbulence intensity. However, one of the tip vortices seems to be a bit weaker at this location, and the amplitudes of the normal stress vary a bit more when comparing the different rotations. In the measurements with grid generated turbulence, given in Figure 5.4 (b), it seems that it might be a bit more systematic behavior within the rotations compared to the location closer to the rotor center.

There are more evident peaks in the normal stress, which might indicate the presence of tip vortices. However, it is difficult to state if the peaks represent one or more tip vortices. The amplitudes of the normal stress have in general increased compared to the previous location of the probes, indicating that more of the energy in the wake is located in this z/R range.

In Figure 5.5 (a) and (b) the location of the peaks in the normal stress are given as a function of the distance to the rotor center by z/R . Figure 5.5 (a) clearly illustrates a repeating pattern within the rotations, the same as seen in the contour plot in Figure 5.2 (a). However, there are now two evident tip vortices which have their center in this range of z/R . The peaks in the normal stress are located round $z/R = 1.17$ and $z/R = 1.20$. The tip vortex to the left in the figure is located between $z/R = 1.15$ and $z/R = 1.18$, which is a distance of $1.35E-2$ m, and the tip vortex to the right is located between $z/R = 1.18$ and $z/R = 1.22$, giving a distance of $1.80E-2$ m. In other words, the two tip vortices seen in this figure seem to be of same different size.

As seen previously, the tip vortices are a bit shifted from one another. To the left in the contour plot in Figure 5.5 (a), it seems to be a small indication of the first tip vortex which was found in the previous section when presenting the measurements conducted at position 1 of the rake.

As seen in Figure 5.5 (b), there is still no clear indication of any repeating pattern in the wake when the turbine is placed in a turbulent incoming flow. However, there are some peaks in the normal stress. As seen in the z/R range given previously, the energy is more smeared out over the entire range. This corresponds to the measurements described in Section 4.4.5.1 when locating the tip vortices.

The normal stress for an even further position from the rotor center, represented in Table 5.3, is given in Figure 5.6 (a) and (b) and Figure 5.7 (a) and (b).

Table 5.3: $X/D = 1$, Position 3 of hot-wire probes

	HW 1	HW 2	HW 3	HW 5
Distance from rotor center [m]	0.5450	0.5588	0.5756	0.5964
z/R	1.211	1.242	1.279	1.325

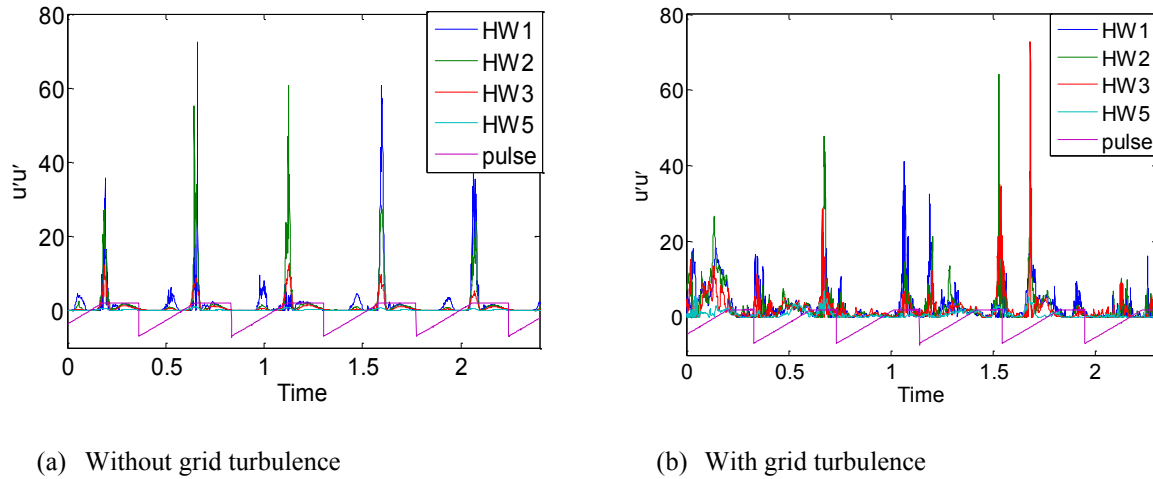


Figure 5.6: $X/D = 1$, Position 3, (a) Five rotations without grid turbulence, (b) Five rotations with grid turbulence

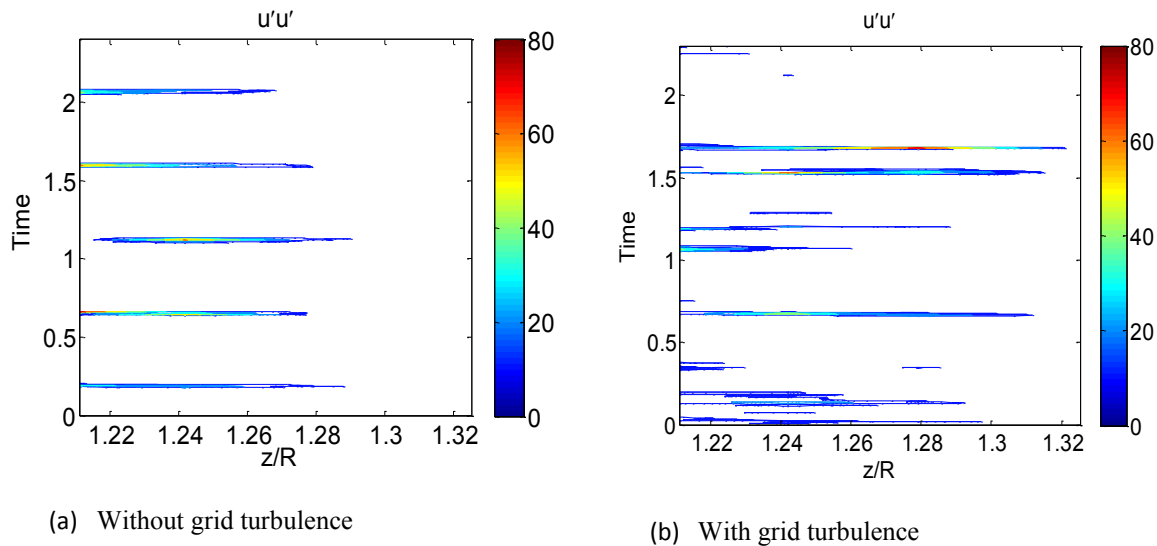


Figure 5.7: $X/D = 1$, Contour plot, Position 3 (a) Five rotations without grid turbulence, (b) Five rotations with grid turbulence

There are still some evident peaks in the normal stress both with and without grid generated turbulence. However, in the measurement with low turbulence intensity, represented in Figure 5.6 (a), it seems that the normal stress representing only one of the tip vortices is picked up by the hot-wire probes. There are some small indications of a second one, but its amplitude is quite small compared to the other one. Hot-wire probe five seems to be located outside, or at the edge of the wake. The normal stress at this location, $z/R = 1.325$, is barely visible as small peaks occurring at the passage of the one evident tip vortex in this range of z/R . This corresponds well to the results obtained when locating the tip vortices in the wake. In the case with grid generated turbulence, represented in Figure 5.6 (b), none of the signals have this kind of calm signal. Thus, the normal stress in the wake with the incoming flow with turbulence intensity round 5.5 % seems to be more spread out at this location in the wake.

Figure 5.7 (a) and (b) represents the same measurements as given in Figure 5.6 (a) and (b), but presented as a contour plot giving the position of the normal stress according to the distance to the rotor center, z/R .

In Figure 5.7 (a) the tip vortex located round $z/R = 1.20$ in the previous section is clearly seen within every rotation. The location of the peak value seems to vary a bit, from $z/R = 1.20$ to $z/R = 1.24$, which equals a distance of $1.80E-2$ m. However, it seems that the tip vortex is not fully captured at this z/R range. Later in this chapter, in Section 5.5, a phase averaging of the results will be conducted. This will give a clearer image of the locations of the tip vortices and their size based on the normal stress in the wake.

In Figure 5.7 (b), there is still no evident systematic behavior in the normal stress within the different rotations. However, the normal stress is located to the left in the figure, which is the same as in the case for the measurements conducted in a flow with low turbulence intensity.

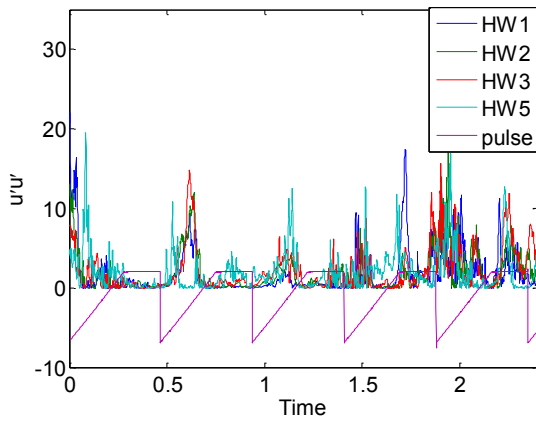
5.2. Time series $X/D = 3$

The values in this section represent five rotations of the model wind turbine.

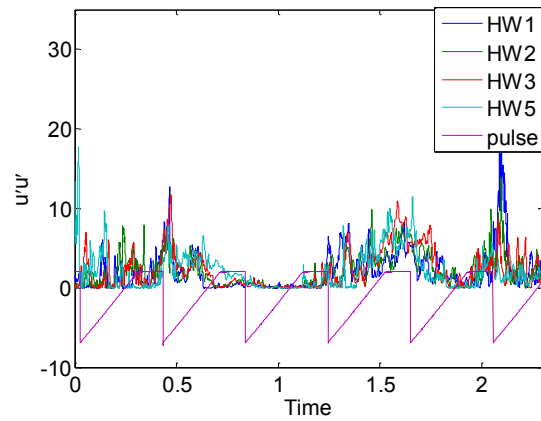
Figure 5.8 (a) and (b) and Figure 5.9 (a) and (b) represents the normal stress measured at $X/D = 3$ downstream the model wind turbine, for the cases with and without grid generated turbulence. The positions of the hot-wire probes are given in Table 5.4.

Table 5.4: $X/D = 3$, Position 1 of hot-wire probes

	HW 1	HW 2	HW 3	HW 5
Distance from rotor center [m]	0.480	0.4938	0.5106	0.5314
z/R	1.067	1.097	1.135	1.181

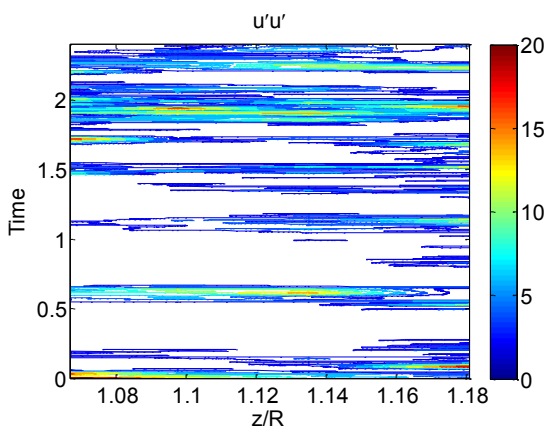


(a) Without grid turbulence

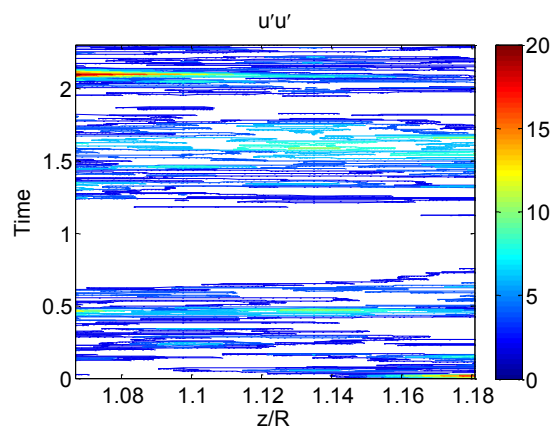


(b) With grid turbulence

Figure 5.8: $X/D = 3$, Position 1 (a) Five rotations without grid turbulence, (b) Five rotations with grid turbulence



(a) Without grid turbulence



(b) With grid turbulence

Figure 5.9: $X/D = 3$, Contour plot, Position 1 (a) Five rotations without grid turbulence, (b) Five rotations with grid turbulence

When comparing Figure 5.8 (a) and (b) with the once representing the normal stress at $X/D = 1$ downstream the turbine, the flow in the wake seems much more chaotic. In the case with an incoming flow with low turbulence intensity, presented in Figure 5.8 (a), the amplitudes of the normal stress are decreased and the clear indication of the three tip vortices is no longer present. Though, at $X/D = 3$ downstream the wind turbine rotor, the wake might have expanded and the tip vortices might be found further from the rotor center. Since the amplitude of the normal stress at $X/D = 1$ downstream the turbine without the grid generated turbulence was quite high, one might expect that the tip vortices still exist at $X/D = 3$ downstream the turbine rotor. However, the energy in the flow at this location is much more spread out in the range of the measurement.

In Figure 5.8 (b), representing the normal stress at $X/D = 3$ with an incoming flow with a turbulence intensity round 5.5 %, there seems to be no sign of anything other than chaos. The energy is spread out as seen in the noisy and chaotic signal. This is what one might expect at 3 diameters downstream the rotor when the turbine is placed in the grid generated turbulence. The turbulent flow will dissolve any systematic behavior in the wake more rapidly due to the faster decay of the turbulence and recovery of the wake deficit. Even though, the level of the normal stress is quite equal for both the cases with and without grid generated turbulence.

Figure 5.9 (a) and (b) represents the same measurement, but presented in a contour plot indicating the position of the normal stress according to the distance to the rotor center. It doesn't seem to be any systematic behavior in the wake in either of the two cases. Though in Figure 5.9 (a) the normal stress is more gathered, which might indicate that it still exist some kind of structure in the wake. Figure 5.9 (b) shows the chaotic behavior in the wake behind the turbine at this location with an incoming flow with turbulent intensity round 5.5 %. The normal stress is smeared out over the entire range given in the figure.

In Figure 5.10 (a) and (b) and Figure 5.11 (a) and (b), the probes are moved a bit further from the rotor center. The positions of the hot-wire probes are given in Table 5.5.

Table 5.5: $X/D = 3$, Position 2 of hot-wire probes

	HW 1	HW 2	HW 3	HW 5
Distance from rotor center [m]	0.5150	0.5288	0.5456	0.5664
z/R	1.144	1.175	1.212	1.259

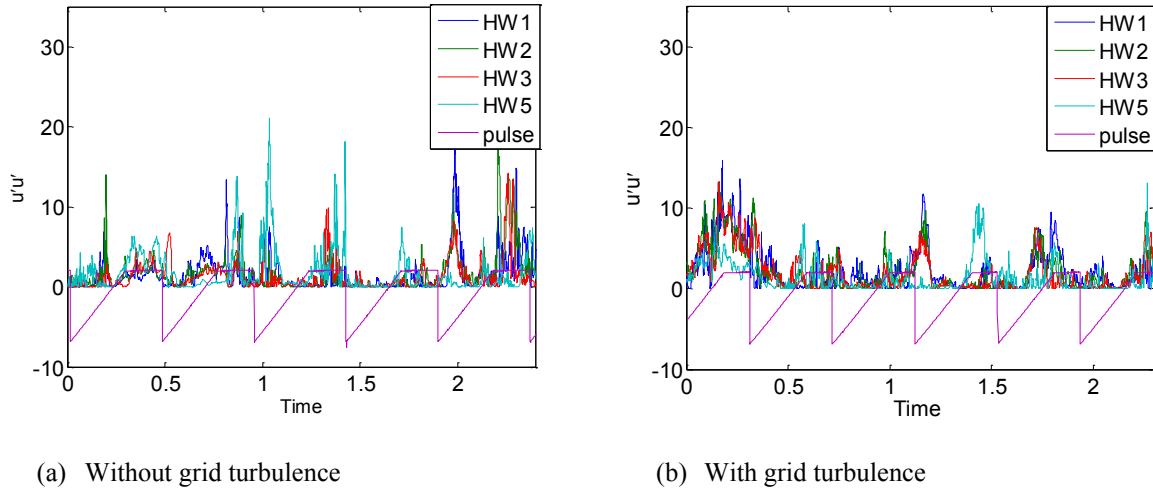


Figure 5.10: $X/D = 3$, Position 2 (a) Five rotations without grid turbulence, (b) Five rotations with grid turbulence

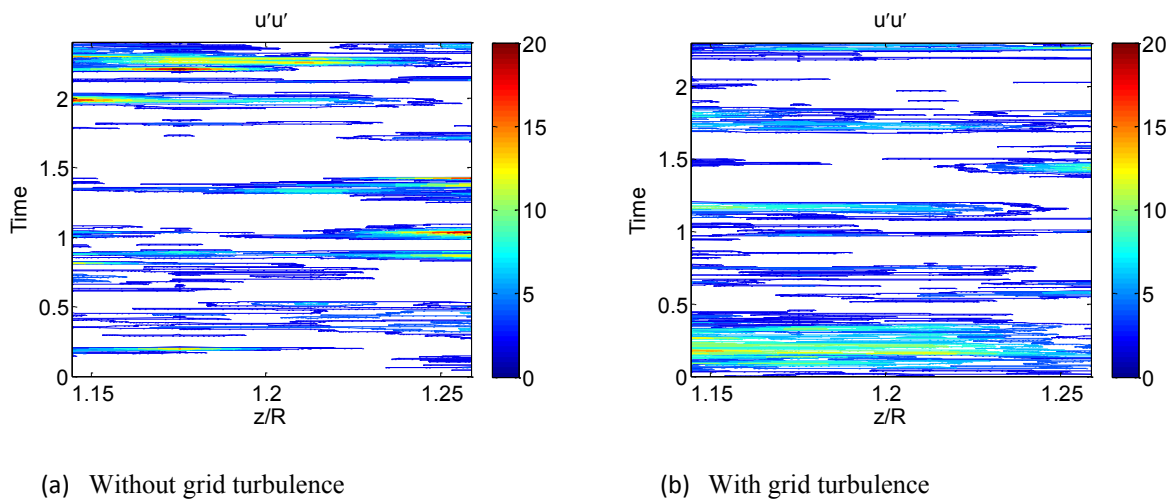


Figure 5.11: $X/D = 3$, Contour plot, Position 2 (a) Five rotations without grid turbulence, (b) Five rotations with grid turbulence

Even at this distance from the rotor center, there are no evident structures within the rotations. There are some peaks in the normal stress in the wake when the turbine is placed in a low turbulent incoming flow, as seen in Figure 5.10 (a). The level of the normal stress has in general decreased when compared to the z/R range given in the previous section, and it seems to be less “noise” in the flow. However, there are still some peaks, which might indicate that there still exists a distinct tip vortex at this distance from the turbine rotor in the wake.

In the case with grid generated turbulence, given in Figure 5.10 (b), the normal stress is quite equal as seen at the z/R range given previously; it is no repeating pattern and the level of the normal stress has not changed. The energy in flow is smeared out over the entire area.

The locations of the peaks in the normal stress according to the distance to the rotor center are illustrated in Figure 5.11 (a) and (b). Figure 5.11 (a) indicates that the location of the peaks in the normal stress varies when comparing the different rotations.

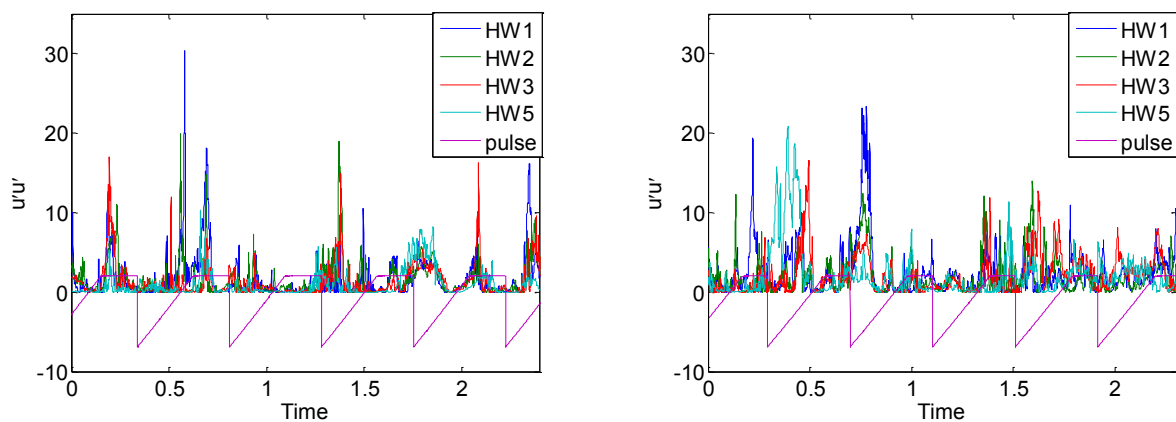
In rotation number 1 and 5 the peak is located round 1.17, in rotation 2 and 3 it is located round 1.25, while in rotation number 4 there is no evident peak in normal stress. The fact that the normal stress in rotation 4 is so weak is a bit surprising, since the energy in the flow needs to be somewhere. The change in the location of the peak values might indicate the energy moves around in the wake.

In Figure 5.11 (b) there are still no sign of any repeating pattern within the rotations. The normal stress is more spread out over entire the area at this location, and there is no indication of systematic behavior. The level of the normal stress is decreased compared to the case without grid generated turbulence. This might indicate that the energy in the wake has spread out even more due to the turbulent incoming flow.

When moving even further from the rotor center, to the positions given in Table 5.6, the level of the normal stress increase in both cases and it still exist evident peaks in the normal stress; see Figure 5.12 (a) and (b).

Table 5.6: $X/D = 3$, Position 3 of hot-wire probes

	HW 1	HW 2	HW 3	HW 5
Distance from rotor center [m]	0.5500	0.5638	0.5806	0.6014
z/R	1.222	1.253	1.290	1.336



(a) Without grid turbulence

(b) With grid turbulence

Figure 5.12: $X/D = 3$, Position 3 (a) Five rotations without grid turbulence, (b) Five rotations with grid turbulence

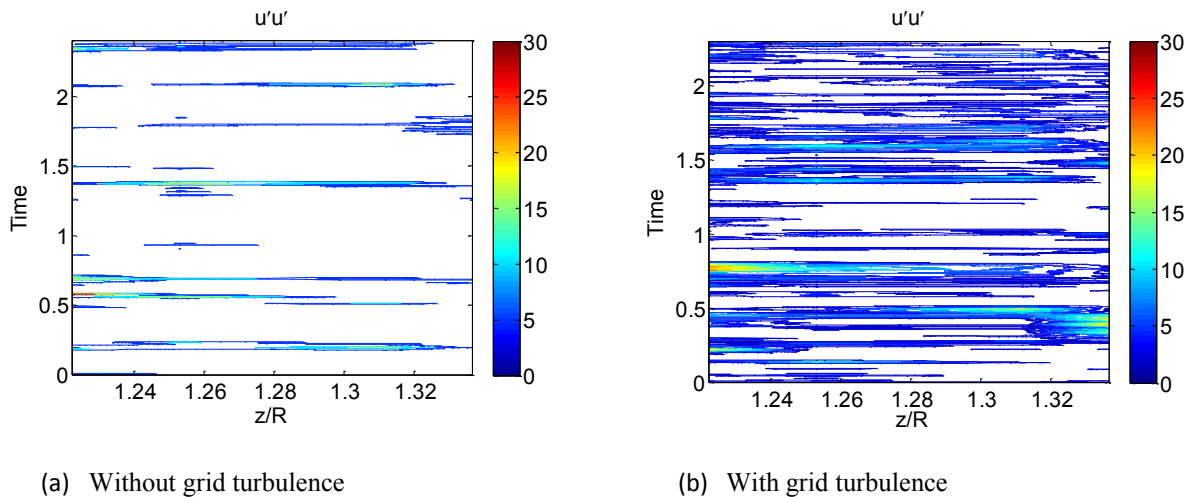


Figure 5.13: $X/D = 3$, Contour plot, Position 3 (a) Five rotations without grid turbulence, (b) Five rotations with grid turbulence

As seen when comparing Figure 5.12 (a) and (b), the amplitudes of the normal stress for the two cases are quite even, but the energy distribution in the flow for the two cases are not comparable. It is much less noise in the normal stress in the case without grid generated turbulence.

In the case with grid turbulence the flow seems more chaotic and disorganized and the energy in the flow is spread between the positions of the hot-wire probes.

The positions of the peaks in the normal stress for the two cases are given in Figure 5.13 (a) and (b). Figure 5.13 (a) indicates that the peaks are a bit spread over the z/R range given in the figure. At the other two z/R ranges given in the previous sections, the peaks tended to appear at the some of the same z/R positions for the different rotations. At this position it seems to be some congestion round $z/R = 1.3$ within each rotation. The energy in the wake at this distance from the turbine rotor is however quite gathered compared to the case with an incoming flow with turbulence intensity round 5.5 %. The normal stress in the wake behind the turbine when placed in the turbulent flow, see Figure 5.13 (b), is smeared out with no apparent structure, and the peaks seen in Figure 5.12 (b) in the first two rotations are located at different z/R positions.

Having in mind that the at $X/D = 1$ downstream the turbine it was observed that the tip vortices were shed from the blade in slightly different courses, the vortices courses can have spread even more at 3 diameters downstream the wind turbine. This might be an explanation to why there seems to be only one or two tip vortices/ or congestions of normal stress at the different positions of the hot-wire probes in the areas of the wake given in the previous sections. One of the tip vortices might appear at one position of the rake and the other two at another position. The phase averaging of the measurements conducted later in the study, in Section 5.5, might reveal if the three tip vortices are still evident at three diameters behind the rotor or if they have merged together.

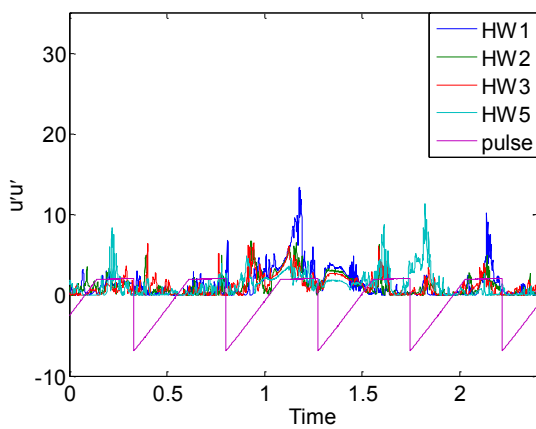
5.3. Time series $X/D = 5$

The values presented in this section all represents five rotations of the model wind turbine.

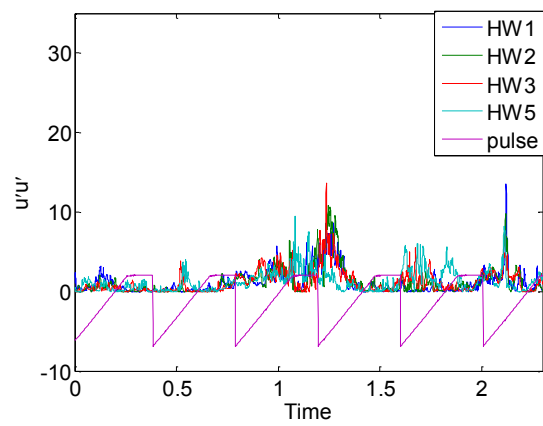
Figure 5.14 (a) and (b) represents the normal stress at $X/D = 5$ downstream the wind turbine rotor at the position given in Table 5.7.

Table 5.7: $X/D = 5$, Position 1 of hot-wire probes

	HW 1	HW 2	HW 3	HW 5
Distance from rotor center [m]	0.5100	0.5238	0.5406	0.5614
z/R	1.133	1.164	1.201	1.248

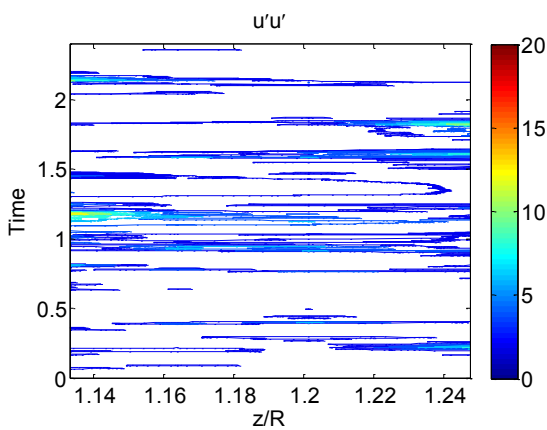


(a) Without grid turbulence

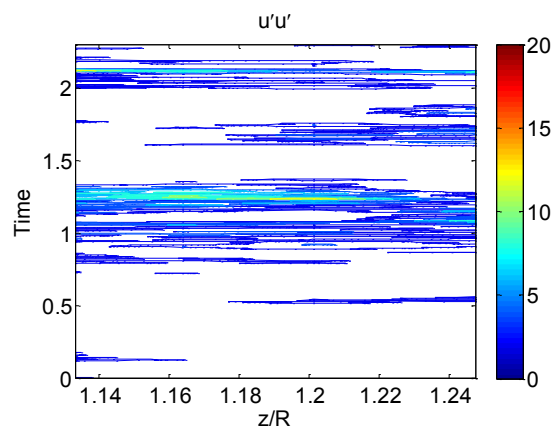


(b) With grid turbulence

Figure 5.14: $X/D = 5$, Position 1 (a) Five rotations without grid turbulence, (b) Five rotations with grid turbulence



(a) Without grid turbulence



(b) With grid turbulence

Figure 5.15: $X/D = 5$, Contour plot, Position 1 (a) Five rotations without grid turbulence, (b) Five rotations with grid turbulence

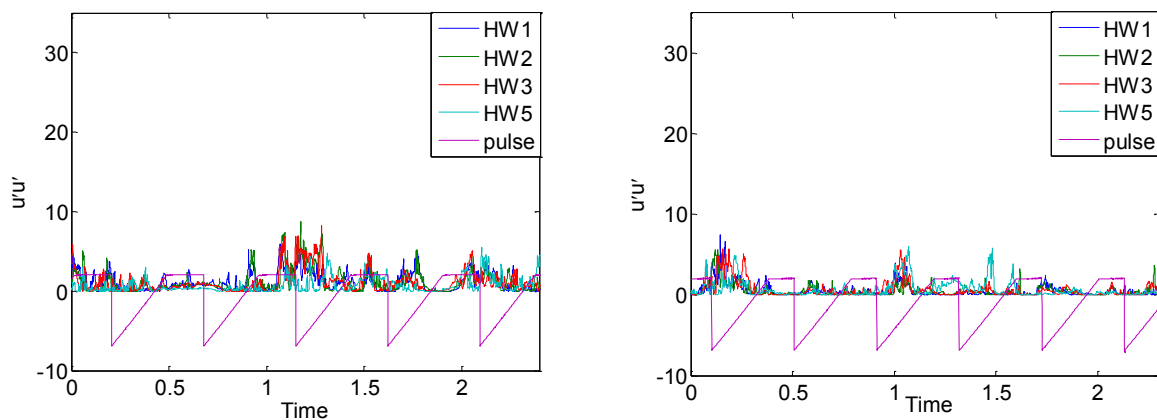
Figure 5.14 (a) and (b) give a clear indication that there are no sign of tip vortices at this position in the wake of the turbine. The tip vortices are most likely broken up or merged together and the flow in the wake seem to be an ordinary turbulent flow. The normal stress has decreased a great deal compared to $X/D = 1$ and $X/D = 3$ downstream the turbine. Thus, when studying Figure 5.14 (a), there are peaks in the normal stress in the wake within the five rotations measured at the positions of hot-wire probe 1 and 5. This might indicate that the tip vortices are just merged and not fully broken up, and that there still is some structure in the wake. While in the wake where the turbine is placed in an incoming flow with turbulence intensity round 5.5 %, Figure 5.14 (b), it seems that the structure is fully broken up.

In Figure 5.15 (a) and (b), the position of the small peaks in the normal stress is indicated by a contour plot. Figure 5.15 (a) indicate that the peak seen in the normal stress in every rotation in Figure 5.14 (a) is not located at the same z/R position in the wake, and it is rather weak. In the case with a turbulent incoming flow, see Figure 5.15 (b), the wake seems to be fully dissolved at this location. Within the first rotation there is almost no normal stress, while in the third and fourth rotation the level on the normal stress is increased.

When studying the normal stress in the wake at a position further from the rotor center, given in Figure 5.16 (a) and (b), (positions are given in Table 5.8) the trends mentioned in the previous section, regarding the one peak in the normal stress within every rotation, is not present.

Table 5.8: $X/D = 5$, Position 2 of hot-wire probes

	HW 1	HW 2	HW 3	HW 5
Distance from rotor center [m]	0.5800	0.5938	0.6106	0.6314
z/R	1.289	1.320	1.357	1.403



(a) Without grid turbulence

(b) With grid turbulence

Figure 5.16: $X/D = 5$, Position 2 (a) Five rotations without grid turbulence, (b) Five rotations with grid turbulence

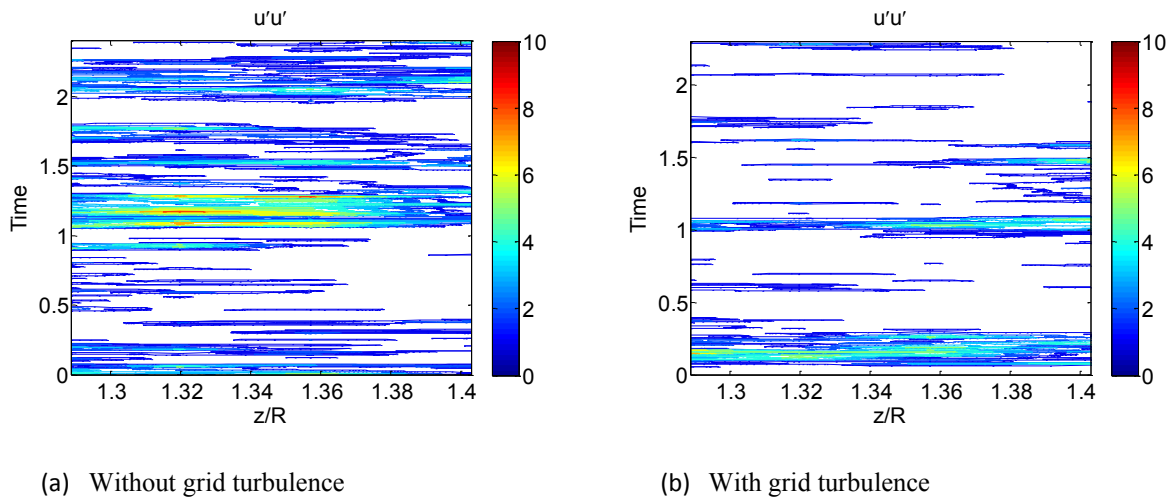


Figure 5.17: $X/D = 5$, Contour plot, Position 2 (a) Five rotations without grid turbulence, (b) Five rotations with grid turbulence

The level of the normal stress have in both cases decreased even more at this location in the wake, as can be seen in Figure 5.16 (a) and (b), and there are no evident peaks repeating itself in the normal stress in either case. Figure 5.17 (a) and (b) are the contour plots of the measurement at this location. There is some difference in the normal stress for the two cases. In the case with grid generated turbulence, the energy is decreased at this location. This coincides with the theory that the wake deficit and thus the turbulent energy in the wake are dissolved at a faster rate when the turbine is placed in a flow with a higher level of turbulence intensity.

5.4. Time averaged turbulent kinetic energy

Based on the mean values from the time series and Equation (3.29), the turbulent kinetic energy from time averaged measurements can be plotted and compared for the cases with and without grid turbulence. In Figure 5.18, Figure 5.19 and Figure 5.20 the turbulent kinetic energy is normalized by the reference free stream velocity for the 3 positions $X/D = 1, 3$ and 5 downstream the model wind turbine. The values are plotted as a function of the position z/R . The blue lines represent the measurements without grid generated turbulence, and the red lines the measurements conducted with an incoming flow with turbulence intensity round 5.5% .

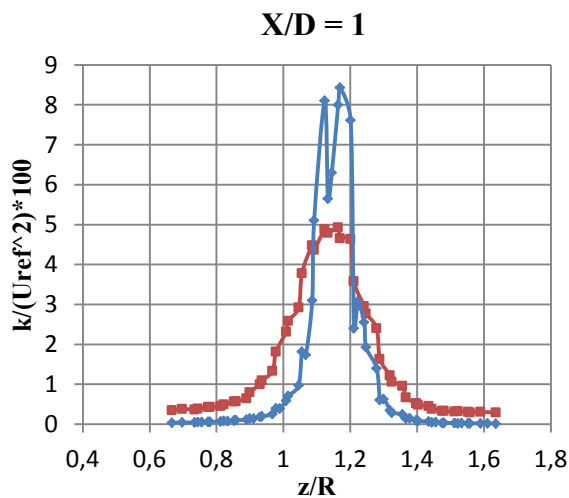


Figure 5.18: $X/D=1$, turbulent kinetic energy with (red line) and without (blue line) grid turbulence

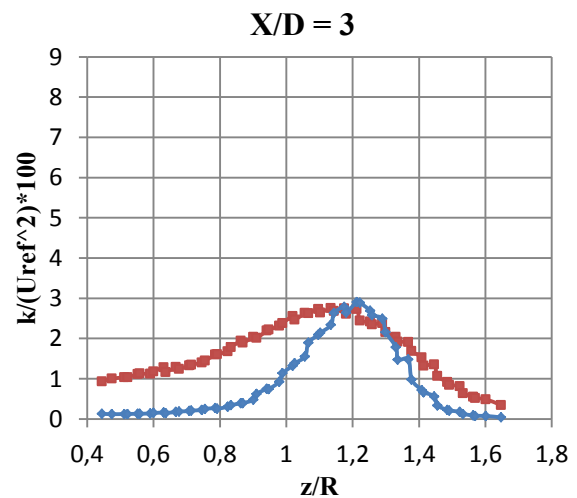


Figure 5.19: $X/D=3$, turbulent kinetic energy with (red line) and without (blue line) grid turbulence

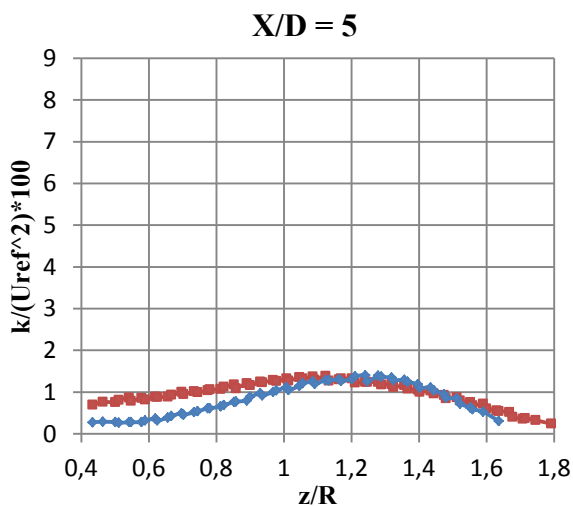


Figure 5.20: $X/D=5$, turbulent kinetic energy with (red line) and without (blue line) grid turbulence

As seen in the figures, the turbulent kinetic energy decreases, or is smeared out in the wake, when moving downstream in the wake of the turbine. This coincides with the theory stating that the turbulent kinetic energy will decrease due to dissipation and diffusion, termed the energy cascade. The turbulent energy at the downstream position in the wake has been smoothed out by spanwise turbulent diffusion. Another observation is that in the case with the grid generated turbulence at $X/D = 1$, the amplitude of the turbulent kinetic energy is decreased compared to the case without grid turbulence. This is due to that the grid generated turbulence affects the wake development in such a way that the turbulence will decay faster, as also predicted in the model by Bossanyi. The increased turbulence level in the free stream has in other words increased the radial transport of energy in the wake leading to a smearing out of the energy; but the total energy beneath the curves in the two cases seems to be in the same order.

At $X/D = 3$ and $X/D = 5$ downstream the wind turbine the turbulent kinetic energy is higher when moving toward the rotor center in the case with grid generated turbulence compared to the case with a low turbulent incoming flow. The level of the energy is quite equal for the two cases, and the peak in the stress is located almost at the same z/R position. However, it seems that the total energy is higher in the case with grid turbulence. This might be a consequence of the increased tip speed ratio, resulting in a reduced lift force, especially at the root of the blade, and thus a reduced power extraction from the incoming flow. This leads to more energy in the wake of the turbine, which is lost in the power extraction.

At $X/D = 3$ downstream the turbine, the turbulent kinetic energy is at a higher level over a wider area for the case with grid turbulence. It's still a small peak in the energy, though not as pronounced as in the case without grid generated turbulence. This is clearly an effect of the turbulent flow causing the wake to expand and be smeared out.

5.5. Phase averaging of the measurements

An averaging of the measurements was conducted by using the pulse signal accumulated by the ramp generator. It was made a Matab script where the converted voltage signal from the 4 hot-wire probes was placed in different bins according to the position of the turbine blades. The drop in the pulse signal, as seen in some of the figures in Section 5.1 to 5.3, indicates the start of a new rotation. Since the pulse signal and the signal from the hot-wire anemometry were logged simultaneously, the index of the drop in the pulse signal could be used to sort the measured velocities. The fluctuating velocities from the anemometers were divided into 180 bins, which mean that each bin represented a two degree rotation of the turbine. This gave a number of 4-6 samples in each bin for each rotation, dependent on number of samples within the rotation. The result matrix was then three-dimensional matrix with *nr. samples* \times 4 (HW) \times 180. The velocities in each bin were then summed up and divided by the number of samples in the bin.

5.5.1. Phase averaged fluctuating velocity, u'

In Figure 5.21 to Figure 5.26 the phase averaged fluctuating velocity, u' , at the given z/R position for all the measurements conducted at $X/D = 1, 3$ and 5 , both with and without grid generated turbulence, are presented in contour plots. The rotation in degrees is represented on the ordinate. The column to the left represents the measurements without grid generated turbulence and the right column with grid generated turbulence. The fluctuating velocity is given as real value, not normalized.

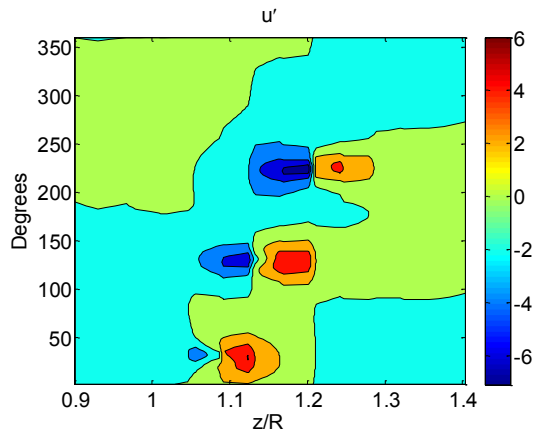


Figure 5.21: X/D = 1, Phase averaged fluctuating velocity without grid turbulence

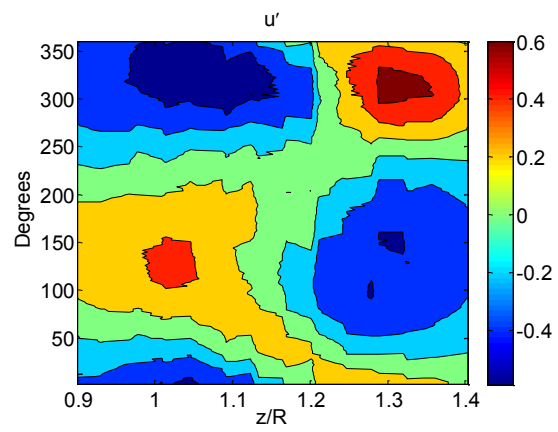


Figure 5.22: X/D = 1, Phase averaged fluctuating velocity with grid turbulence

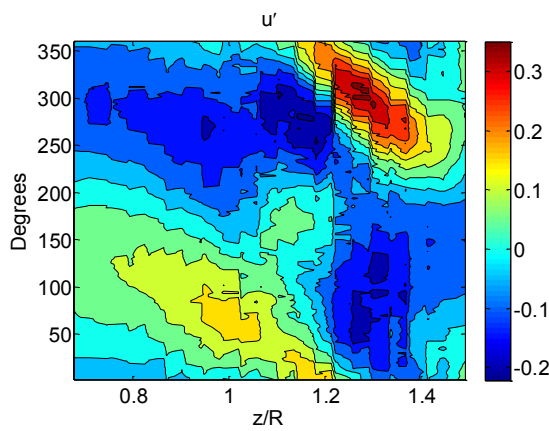


Figure 5.23: X/D = 3, Phase averaged fluctuating velocity without grid turbulence

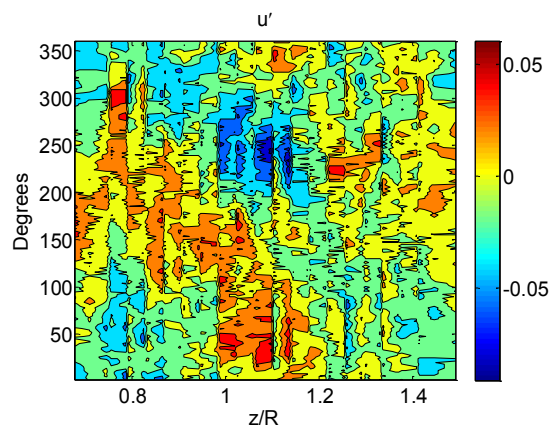


Figure 5.24: X/D = 3, Phase averaged fluctuating velocity with grid turbulence

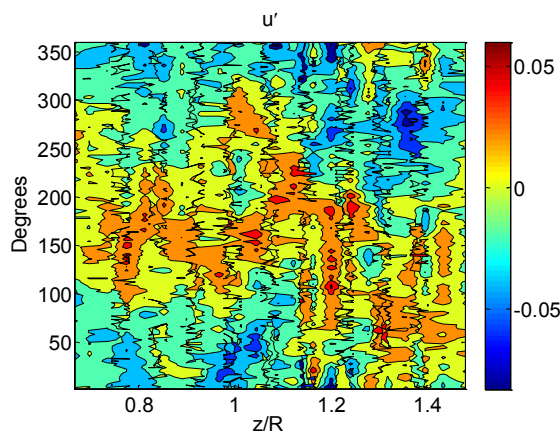


Figure 5.25: X/D = 5, Phase averaged fluctuating velocity without grid turbulence

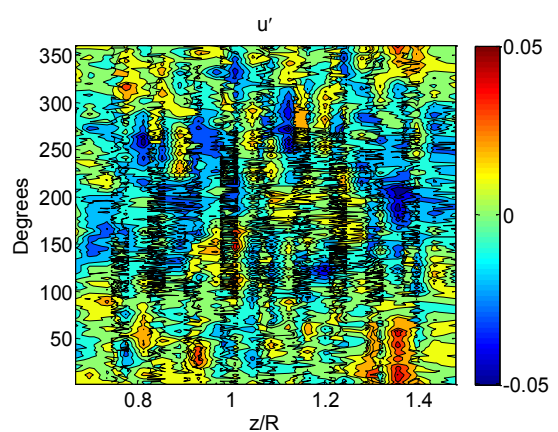


Figure 5.26: X/D = 5, Phase averaged fluctuating velocity with grid turbulence

The figures clearly show both the effect of the grid generated turbulence and the changes in the wake structure at the different positions downstream the turbine. In Figure 5.21 the three tip vortices in the wake are evident. As seen in Section 5.1, when only studying the measurements from 5 rotations of the wind turbine rotor at X/D = 1, the tip vortices are not equally distributed within the 360° and the size of the vortices are unequal.

This is even more clarified in this plot. The tip vortices are seen as a positive and a negative field in the fluctuating velocity. This is due to the rotation of the tip vortices, giving both a negative and a positive velocity compared to the streamwise direction, x . The center of the positive part of the vortices are round $z/R = 1.12$, $z/R = 1.17$ and $z/R = 1.23$, which coincides with the observations conducted in Section 5.1. The sizes of the tip vortices will be studied in the section representing the phase averaged normal stress, Section 5.5.2.

When comparing the phase averaged result at $X/D = 1$ with and without grid generated turbulence, given in Figure 5.22 and Figure 5.21 respectively, the effect of the turbulent incoming flow is evident. The three tip vortices seem to be merged together and there are now only two peaks, or four when counting both positive and negative peaks, in the fluctuating velocity. The level of the fluctuating velocity has decreased with a factor of 10 compared to the case with an incoming flow with low turbulence intensity, and the sizes of the fields with the greatest deviation from the mean velocity are larger when comparing the two cases. Thus, it's rather unlikely that these fields represent the single tip vortices seen in the case without grid generated turbulence, and instead represent the location of merged tip vortices.

When studying the phase averaged fluctuating velocity at $X/D = 3$ downstream the turbine without grid generated turbulence in Figure 5.23, the evident tip vortices seen at $X/D = 1$ are no longer present. There is one clear positive peak located round $z/R = 1.30$ appearing at 300° of the rotation of the wind turbine rotor. The location of the center is in the range between $z/R = 1.19$ to $z/R = 1.40$. In the contour plot for five rotations given in Section 5.2 it was also seen a peak in the normal stress at this locations, though not as wide as the one seen here. This might indicate that the peak seen in Figure 5.23 is a location of the merged tip vortices. As seen, there are clear fields in the wake, which indicates that there is some structure in the wake. However, the level of u' is reduced by a factor of 15 compared to the measurements conducted at $X/D = 1$. Thus, the energy in the wake seems to be spread out at this position downstream the turbine.

In the case with grid turbulence at $X/D = 3$ downstream the turbine, given in Figure 5.24, the flow in the wake seems to be chaotic and unstructured. The level of the fluctuating velocity is still reduced by a factor of 10 compared to the case without grid generated turbulence and a factor of 12 compared to the same case at $X/D = 1$. The chaotic behavior coincides well with what was seen in the figures representing five rotations of the turbine, given in Section 5.2.

At $X/D = 5$, represented in Figure 5.25 and Figure 5.26, the flow seems to be chaotic and unstructured for both cases. This indicates that the wake might be fully dissolved, and the flow in the wake is now an ordinary turbulent flow with no evident structure. The maximum level of the fluctuating velocity is quite equal in both cases. Though, the level of the fluctuating velocity in the case without the grid generated turbulence is quite equal to the case at $X/D = 3$ with a turbulent incoming flow. It seems that the contour plots, and thus the flow, are comparable at these two locations. This might indicate that the wake of the turbine encountered by a turbulent flow recovers at an earlier stage downstream the turbine, which agrees with theory.

5.5.2. Phase averaged normal stress, $u'u'$

In Figure 5.27 to Figure 5.32, the normal stress, $u'u'$, at $X/D = 1, 3$ and 5 downstream the model wind turbine with and without grid generated turbulence are averaged according to the position of the blade. The rotation of the rotor turbine is represented on the ordinate in degrees. The figures to the left is the phase averaged normal stress without grid turbulence, and to the right is the phase averaged normal stress with grid turbulence.

The normal stress is given in real values, not normalized.

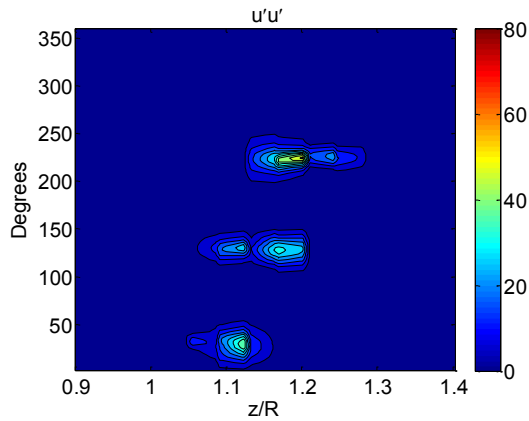


Figure 5.27: $X/D = 1$, Phase averaged normal stress without grid turbulence

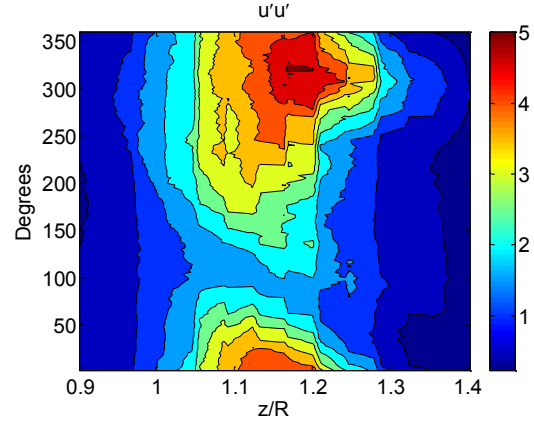


Figure 5.28: $X/D = 1$, Phase averaged normal stress with grid turbulence

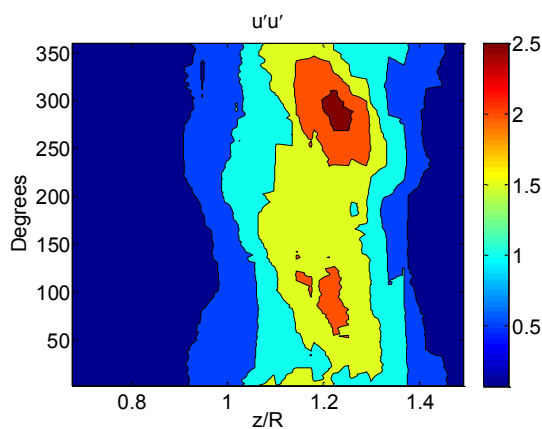


Figure 5.29: $X/D = 3$, Phase averaged normal stress without grid turbulence

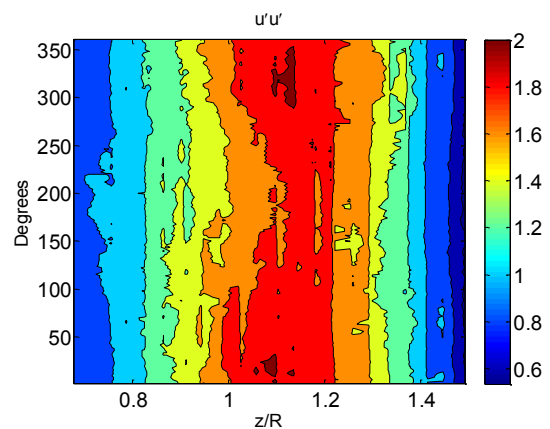


Figure 5.30: $X/D = 3$, Phase averaged normal stress with grid turbulence

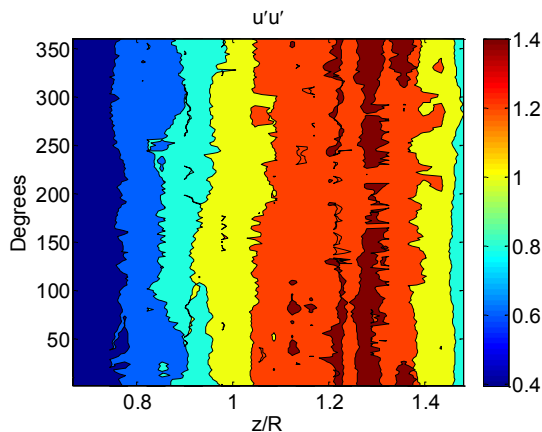


Figure 5.31: $X/D = 5$, Phase averaged normal stress without grid turbulence

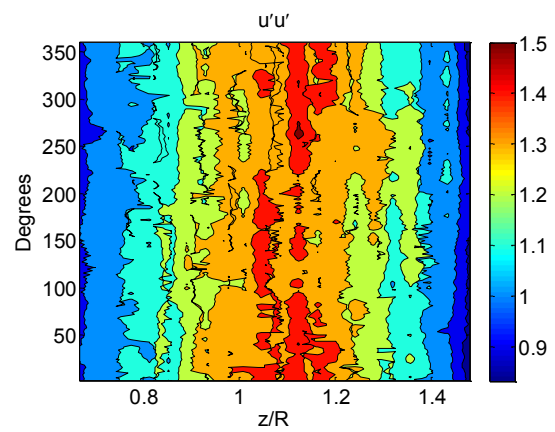


Figure 5.32: $X/D = 5$, Phase averaged normal stress with grid turbulence

To be sure that the results were correct phase averaged, the sum of the normal stress for the 360° at each z/R position was compared to the time averaged normal stress computed in the in-house converting program *hwsconv*. It was a good correspondence between shapes the two different averages. The comparison is given in Appendix A.2.

In Figure 5.27 the three tip vortices are clearly seen as the peaks in the normal stress, and the figure is quite equal to Figure 5.21 representing the fluctuating velocity given in Section 5.5.1. The plot is scaled equal to the contour plots given in Section 5.1 to be able to compare the locations of the tip vortices.

The position and the size of the tip vortices are as seen in previous sections in the study; the tip vortices are of different size and are shifted to the right in the figure. The center of the tip vortices, or the peak value in the normal stress, is located round 30° , 128° and 224° based on the phase averaged measurements. This equals a distance of 98° and 96° between, respectively, tip vortex one and two, and two and three. The distance between the third and the first tip vortex then becomes 166° .

Using a criterion that the center of the tip vortex is located where the normal stress is higher than the mean value for each accumulation of normal stress, a study on the size of the tip vortices can be conducted. The first tip vortex, emerging within the first 70° of rotation, is located between $z/R = 1.05$ to $z/R = 1.15$, giving a distance of $4.50E-2$ m, with the center located between $z/R = 1.09$ to $z/R = 1.13$. The center width corresponds to a distance of $1.80E-2$ m. The second tip vortex emerging, located between 100° and 160° of the rotation of the turbine rotor, has its extremes points at $z/R = 1.08$ and $z/R = 1.21$. The center is located between $z/R = 1.09$ and $z/R = 1.20$ which equals a distance of $4.95E-2$ m. The third and last tip vortex emerges between 190° and 260° of the rotation of the turbine rotor. It has its extreme points at $z/R = 1.13$ and $z/R = 1.28$. The center of the tip vortex is located between $z/R = 1.15$ and $z/R = 1.25$, which equals a distance of $4.50E-2$ m.

The strength of the tip vortices is also unequal. The first tip vortex has a maximum normal stress round 40.0, while the second tip vortex is weaker, with a maximum value of 31.7. The strongest tip vortex is the third, which is clearly seen from the figure, with a maximum value of 51.4.

In Figure 5.28, representing the case at $X/D = 1$ downstream the turbine with grid generated turbulence, the normal stress is decreased by a factor of round 10 compared to the case at $X/D = 1$ without grid turbulence. There is a continuous field in the wake with increased normal stress, stretching from round 150° around to 50° with a center at 320° of the rotation of wind turbine rotor. Since there is no indication of three peaks representing the tip vortices, is it likely to believe that this might be location of the merged tip vortices. The fact that there is a continuous field with only one “open space” during the rotation, indicates that the tip vortices have caught up with each other. This might also explain the peaks seen in Section 5.1 when presenting the measurements for only five rotations of the turbine, and why they emerged at different z/R positions. There is, in other words, still a structure in the wake at this point downstream the turbine, and thus, the grid generated turbulence have not dissolved the whole wake structure to an ordinary turbulent flow.

The phase averaged measurements conducted at $X/D = 3$ downstream the turbine without grid turbulence is given in Figure 5.29. The level of the normal stress has decreased by a factor of 20 compared to the measurements conducted at $X/D = 1$.

In the figure there are two fields in the wake with increased normal stress, one at 100° and one at 290° of the rotation, both appearing round $z/R = 1.22$, but the peak located at 290° is much stronger than the other. One explanation might be that two of the tip vortices have merged together, creating the field with greatest normal stress, while the third tip vortex is represented by the weaker peak in the normal stress. The fact that the tip vortices are located quite close to each other in the wake, as seen at $X/D = 1$, and that the vortex located in between the two other vortices is the weakest one, is a good support to this statement. However, there is an increased normal stress stretching over the area between $z/R = 1.10$ to $z/R = 1.31$, which might indicate that the weaker tip vortex moves around.

At $X/D = 3$ with grid generated turbulence, presented in Figure 5.30, there seem to be a continuous field through the entire wake with increased normal stress. It is likely that the field seen at 1 diameter downstream the turbine has been smeared out to this one big field since the z/R range of the field is the same in both cases, ranging from $z/R = 0.90$ to $z/R = 1.30$. The level of the normal stress has only decreased by a factor of 2.5 compared to the same case at $X/D = 1$. This is a small reduction compared to the decrease seen in the case without grid generated turbulence.

The phase averaged measurements at $X/D = 5$ downstream the turbine for the case without and with grid turbulence are given in respectively Figure 5.31 and Figure 5.32. In neither case are there any signs of distinct peaks representing the tip vortices. The figure representing the case without grid generated turbulence is quite equal to Figure 5.30, who represents the measurements conducted at $X/D = 3$ with grid turbulence. Based on this, one might believe that the flow field in the wake at $X/D = 5$ with a low turbulent flow is quite equal to the flow field in the wake at $X/D = 3$ in a flow with turbulence intensity round 5.5 %. This coincide with the theory, claiming that the wake recover faster when introduced to a higher free stream turbulence. There is however a slightly reduced normal stress at $X/D = 5$ in the case without grid generated turbulence compared to $X/D = 3$ with grid turbulence.

The level of the normal stress at $X/D = 5$ is equal in both cases. The normal stress in wake exposed to the grid generated turbulence is not as clearly divided into fields as in the case without grid turbulence. This indicates that the flow pattern in the wake of the turbine in the case with grid turbulence is more disturbed and broken up.

5.6. Study on one tip vortex

Based on the contour plots representing the phase averaged measurement, specific locations in the wake has been selected to study the behavior of one of the tip vortices. In the next sections, a study on the stability of one of the tip vortices in the streamwise direction, x , will be conducted based on statistical values from the rotations of the wind turbine rotor within different time series.

5.6.1. Without grid generated turbulence, $X/D = 1$

It is clear from Figure 5.27 in Section 5.5.2 (the phase averaged normal stress) that one of the tip vortices at $X/D = 1$ downstream the turbine, measured in the case with an incoming flow with low turbulence intensity, is located within the first 100° of each rotation at a location round $z/R = 1.12$. Based on this, the hot-wire measurements representing the fluctuating velocity round this location for the first 100° for each rotation were selected and studied. The positions of the hot-wire probes are specified in Table 5.9.

Table 5.9: $X/D = 1$, Position 1 of hot-wire probes

	HW 1	HW 2	HW 3	HW 5
Distance from rotor center [m]	0.475	0.4888	0.5056	0.5264
z/R	1.056	1.086	1.124	1.170

To locate the where, or which hot-wire probe detected the tip vortex, a Matlab script was made to sort out the maximum fluctuating velocity within this selected data set for every rotation in the four time series. This location was assumed to represent the location of the tip vortex. Further, it was summed up how many maximum points each probe detected, and a probability density function of the maximum fluctuating velocity was made as a function of z/R . The distribution is given in Figure 5.33. The values are normalized by the total number of rotations, which is 1278 in these four time series.

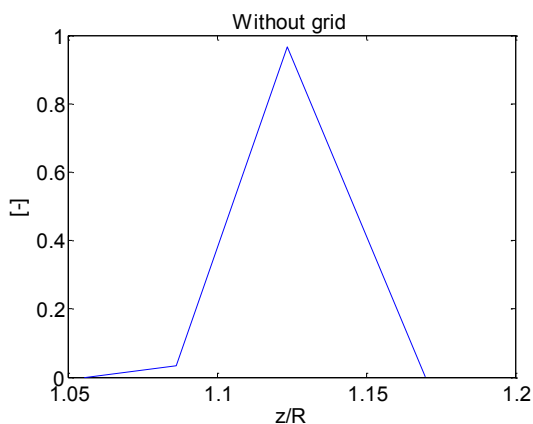


Figure 5.33: Position 1, PDF on the location of one tip vortex, $X/D = 1$ without grid turbulence

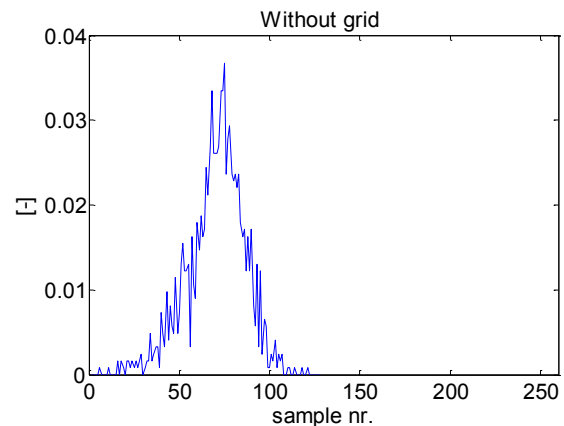


Figure 5.34: Position 1, Time of which u' maximum was measured with hot-wire probe nr. 3 in each rotation, $X/D = 1$ without grid turbulence

It is clear from Figure 5.33 that the probe located at $z/R = 1.124$, hot-wire probe number three, measured the highest fluctuating velocity most frequently, with 96.54 % of the times of the total number of rotations within the time series. This corresponds well to the location of the tip vortex found when presenting the phase averaged normal stress at $X/D = 1$ without grid generated turbulence. It was also measured at the locations of the other three probes every now and then, as can be seen in the distribution.

After locating the tip vortex, a study on the meandering of the tip vortex in the streamwise direction within each rotation could be conducted. This was done by finding when the maximum fluctuating velocity was measured within the first 100° of rotation at hot-wire probe number three for the different rotations. In one rotation it was measured round 940 samples (varied with one or two samples) which gave a total of 261 samples within the first 100° of rotation.

Figure 5.34 illustrates how the maximum fluctuating velocity measured with hot-wire probe three is distributed according to the number of sample within each rotation. The values are normalized by the total number of maximum u' points measured with hot-wire probe number three. The sampling frequency during the measurements was, as mentioned, 20 kHz, and the free stream velocity was 10.2 m/s. This gives a distance of $5.10E-4$ m variation between each sample in the streamwise direction.

The figure clearly illustrates that the location of the maximum fluctuating velocity sampled is gathered round sample number 87. It is a quite even variation around this measurement point, which gives the impression that the tip vortex meanders slightly back and forth in the streamwise direction. However, the variation is somewhat larger to the left in the figure. In other words, the tip vortex seems to appear at an earlier stage within the first 100° of the rotations more often than at a later stage. Though, the range where the maximum u' appears most frequently seems be from sample number 60 to 90. This equals a distance of $1.53E-2$ m. The total spread in the figure is 121 samples, giving a distance of $6.17E-2$ m.

To be sure that this slight meandering in the streamwise direction seen in the previous section was not a contingency, the same procedure was conducted on a measurement point shifted to the right. The position of the hot-wire probes are given in Table 5.10.

Table 5.10: $X/D = 1$, Position 2 of hot-wire probes

	HW 1	HW 2	HW 3	HW 5
Distance from rotor center [m]	0.510	0.5238	0.5406	0.5614
z/R	1.133	1.164	1.201	1.248

At this measurement point hot-wire probes 2, 3 and 5 should be placed as far to the right that hot-wire probe number 1 should measure all the maximum fluctuating velocities belonging to the tip vortex within the first 100° of rotation.

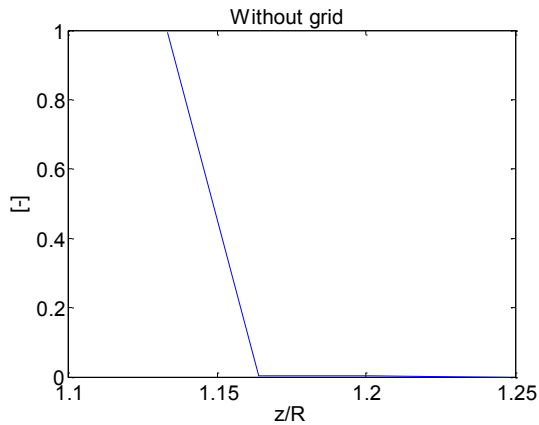


Figure 5.35: Position 2, PDF on the location of one tip vortex, $X/D = 1$ without grid turbulence

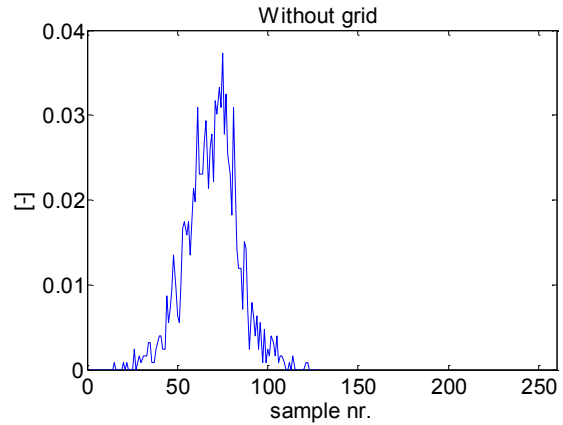


Figure 5.36: Position 2, Time of which u' maximum was measured with hot-wire probe nr. 1 in each rotation, $X/D = 1$ without grid turbulence

As seen in Figure 5.35 nearly all, 99.37 % to exact, of the maximum points were located at the position of hot-wire probe number 1. The values in the figure are normalized by the total number of rotations in the four time series, which was 1278 at this measurement point in the wake.

Conducting the same analysis as for the previous measurement point at $z/R = 1.12$, Figure 5.36 was obtained. Also in this figure there is a variation of when the maximum fluctuating velocity was measured when comparing the different rotations. It is a clear peak around sample number 75, and the variation is quite equal in each direction in the figure. The total spread is 100 samples, giving a distance of $5.10E-2$ m, while the greatest variation lies between sample numbers 60 to 85, giving a distance of $1.28E-2$ m.

Thus, it seems like the location of the tip vortices is not as stable in the streamwise direction at $X/D = 1$ downstream the wind turbine when the turbine is placed in an incoming flow with low turbulence intensity.

5.6.2. With grid generated turbulence, $X/D = 1$

To see the effect of the grid generated turbulence on the wake, the same analyses as conducted in the previous section, Section 5.6.1, was performed on the measurements from the same locations, but now with an incoming flow with turbulence intensity around 5.5 %. Figure 5.37 gives the distribution on where the maximum fluctuating velocity was measured at the positions given in Table 5.9, with grid generated turbulence in the wind tunnel. The values are normalized by the total number of rotations in the four time series representing the measurement point, which was 1428.

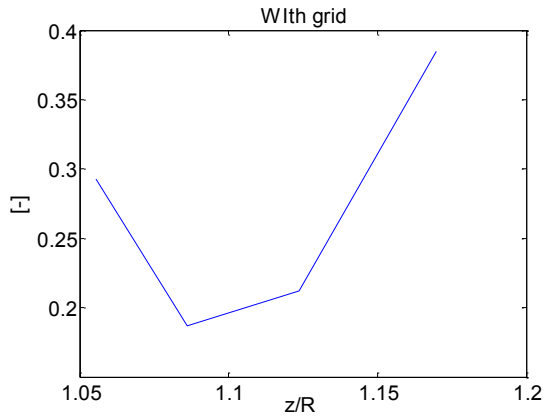


Figure 5.37: Position 1, PDF on the location of one tip vortex, $X/D = 1$ with grid turbulence

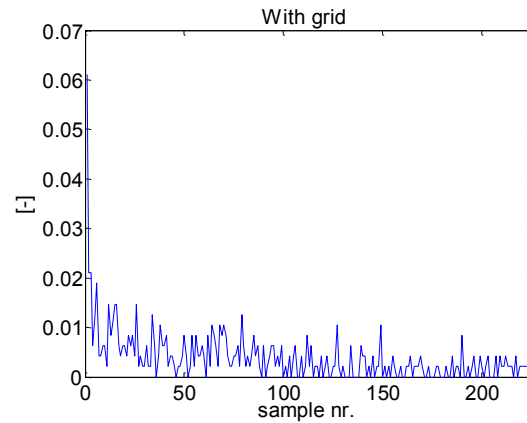


Figure 5.38: Position 1, Time of which u' maximum was measured with hot-wire probe nr. 5 in each rotation, $X/D = 1$ with grid turbulence

In the case with grid generated turbulence, the rotational speed of the turbine was round 1500 rpm, giving a total number of round 810 samples per rotation. A rotation of 100° is then represented by the first 225 samples for each rotation in the time series.

When comparing the distribution at this measurement point for the case with and without grid turbulence in the wind tunnel, Figure 5.37 and Figure 5.33 respectively, there is an evident difference. In the case with grid turbulence the maximum u' is more spread out over the range of z/R given in the figures. However, the location of hot-wire probe number five and one seems to be the two locations where the maximum value appears most frequently. This might indicate a meandering in the streamwise direction and instability in the tip vortex, or the merged tip vortices. The extreme point of the field with increased normal stress, seen in Figure 5.28 when presenting the phase averaged normal stress located within the first 100° of rotation, is in this z/R range. The fact that hot-wire probe number five is the probe where the maximum fluctuating velocity occurs the most, might be due to that $z/R = 1.17$ is located in the middle of the increased normal stress field seen in Figure 5.28.

Based on Figure 5.37, it was chosen to study the appearance of the maximum u' within the different rotations for hot-wire probe number five, located at $z/R = 1.17$. Figure 5.38 illustrates the distribution according to when maximum u' was measured for the different rotations at hot-wire probe five. Also in this figure is there an evident change between the cases with and without grid generated turbulence. In the case without grid generated turbulence in the wind tunnel it was a clear peak where u' maximum appeared most frequently. Now it is spread out over the entire selected data set, with just a narrow peak in the beginning of the rotations. The total distance over where the maximum fluctuating velocity is measured is $11.48E-2$ m in the streamwise direction. The small peak round sample number 1 in Figure 5.38 corresponds well to the location of the merged tip vortices, located within 0° to 50° , found in the phase averaged measurements.

When conducting the same analysis on a measurement point further from the rotor center, given in Table 5.10, the same trends appear. However, the distribution on where the maximum fluctuating velocity is located within the given z/R area is more evident. As seen in Figure 5.39, hot-wire number one, located at $z/R = 1.13$, measured almost 50 % of the maximum u' for the 1482 rotations in these four time series.

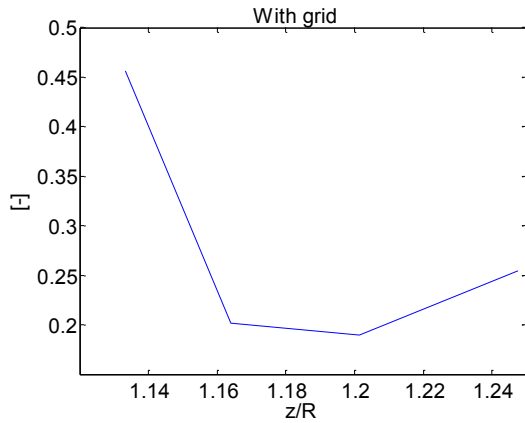


Figure 5.39: Position 2, PDF on the location of one tip vortex, $X/D = 1$ with grid turbulence

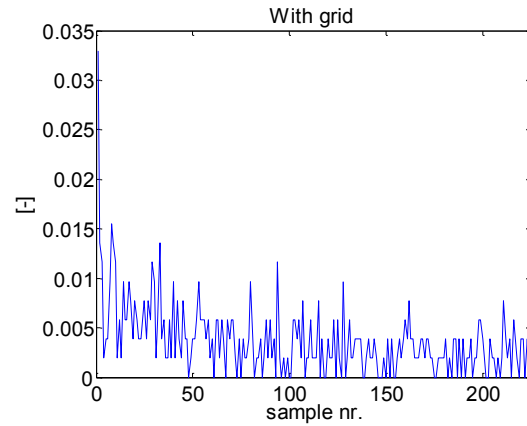


Figure 5.40: Position 2, Time of which u' maximum was measured with hot-wire probe nr. 1 in each rotation, $X/D = 1$ with grid turbulence

Based on this, the time at which the maximum fluctuating velocity occurred within the first 100° in each rotation for hot-wire probe number one was studied. Figure 5.40 illustrates the distribution. It is clearly the same trends as seen at the position given in the previous section. The maximum values are smeared out over the first 100° of rotation, with a small peak at the beginning of the rotations. There is no accumulation round one specific point as in the case without grid generated turbulence in the wind tunnel.

That fact that it is such an evident change between the two cases is no surprise. As seen in the phase averaged measurements, the tip vortices seems to have merged together when the turbine is placed in an incoming flow with turbulence intensity typical for atmospheric turbulence intensity.

5.7. Cross correlation of the flow field in the wake

It has been conducted two cross correlation calculations between the probes to illustrate how the flow behaves in a given area in the wake and how well the flow is correlated. The cross correlations are computed by the use of Equation (3.30).

The first cross correlation given in this section is related to one specific z/R location. Based on all the measured time series that included this position for one of the four hot-wire probes, the correlation between the probes, and the distance between them was found. It is used a time delay increment of 30 samples in the cross correlation, which equals $1.5E-3$ seconds.

In Figure 5.41 and Figure 5.42, $z/R = 1.20$ is used as “zero point”. As seen from the figures given in the Section 5.5.2, the measurements conducted at $z/R=1.20$ should detect at least one, maybe two, of the tip vortices. Since the hot-wire rake was traversed with an increment of $3.50E-2$ m in the horizontal direction between each measurement, in the range between $z/R=0.67$ to $z/R=1.64$ at $X/D = 1$, all four probes was used to conduct measurements relatively close to $z/R=1.20$.

Figure 5.41 shows the results obtained by a cross correlation between the fluctuating velocity signals from the measurements conducted at $X/D = 1$ without grid turbulence. The distance given in the figure is normalized with respect to the radius of the model wind turbine. On the horizontal axis the distance represents the deviation from the zero point $z/R = 1.20$, where the negative direction is directed towards the rotor center and positive direction is increasing distance to the rotor center. The total spread is $10.26E-2$ m. On the vertical axis the delay is represented as numbers of rotations, which equals a bit over five rotations of the wind turbine rotor.

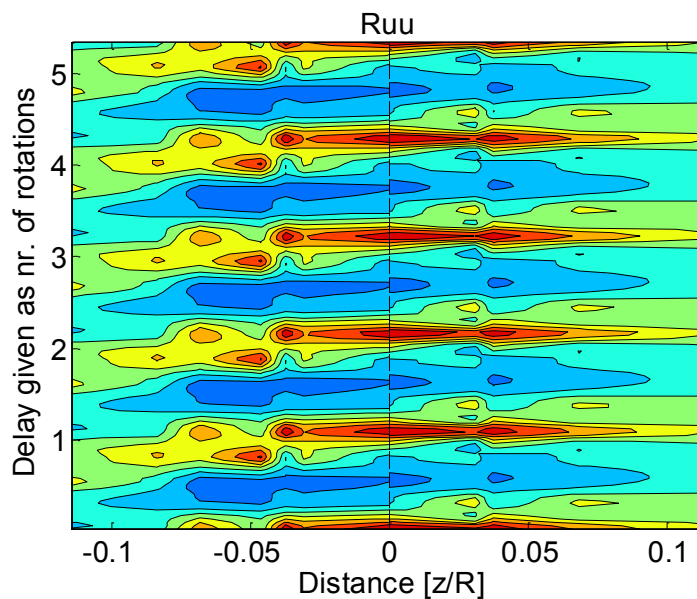


Figure 5.41: Cross correlation $X/D = 1$ without grid with $z/R = 1.2$ as zero point

As seen in the figure, the pattern repeats itself throughout the five rotations. The width of the strong correlated fields, indicated by the dark red fields, is round $4.50E-2$ m. This is the same distance as found in Section 5.5.2 for the third tip vortex at $X/D = 1$ in the case without grid generated turbulence. This strong correlated field indicates the size of which the flow is well correlated, and thus is an indication of the location and size of the tip vortex.

Comparing Figure 5.41 to Figure 5.27, whom represents the phase averaged measurements, the tip vortex captured in this cross correlation seems to be the third tip vortex. Since the tip vortices are so well defined in this location of the wake, the tip vortex is clearly seen in the cross correlation.

As seen in the figure, the flow has a greater correlation when moving to the right in the figure, which is directed further from the rotor center. This means that the flow is directed away from the center line in the wake of the turbine, and expanding downstream, which coincides with the theory.

Figure 5.42 presents the cross correlation from the same z/R positions as given in the previous section, however, now it represents the cross correlation in the case with an incoming flow with turbulence intensity round 5.5 %. The distance and delay is normalized in the same way as in the previous case.

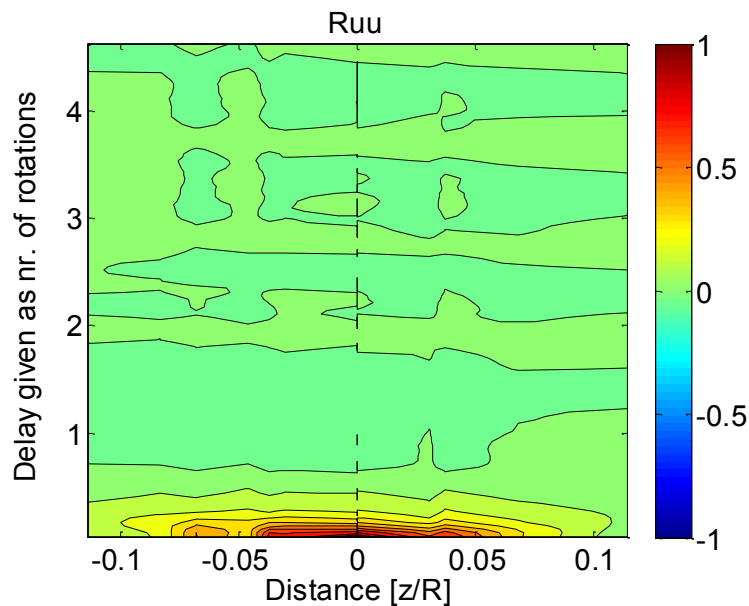


Figure 5.42: Cross correlation $X/D = 1$ with grid generated turbulence with $z/R = 1.2$ as zero point

In the cross correlation the delay equals 4.5 rotations of the turbine. The figure clearly shows that there is no correlation in the flow when moving downstream in the wake of the turbine. This indicates that the flow in the wake is random, chaotic and unstructured with no correlation between the different positions in the wake at $X/D = 1$ when the model turbine is placed in an incoming flow with turbulence intensity typical for atmospheric turbulence intensity. There is however a clear correlation right around in the center of the zero point, which is as expected. This corresponds well to the observations seen earlier in the study.

The second cross correlation conducted is based on the point (index) of which the maximum fluctuating velocity occurs most frequently within the different sets of time series (total of four time series within one set) for the first 100° of rotation of the turbine rotor. This point is found using the same method used in Section 5.6. The index of which the maximum fluctuating velocity occurs most frequently is found for the time series where the hot-wire probes are located close to $z/R = 1.1$. In other words, the cross correlation is based on the zero point, $z/R = 1.10$, and will indicate how the tip vortex seen in the Section 5.6 is correlated within a given area of the flow in the wake. The cross correlation is based on the measurements at $X/D = 1$ in an incoming flow with low turbulence intensity.

The index point, found as described in Section 5.6, within each rotation for the reference probe is multiplied with all the fluctuating velocities within the same rotation for the other probes. The products between two probes are then summed up for each of the locations (index), and divided by the number of rotations. Further, this is divided by the variance of the time series for reference probe. This will give the mean cross correlation in z direction in the flow for that specific tip vortex within the rotations. The cross correlation is given as a contour plot in Figure 5.43.

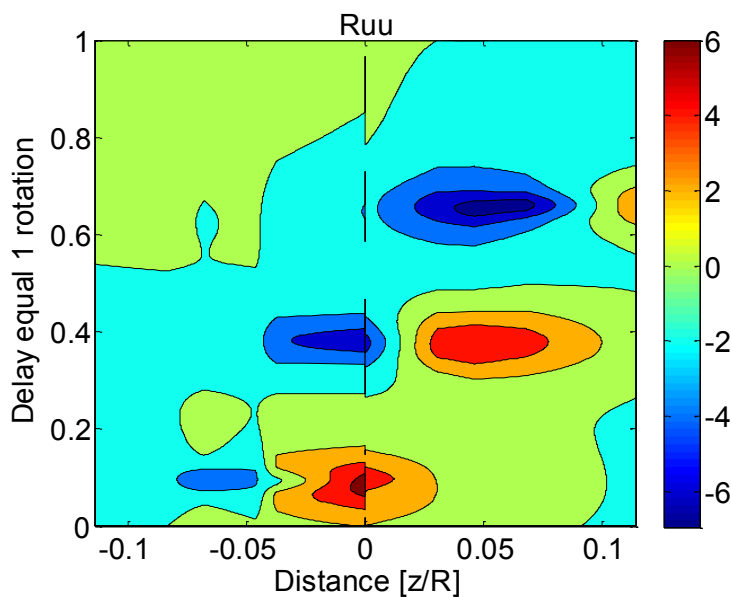


Figure 5.43: Cross correlation of the tip vortex located within the first 100° of rotation

The figure shows that the greatest correlation is at a delay round 0.1, which equals a rotation of round 36° of the turbine rotor. This coincides to the location found in the phase averaged measurements, which is as expected, since the correlation is based on the tip vortex located at this location.

The tip vortex seems to have a greater correlation when moving towards the centerline of the wake, in other words, towards the left in the figure. However, the resolution in the correlation is not as great due to the restricted number of hot-wire probes used during the measurements.

It is clear that the tip vortex is correlation to the two other tip vortices in the wake of the turbine. The center of the second tip vortex seems to be located at a distance of $2.25E-2$ m to the right in the figure, directed outward towards the free stream, from the reference tip vortex. The center of the third tip vortex is not seen in this correlation due to the narrow distance between the extreme points of the rake ($5.1E-2$ m). However, there is an indication of its presence at the edge of the correlation at a delay round 0.7.

Based on this correlation it seems that the tip vortices are located with a distance of round 108° between one another. This leaves a distance of 144° between the third and the first tip vortex.

5.8. Power spectral density function, PSD

A Fast Fourier Transformation (FFT) was conducted on some of the measurements point to convert the time series to frequencies using the in-house Fortran program *spac-mac-big-ASCII*. This allows the strength of the variation in the time series as a function of frequency to be described using a power spectral density function (PSD). In the FFT it was used a Hanning style window, and the number of FFT was 145.

The spectrum is based on the time series from only one of the hot-wire probes. The analysis is conducted on measurements at $X/D = 1$ and 3 downstream the turbine, both with and without grid generated turbulence.

The selected measurement points are chosen on the basis on the location of the tip vortices and increased normal stress seen in Section 5.5.2.

5.8.1. $X/D = 1$

Figure 5.44, Figure 5.45 and Figure 5.46 illustrates the distribution of the energy at respectively the locations $z/R = 1.050$, $z/R = 1.133$ and $z/R = 1.201$ as a function of frequency. The dimension of the function is in other words represented by power per unit of frequency. The red lines represent the case without grid turbulence, while the blue line represents the case with grid turbulence. The values are normalized by the maximum $f^* \Phi_{uu}$ within each PSD.

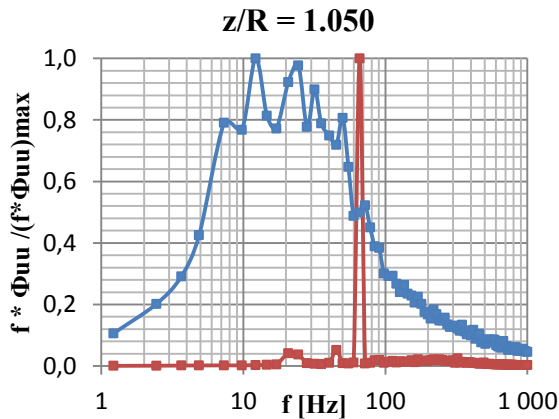


Figure 5.44: PSD of measurements conducted at $z/R=1.050$, $X/D = 1$ with (blue line) and without (red line) grid turbulence

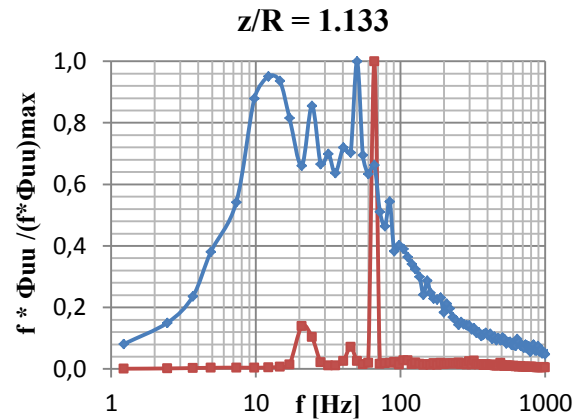


Figure 5.45: PSD of measurements conducted at $z/R=1.133$, $X/D = 1$ with (blue line) and without (red line) grid turbulence

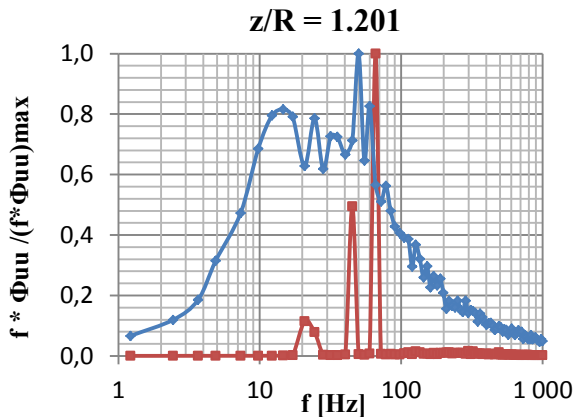


Figure 5.46: PSD of measurements conducted at $z/R=1.201$, $X/D = 1$ with (blue line) and without (red line) grid turbulence

The three peaks mentioned in Section 3.4.3 are clearly present in all the spectrums representing the case with an incoming flow with low turbulence intensity. The rotational frequency of the turbine in this case was 21.67 Hz, and for every z/R position of the probe there is a peak close to 21 Hz. This peak in the spectrum means that there is one incidence occurring once in each rotation. This might be due to that one of the tip vortices is shed different from the two other, which is a result from different loading on the turbine blades, as mentioned earlier in the report. It could also be that one of the tip vortices has a different strength than the other two vortices, as also has been seen earlier in the study.

The second peak is also present in every spectrum with a frequency round 45 Hz. This means that there is some repeating pattern occurring two times during the rotations. The third peak, occurring at a frequency of 66 Hz in every spectrum for the case with an incoming flow with low turbulence intensity, represents the three tip vortices and is the most evident peak in every spectrum. As can be seen by the PSD representing the measurements with an incoming flow with low turbulence intensity, there are no evident noise in the flow, which would have occurred as peaks at frequencies other than the 3P's.

When comparing the three spectrums representing the case without grid generated turbulence, the size of the first and second peak varies with the z/R position of the probe. In Figure 5.44 the two peaks, 1P and 2P, are barely visible. The position $z/R=1.05$ is quite close to the rotor center, and when studying the position of the tip vortices from the phase averaged results in Figure 5.27, the tip vortices locations are further from the rotor center. However, the hot-wire probe still detects the presence of the tip vortices in the wake of the turbine.

The fact that the two first peaks are small in Figure 5.44, compared to the two other z/R positions of the probe given in Figure 5.45 and Figure 5.46, is mainly due to that the values are scaled down with the maximum $f^*\Phi_{uu}$ for the different time series. The highest value of $f^*\Phi_{uu}$ is actually at $z/R = 1.05$, with a value of 3.77. For the $z/R = 1.13$ the maximum value of $f^*\Phi_{uu}$ is 2.26 and for $z/R = 1.201$ $(f^*\Phi_{uu})_{max} = 2.064$. This indicates that the presence of the tip vortices in the three selected time series is strongest at $z/R = 1.05$, which might be due to that at this location the variations of the tip vortices is not “visible”, and only the presence of the vortices is detected.

When moving further from the rotor center, to $z/R = 1.13$ given in Figure 5.45, both the first and the second peak increase, mainly due to the decreased maximum value of $f^*\Phi_{uu}$. Though, when scaling the amplitudes in Figure 5.45 with $(f^*\Phi_{uu})_{max}$ from $z/R = 1.05$, there is still a small increase in the first and second peak. This indicates that the energy in the time series measured at $z/R = 1.13$ is more spread over the two other frequencies 1P and 2P, than at $z/R = 1.05$.

At position $z/R = 1.13$, the first peak has increased the most compared to $z/R = 1.05$, and when comparing it to Figure 5.46 representing $z/R = 1.20$, there is almost no change. This might indicate that the first peak is connected to the different loading of the turbine blades since there is almost no change in this peak between these two measurements points. The tip vortex that causes this peak might be shed in a different course than the two other, or be of different strength. The increase in 2P is more interesting. This indicates that there is some interaction between the tip vortices in a way that they might pulsate between one another.

However, the second peak increase a great deal when moving from $z/R = 1.13$ to $z/R = 1.201$. When scaling the values with the maximum $f^*\Phi_{uu}$ found at $z/R = 1.05$, the second peak is still greatest at $z/R = 1.20$, which indicates that interaction between the tip vortices is even stronger at this location. This might, as mentioned, be caused by a pulsation between the tip vortices; the first tip vortex pulsates towards the second tip vortex, and the second tip vortex pulses towards the third. In other words, there seems to be an instability and interaction between the tip vortices. The pulsation may lead to a merging of two of the tip vortices further downstream in the wake.

A trend for all the figures is that the energy is much more spread out when the turbine is placed in an incoming flow with turbulence intensity typical for atmospheric turbulence. There are still some peaks representing a repeating occurrence in the flow in the case with the grid generated turbulence. The rotational frequency of the turbine during the measurements with grid generated turbulence was 25 Hz.

This means that the 3P's should be located round 25 Hz, 50 Hz and 75 Hz. The maximum value of $f*\Phi_{uu}$ is round 0.4 for all the z/R locations.

In Figure 5.44, representing $z/R = 1.05$, the greatest peak is at a frequency of 12 Hz in the case with grid turbulence, which is half of the rotational frequency. There are peaks appearing at the two first P', at 25 Hz and 50 Hz. At the last P, 75 Hz, there is no apparent peak in the specter. This might indicate that the tip vortices have already merged or are not detectable at this point in the flow when the turbine is exposed to a turbulent flow.

In Figure 5.45, representing the spectrum for position $z/R = 1.13$, there are still two clear peaks at the first two P'2 in the specter representing the case with grid generated turbulence. When studying the specter even closer, there is a small hint of an increased energy at 70 Hz. This might be the last P, representing the tip vortices in the wake. However, the peak is barely visible.

The PDS for when the turbine is placed in an incoming flow with a turbulence intensity round 5.5 %, at position $z/R = 1.20$, is given in Figure 5.46. Also at this location the two first P's, 25 Hz and 50 Hz, are visible in the figure. The second P at 50 Hz is actually the greatest peak in the spectrum. Neither at this position is there any clear sign of the three tip vortices in the wake, which should be represented by a peak round 75 Hz.

One common feature for the two cases with and without grid turbulence is the increased energy at the second P at position $z/R = 1.20$.

5.8.2. $X/D = 3$

The power spectral density function from measurements conducted at $X/D = 3$ downstream the model wind turbine are given in Figure 5.47 and Figure 5.48. The chosen measurements point are $z/R = 1.13$ and $z/R = 1.21$ based on the phase averaged normal stress at $X/D = 3$ given in Section 5.5.2.

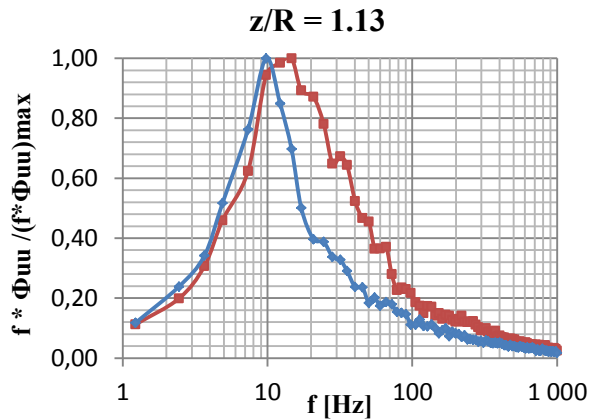


Figure 5.47: PSD of measurements conducted at $z/R=1.13$, $X/D = 3$ with (blue line) and without (red line) grid turbulence

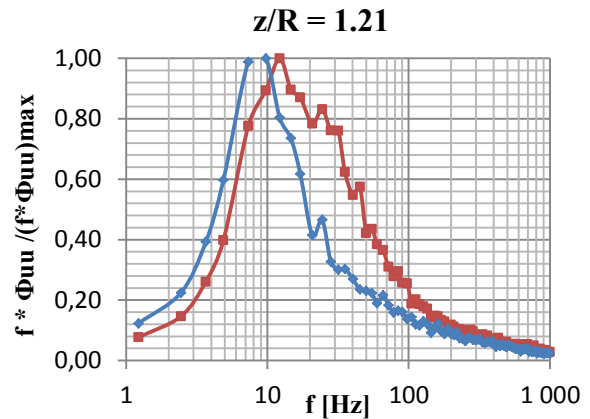


Figure 5.48: PSD of measurements conducted at $z/R=1.21$, $X/D = 3$ with (blue line) and without (red line) grid turbulence

As seen in the figures the energy distribution as a function of frequency is quite equal in both the cases. However, the spectrum without grid turbulence is shifted a bit to the left. This might be due to the reduced rotational frequency of the turbine in the case with an incoming flow with low turbulence intensity.

The fact that there are no clear peaks indicates that the tip vortices are merged together or broken up in both cases, and that the flow field in the wake is quite equal for both with and without grid generated turbulence in the wind tunnel. Hence, there are no specific oscillating patterns within the time series.

5.9. Final discussion

The grid generated turbulence did not give a significant change to the power or thrust coefficient curves. Based on this it is naturally to believe that the change in the wake would not be as severe as seen in the results, as least not at $X/D = 1$. However, the turbulence intensity typical for atmospheric turbulence altered the wake structure considerably. The reason for the small change in the power coefficient curves might be that the boundary layer created by the grid, when placed on the floor in front of the turbine, might have disturbed the flow at the tip of the blade closest to the floor, and thus reduced the power extraction in the measurement conducted without grid turbulence.

The study of the meandering of the wake is only possible when the model wind turbine is placed in an incoming flow with low turbulence. This is due to that the method for this study is based on the location of the tip vortices, and the only well-defined vortices were found in the case without grid generated turbulence in the wind tunnel. As seen in Section 5.8, the only clear indication of the three tip vortices is in the case with a low incoming turbulent flow at $X/D = 1$ downstream the turbine. However, it were indications of merged tip vortices at $X/D = 1$ in the case with an incoming flow with turbulence intensity typical for atmospheric turbulence and at $X/D = 3$ in the case with low turbulence intensity. At $X/D = 5$ the wake seems to be fully dissolved in the case with grid generated turbulence. In the case without grid generated turbulence at $X/D = 5$ there seems to be some kind of structure in the wake, based on the congestion in the normal stress seen in the phase averaged measurements. The flow field in the wake at $X/D = 5$ without grid generated turbulence is comparable to the flow field at $X/D = 3$ with grid turbulence, both when considering the structure of the flow field and level of normal stress. The fact that the tip vortices merge together and break up at a faster rate when the incoming flow has higher turbulence intensity corresponds well to the theory. The increased tip speed ratio in the case with grid generated turbulence might also be a contributing reason to the faster recovery of the velocity deficit in the wake due to the increased thrust coefficient of the turbine.

Based on the PSD, the three peaks seen in the normal stress at $X/D = 1$ without grid turbulence, presented both in the phase averaging and from the first five rotations, can be said to represent the tip vortices in the wake. The lack of the 3P frequency in the PSD representing the other measurement points in the wake indicate that the three tip vortices were broken up or merged together at these positions.

Also indicated by the PSD is instability in the tip vortices position, due to the high 2P frequency. The high 2P frequency at $z/R = 1.20$ might indicate that the most unstable tip vortex is the second vortex, or the tip vortex in the middle. Since this measurement point is in the area of the second and third tip vortex, and the 2P frequency is highest at this measurement point, a pulsating motion between these two tip vortices might be the “strongest” compared to a pulsating motion between tip vortex one and two.

The tip vortices found at $X/D = 1$ downstream the turbine in the case where the model wind turbine was placed in an incoming flow with low turbulence, seems to be located relatively stable. When comparing the z/R position of the center of the tip vortices from the phase averaged measurements with the once presented for the five first rotations of the turbine, based on the level of the normal stress in the flow, the deviation varies with a distance from $4.50E-3$ m to $1.80E-2$ m. The first tip vortex, located within the first 100° of rotation, seems to be most stable. When studying the location of the center of the tip vortex directly from the time series, the center seems to be located between $z/R = 1.10$ and $z/R = 1.14$, while in the phase averaged measurements the range is from $z/R = 1.09$ to $z/R = 1.13$. This indicates that the center of the tip vortex tends to move a bit to the left, in a direction closer to the wind turbine rotor, with a distance of $4.50E-3$ m. However, in both Figure 5.2 and Figure 5.27 the peak value in the normal stress, indicating this tip vortex, is located within a narrow range, and the diameter of the tip vortex seems to be in the order of $1.80E-2$ m. This corresponds well to the assumptions conducted after the first measurement with rake 1.

The second tip vortex, located within 100° to 160° of rotation at $X/D = 1$, seems to be a bit more unstable. When presenting the normal stress for only five rotations of the wind turbine, the center seems to be located within $z/R = 1.15$ to $z/R = 1.18$, see Figure 5.5. However, in the third rotation the center is shifted a bit to the right in the figure, to $z/R = 1.17$ to $z/R = 1.20$, which equals a displacement of $9.0E-3$ m. Both ranges indicate a diameter of $1.35E-2$ m of the tip vortex. In the phase averaged measurements the peak value in the normal stress is located between $z/R = 1.09$ and $z/R = 1.20$. This is a much wider range, going from $1.35E-2$ m when studying the location of one rotation, to $4.95E-2$ m when the studying the phase averaged measurements. Thus, the location of the center of the tip vortex seems to move mainly towards the rotor center within the rotations. This indicates that the location of this tip vortex is more unstable than the first tip vortex.

As seen from Figure 5.7 and Figure 5.27, tip vortex number three, located within 190° and 260° of the rotation, seems to be even more unstable. In Figure 5.7 the increased normal stress representing the tip vortex seems to be located between $z/R = 1.235$ and $z/R = 1.260$, though in Figure 5.5 it is located between $z/R = 1.19$ and $z/R = 1.22$. However, none of the two figures seem to capture the whole tip vortex, so an presumption based on Figure 5.5 and Figure 5.7 is that the tip vortex is located between $z/R = 1.19$ to $z/R = 1.26$. In the third rotation in Figure 5.7 the whole tip vortex seems to be captured, with a center located within $z/R = 1.21$ to $z/R = 1.26$. When studying the tip vortex presented by phase averaged measurements, it might seem like the division of the tip vortex seen between Figure 5.5 and Figure 5.7 is caused by the “two parts” of the tip vortex. In other words, the negative fluctuating velocity was captured in Figure 5.5 and the positive in Figure 5.7. However, when comparing the width of the tip vortex found by the phase averaged measurements with the once found for a single rotation, there are deviations in the range of $1.80E-2$ m to the left in the figures, and thus the tip vortex seems to move towards the wind turbine rotor within some of the rotations. The average diameter of the tip vortex seems to be round $2.70E-2$ m based on the normal stress given in Section 5.1.

When comparing the average size of the tip vortices, they seem to be different. The average size of the first tip vortex is $1.80E-2$ m, while the second tip vortex is $1.35E-2$ m. The third tip vortex seems to be in the order of $2.70E-2$ m, which is $9.0E-3$ m wider than the first and $1.35E-2$ m wider than the second vortex.

Based on the comparison given in the previous sections, for the case with an incoming flow with low turbulence at $X/D = 1$, all the tip vortices seem to meander a bit. The meandering is mainly directed towards the rotor center based on the locations seen within the five first rotations. The exact meandering of the tip vortices in the horizontal direction, z , is difficult to state based on the method used to present the measurements in this master thesis. A criterion on level of the normal stress indicating the exact position of the tip vortices is difficult to state, and thus the comparison between the positions of the tip vortices is just an estimate. In the comparison in this section the location of the tip vortices are based on when the normal stress is greater than the mean value for the specific accumulation indicating the vortices.

The fact that all the tip vortices seem to meander mainly towards the rotor center might be caused by the strength in the free stream flow, holding the wake in place. In other words, the strength of the tip vortices is not great enough to “push” the free stream in an outward direction relative to the rotor center, and the instability in the tip vortices cause a meandering motion mainly towards the rotor center. The strength of the tip vortices is unequal when considering the level of the normal stress presented both in the phase averaged results and from the first five rotations. The second tip vortex is the weakest one, while the third is the strongest. The strongest tip vortex, number three, is also the tip vortex that seems to meander most outward from the centerline in the wake when compared to the other two vortices. This corresponds well to the statement that the strength of the vortices has an influence on meandering in outward direction, towards the free stream. It seems that even though the tip vortices are located within the same wake, they tend to meander with different distance, both in the streamwise and horizontal direction. This indicates that the displacement of the tip vortices might not be a correct method of determining if the whole wake of the model wind turbine meanders. It also proves that the displacement of the tip vortices is individual.

One explanation to the unequal strength of the tip vortices might be an unequal lift force acting the blades. This coincides with the assumption of the uncertainty related to the pitch angle of the blades. When changing the pitch angle, the lift force will either increase or decrease, dependent of the angle, which again will change the strength of the vortex. However, a damaged blade will also affect the total lift force acting on the turbine blade.

At $X/D = 3$ downstream the turbine, in the case with an incoming flow with low turbulence intensity, it seems like two of the tip vortices have merged together, due to the two peaks in the normal stress. This corresponds well with the instability seen at $X/D = 1$. Tip vortex two and three seems to be the most unstable, and the fact that these two have merged together at $X/D = 3$ is not unlikely. The high 2P frequency seen at $z/R = 1.20$ is also a good support to this statement.

As seen in Section 5.6, the maximum value of the fluctuating velocity, assumed to represent the center of the tip vortex, is not stable in the streamwise direction. For the two cases chosen to study, $z/R = 1.12$ and $z/R = 1.13$, the maximum fluctuating velocity varied quite frequently within a range of respectively $1.53E-2$ m and $1.28E-2$ m. This is in the same magnitude as the once estimated in the horizontal direction, z .

The instability might indicate variable loads on the turbine blades during the measurements, causing the tip vortex to be shed in a slightly different path. It might also be caused by instability in the tip vortex. The meandering in the streamwise direction corresponds to the high 2P frequency seen in the PSD.

The distribution of the tip vortices within the 360° of rotation was different when studying the phase averaged measurements and the cross correlation based on the location of tip vortex number one. In the phase averaged measurements, the distribution of the vortices were 30° , 128° and 224° , and according to the cross correlation the locations was found to be 36° , 144° and 252° . Since both analyses are based on averaged values, one might expect the vortices to appear at the same location. However, the cross correlation is based on the index value where the maximum u' occurs most frequently. This will be a source of error due to the meandering of the peak. Thus, the distribution of the vortices will not be comparable for these two averages. The only clear observation is that the tip vortices are not equally distributed within the 360° , and are most likely to appear at the distribution given by the phase averaged measurements.

As seen from the results and analysis conducted in this chapter, the tip vortices seems to already have merged together at $X/D = 1$ when the turbine is placed in an incoming flow with turbulence intensity that is typical for atmospheric turbulence. However, there is some congestion of energy indicating a certain structure in the wake at this location. The gap in the normal stress seen in the phase averaged measurements indicate that the tip vortices have caught up with one another, creating a field of increased normal stress in the wake of the turbine. Thus, the grid generated turbulence seems to have an effect which forces the tip vortices to merge together at a faster rate. The fact that the vortices are not equally distributed within the 360° in the wake might make it easier for the vortices to merge together in the turbulent incoming flow. Further downstream the model wind turbine, the wake structure seems to be fully dissolved due to the grid generated turbulence. All these observations correspond well to the theory.

6. Conclusion

It has been conducted a study on wake meandering downstream a horizontal axis model wind turbine in an incoming flow with both low turbulence intensity and turbulence intensity typical for atmospheric turbulence. The experiments were conducted in the wind tunnel at NTNU at the Department *Energy and Process Engineering*. Several initial measurements, including grid geometry calculations and measurements, performance measurements of the model turbine, integral length scale measurements, among other, lead up to a final measurement with four hot-wire probes in the area of the tip vortices in the wake of the turbine. The measurements were conducted at $X/D = 1, 3, \text{ and } 5$ downstream the model wind turbine.

The aim of the experiments was to study the meandering of the wake of the model wind turbine in the two incoming flows. There have been conducted numerous experiments on the wake of wind turbines, and the phenomenon wake meandering, where the wake moves around in space, is a topic of interest for many. The meandering can cause fatigue loads on downstream wind turbines in a wind farm, and the phenomenon has shown difficult to model accurately.

The fact that a wind turbine blade sheds tip vortices, a total of three for a three bladed horizontal axis turbine, which follow the wake of the wind turbine downstream, makes it possible to state if the wake meanders based on the location of the tip vortices. By using an array of four hot-wire probes, simultaneous measurements were conducted at multiple nearby points in the wake, and thus the location of the tip vortices was obtained based on the increased normal stress in the wake.

An incoming flow with turbulence intensity typical for atmospheric turbulence was created by inserting a grid in the inlet to the test section in the wind tunnel. The grid produced a turbulence intensity of round 5.5 % and the integral length scales was found to be $L_{uux} = 6.5E-2$ m and $L_{uuz} = 3.1E-2$ m at $x = 3.75$ m downstream the grid. The tip speed ratio of the model wind turbine was set to 6 in the measurement conducted with an incoming flow with a low turbulence intensity of round 0.3 %, and 7 in the case with a turbulence intensity round 5.5 %.

Well-defined tip vortices were only found at $X/D = 1$ downstream the model wind turbine, when the incoming flow had low turbulence intensity, based on the increased level of normal stress in the wake. The presence of the tip vortices were also confirmed by a 3P frequency in a power spectral density function conducted on chosen time series from the measurements.

At the other measurements points downstream the turbine, phase averaged measurements showed only broad fields with increased normal stress, indicating that the tip vortices had either merged together or broken up. This was also confirmed by a power spectral density function, which lacked the 3P frequency. In the case with an incoming flow with turbulence intensity typical for atmospheric turbulence, the tip vortices seemed to already have merged together at $X/D = 1$ downstream the turbine.

The phase averaged measurements showed a field in the wake with increased normal stress, with only one gap with almost no normal stress, throughout the 360° in the wake. Thus, the increased turbulence intensity in the incoming flow forced the tip vortices to merge together at an earlier stage downstream the model wind turbine compared to an incoming flow with low turbulence intensity. This corresponds well to previous observations and theory. Though, it was not assumed that they would merge together at such an early stage downstream the turbine. This was likely due to an unequal distribution of the tip vortices and that the turbulent flow smeared out the energy in the wake by diffusion and mixing.

The strength and size of the tip vortices, based on the normal stress at $X/D = 1$ without grid generated turbulence in the wind tunnel, were found to be unequal. This is likely caused by different loading and/or different pitch angles of the turbine blades, which resulted in a different transport velocity of the vortices and that they followed their own path in the wake. The result of this was clearly seen in the phase averaged measurement, where the distribution of the vortices within the 360° of rotation was unequal. The location of the vortices was found to be at 30° , 128° and 224° from the phase averaged measurements. The diameters of the three tip vortices were found to be in the order of $1.80E-2$ m, $1.35E-2$ m and $2.70E-2$ m respectively. The weakest tip vortex was found to be the one in the middle, and the strongest tip vortex was the one with the greatest diameter.

The tip vortices located at $X/D = 1$ without grid generated turbulence seemed to meander a bit back and forth, with a distance from $4.50E-3$ m to $1.80E-2$ m in the horizontal direction, z , though mainly towards the rotor center. However, the exact meandering of the tip vortices in the horizontal direction is difficult to state based on the method used to present the measurements in this master thesis. A criterion on level of the normal stress indicating the exact position of the tip vortices is difficult to state, and thus the comparison between the positions of the tip vortices is just an estimate.

In the PDS a 2P frequency indicated a pulsating motion between the tip vortices within the rotations. A study on the location of the peak in the normal stress in the streamwise direction, x , believed to represent one of the tip vortices, also indicated a meandering of the tip vortex. The peak value varied within a total distance of $6.17E-2$ m between the rotations measured in one time series. The 2P frequency was highest at $z/R = 1.20$, indicating that the pulsating motion might be strongest between tip vortex two and three, with coincides with the strength and a merging of two tip vortices at $X/D = 3$ in the low turbulent incoming flow.

Even though the tip vortices are located within the same wake, they tend to meander with a different distance, both in the streamwise and horizontal direction. This indicates that the displacement of the tip vortices might not be a foolproof method of determining if the whole wake of the model wind turbine meanders. It also proves that the meandering of the tip vortices is individual.

At $X/D = 3$ downstream the turbine, in the case with an incoming flow with low turbulence intensity, it seemed like two of the tip vortices had merged together. While at $X/D = 5$ for the same case, the vortices seemed to create only a continuous field with increased normal stress.

The turbulent kinetic energy in the wake was clearly smeared out when comparing the measurements conducted with and without grid turbulence. The energy in the incoming turbulent flow was thus high enough to affect the flow in the wake and cause the tip vortices to merge together.

7. Further work

Due to lack of time, a correct and thorough (or foolproof) method of studying the meandering of the tip vortices in the horizontal direction, z , was not obtained in this study. In a later study a method of locating the tip vortices within the rotations in the time series needs to be established. In a selected data set there will always be a maximum value for each measurement point, or index, in the set. A way to find the area of where the tip vortices are within this data set, and to see if this area moves from one hot-wire probe to another might be a way to conduct such a study. It then needs to be established a criterion of locating this area in a way to be sure that it just represented the tip vortex. If such a criterion could be found, the meandering can be studied thorough. Based on this, a histogram can be made as to where the tip vortices are located within the range measured by the hot-wire probes within the rotations.

Since the tip vortices seem to be of different size and strength, and are unequal distributed within the 360° in the wake of the turbine, the fine tuning of the pitch angle on the blades prior to the experiment, should be conducted even more carefully. The model wind turbine blades should also be examined even more closely to see if there is any damage on the blades causing the tip vortices to be shed unequal.

Due to the significant change in the wake structure at $X/D = 1$ when the model wind turbine was placed in an incoming flow with a turbulence intensity typical for atmospheric turbulence, new measurements should be conducted closer to the rotor of the turbine. This way the meandering of the wake can be studied and compared for the two incoming flows. The measurements should also be conducted with more than four hot-wire probes to be sure to cover the entire range over where the tip vortices are located. It is shown that an integral length scale L_{uux} as short as $6.5E-2$ m and $L_{uuz} = 3.1E-2$ m are sufficient to affect the behavior of the wake. If it is long enough to make the whole wake meander will be remained to see at a later time.

The use of more than 4 hot-wires probes will also increase the resolution in the analysis. This way the cross correlation based on the single tip vortex can be used to find the angle of which the tip vortices travel downstream in the wake and further comparing this to the one found by using the velocity triangle and/or the tip speed ratio of the turbine. A velocity difference between the wake, or tip vortices, and the free stream velocity may also be found if a cross correlation with a higher resolution is obtained.

A study on the meandering of the two other vortices in the streamwise direction, x , should also be conducted. This might confirm the assumption that the high 2P frequency seen in the PSD is caused by a pulsating motion between the vortices, and that the motion is strongest between tip vortex two and three.

When conducting new measurement the grid should be taken out of the wind tunnel and not be placed on the floor in front of the model turbine during the measurements.

Bibliography

1. REN21, *REN21 Renewables 2012, Global Status Report*, in *REN212012*: Paris: REN21 Secretariat.
2. Vermeer, L.J., J.N. Sørensen, and A. Crespo, *Wind turbine wake aerodynamics*. Progress in Aerospace Sciences, 2003. **39**(6–7): p. 467-510.
3. Medici, D. and P.H. Alfredsson, *Measurements on a wind turbine wake: 3D effects and bluff body vortex shedding*. Wind Energy, 2006. **9**(3): p. 219-236.
4. Medici, D. and P.H. Alfredsson, *Measurements behind model wind turbines: further evidence of wake meandering*. Wind Energy, 2008. **11**(2): p. 211-217.
5. España, G., et al., *Spatial study of the wake meandering using modelled wind turbines in a wind tunnel*. Wind Energy, 2011. **14**(7): p. 923-937.
6. Aubrun, S., et al., *Comparison between Wind Tunnel and Field Experiments on Wind Turbine Wake Meandering*, in *Progress in Turbulence and Wind Energy IV*, M. Oberlack, et al., Editors. 2012, Springer Berlin Heidelberg. p. 223-226.
7. Ainslie, J.F., *Calculating the flowfield in the wake of wind turbines*. Journal of Wind Engineering and Industrial Aerodynamics, 1988. **27**(1–3): p. 213-224.
8. J. F. Manwell, J.G.M., A. L. Rogers, *Wind Energy Explained*. Second edition ed. 2010: John Wiley & Sons Ltd.
9. J. H. Ferziger, M.P., *Computational Methods for Fluid Dynamics*. Third Edition ed.: Springer.
10. T. Burton, D.S., N. Jenkins, E. Bossanyi, *Wind Energy Handbook*. 2001: John Wiley & Sons, Ltd.
11. Wyngaard, J.C., *Atmospheric Turbulence*. Annual Review of Fluid Mechanics, 1992. **24**(1): p. 205-234.
12. Panofsky, H.A., *The Atmospheric Boundary Layer Below 150 Meters*. Annual Review of Fluid Mechanics, 1974. **6**(1): p. 147-177.
13. J. John, B., *Aerodynamics for engineers*. 1. edition ed. 2009: Pearson Prentice-Hall.
14. White, F.M., *Viscous fluid flow*. 1991: McGraw-Hill Professional Publishing.
15. Counihan, J., *Adiabatic atmospheric boundary layers: A review and analysis of data from the period 1880–1972*. Atmospheric Environment (1967), 1975. **9**(10): p. 871-905.
16. Krogstad, P.-Å., *About the NTNU model turbine data base and the two blind tests*, 2011, NTNU: The Norwegian University of Science and Technology, Trondheim, Norway.
17. Pope, S.B., *Turbulent flows*. 2000, New York: Cambridge University Press.
18. Krogstad, P.-Å., *Personal conversation*, 2013: NTNU.
19. Stoica, P. and R.L. Moses, *Introduction to spectral analysis*. 1997: Prentice Hall.
20. Sanderse, B., *Aerodynamics of wind turbine wakes*. Energy Research Center of the Netherlands (ECN), ECN-E-09-016, Petten, The Netherlands, Tech. Rep, 2009.
21. Verneer, N.-J., *How big is a tip vortex?*, 1996, Institute for Wind Energy, Faculty of Civil Engineering, Delft University of Technology.
22. Sanderse, B., *Aerodynamics of wind turbine wakes*, ECN.
23. Medici, D., *Experimental Studies of Wind Turbine Wakes - Power Optimisation and Meandering*, 2005, Royal Institute of Technology: Stockholm, Sweden.

24. España, G., et al., *Wind tunnel study of the wake meandering downstream of a modelled wind turbine as an effect of large scale turbulent eddies*. Journal of Wind Engineering and Industrial Aerodynamics, 2012. **101**(0): p. 24-33.
25. T. Arts, H.B., J.-M. Buclin, M. Carbonaro, G. Degrez, R. Dénos, D. Fletcher, D. Olivari, M.L. Riethmuller and R.A. Van den Braembussche, *Measurement techniques in fluid dynamics, An introduction*. 2nd revised edition ed. 2004: von Karman Institute for Fluid Dynamics.
26. Somers, D.M., *The S825 and S826 airfoils*. National Renewable Energy Laboratory, Subcontractor Report, 2005.
27. Sæta, E., *The Blade Element Momentum Method*, 2008: NTNU.
28. Krogstad, P.-Å. and M.S. Adaramola, *Performance and near wake measurements of a model horizontal axis wind turbine*. Wind Energy, 2012. **15**(5): p. 743-756.
29. NTNU, I. *The closed return wind tunnel*. 31.05.2012]; Wind tunnel description]. Available from: <http://www.iyt.ntnu.no/mekanikk/Vindtunell.htm>.
30. Suzlon, *S64 Mark II & S66 Mark II - 1.25 MW*, 2010, Suzlon: Suzlon.com.
31. Türk, M. and S. Emeis, *The dependence of offshore turbulence intensity on wind speed*. Journal of Wind Engineering and Industrial Aerodynamics, 2010. **98**(8-9): p. 466-471.
32. Bracchi, T., *Private conversation*, 2012, Ph.D. Student: NTNU.
33. Eriksen, P.-E., *Personal conversation*, 2013: NTNU.
34. Krogstad, P.-Å. and P.E. Eriksen, *"Blind test" calculations of the performance and wake development for a model wind turbine*. Renewable Energy, 2013. **50**(0): p. 325-333.
35. Anthony J. Wheeler, A.R.G., *Introduction to Engineering Experimentation*. Third edition ed. 2010: Prentice Hall

A. Appendix

A.1 Calibration data

A.1.1 Thrust gauge

The offset for the thrust gauge was -5.732 V, and it was used a gain of 4 on the amplifier. The measurements for the calibration are given in Table A.1, and the calibration curve is given in Figure A.1.

Table A.1: Calibration data for thrust gauge

Weight [g]	Temp [°C]	Voltage [V]	delta V [-]	Thrust [N]
0	20.52	-5.732	0.000	0.000
460	20.54	-5.187	0.545	4.513
960	20.56	-4.603	1.129	9.418
1460	20.56	-4.016	1.716	14.323
1960	20.54	-3.429	2.303	19.228
2460	20.54	-2.848	2.884	24.133
3460	20.55	-1.674	4.058	33.943
4460	20.56	-0.498	5.234	43.753
5460	20.52	0.832	6.564	53.563
7460	20.53	3.081	8.813	73.183
9460	20.54	5.397	11.129	92.803
7460	20.53	3.145	8.877	73.183
5460	20.57	0.864	6.596	53.563
4460	20.57	-0.482	5.250	43.753
3460	20.56	-1.598	4.135	33.943
2460	20.56	-2.726	3.006	24.133
1960	20.54	-3.377	2.355	19.228
1460	20.54	-3.940	1.793	14.323
960	20.57	-4.535	1.197	9.418
460	20.60	-5.136	0.597	4.513
0	20.59	-5.708	0.024	0.000

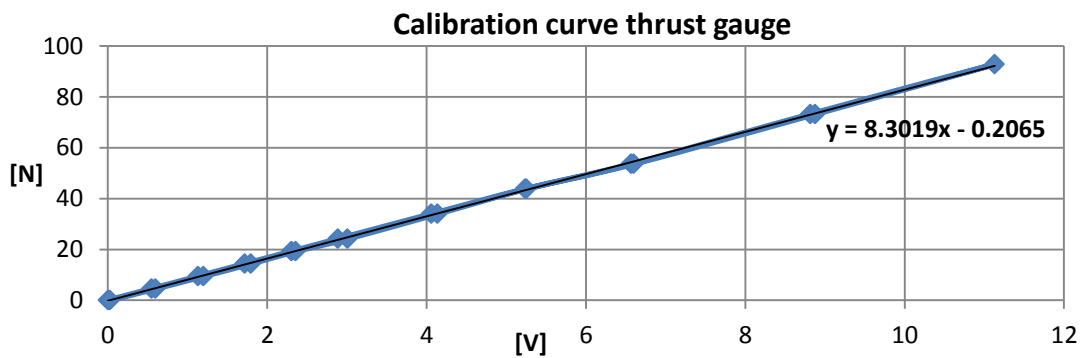


Figure A.1: Calibration curve for thrust gauge

The calibration coefficient for the thrust gauge was 8.3019 N/V.

A.1.2. Torque gauge

The offset value for the torque gauge was 7.033 V, and it was used no gain, or $G = 1$, on the amplifier. The calibration data is given in Table A.2 and the calibration curve is given in Figure A.2.

Table A.2: Calibration data for torque gauge

Wight [g]	Temp [°C]	Torque [V]	Delta V	Moment
0	20.10	7.033	0.000	0.000
16	20.09	6.862	-0.171	0.068
66	20.14	5.939	-1.093	0.282
116	20.13	5.013	-2.020	0.496
166	20.13	3.790	-3.243	0.709
216	20.16	2.735	-4.298	0.923
266	20.15	1.539	-5.494	1.136
316	20.16	0.784	-6.249	1.350
416	20.18	-1.444	-8.477	1.777
516	20.19	-3.587	-10.620	2.204
616	20.17	-5.525	-12.558	2.632
516	20.17	-3.623	-10.655	2.204
416	20.20	-1.449	-8.482	1.777
316	20.19	0.276	-6.756	1.350
266	20.18	1.448	-5.585	1.136
216	20.16	2.586	-4.446	0.923
166	20.18	3.737	-3.295	0.709
116	20.15	4.632	-2.401	0.496
66	20.19	5.758	-1.274	0.282
16	20.19	6.706	-0.327	0.068
0	20.19	6.968	-0.064	0.000

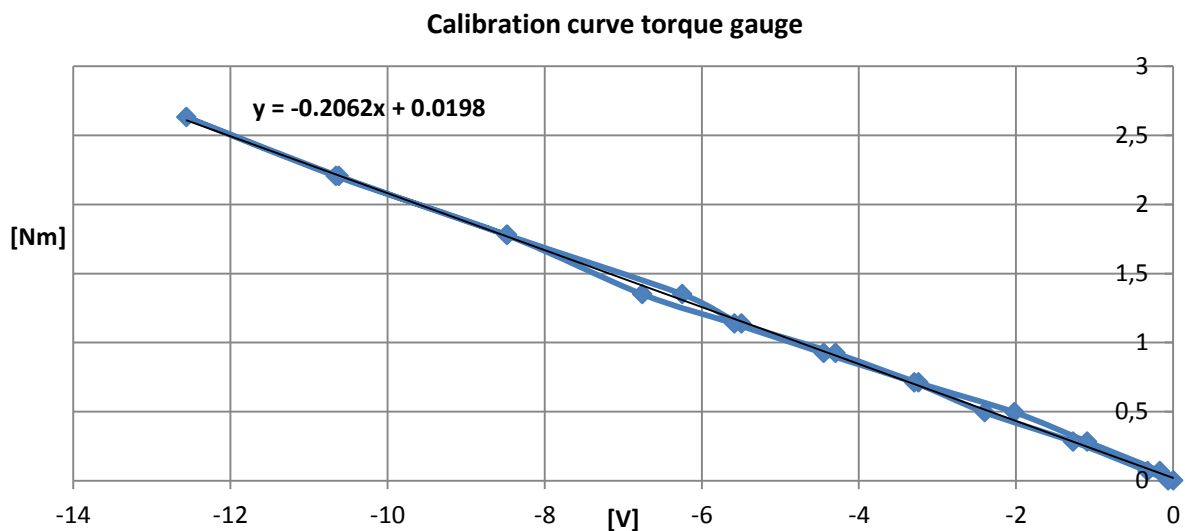


Figure A.2: Calibration curve for torque gauge

The calibration coefficient for the torque gauge was -0.2062 Nm/V .

A.1.3. Pressure transducer Pitot probe

Gain = 5 was used on the amplifier connected to the pressure transducer. The calibration was conducted in an empty wind tunnel and with the use of a inclined manometer. The data for the calibration is given in Table A.3 and the calibration curve is given in Figure A.3.

Table A.3: Calibration data for pressure transduces Pitot probe

RMP Wind tunnel	Temp [°C]	ρ [kg/m ³]	mm [Pa]	dp	V [V]	Delta V	U [m/s]
0	23.492	1.1935	0	0.0	-9.205	0	0
100	23.873	1.1920	20	4.0	-8.870	0.335	2.591
200	24.155	1.1909	85	17.0	-7.840	1.368	5.343
300	24.463	1.1896	195	39.0	-6.048	3.157	8.097
380	24.748	1.1885	317	63.4	-4.128	5.077	10.330
404	24.918	1.1878	359	71.8	-3.463	5.741	10.995
500	25.230	1.1866	550	110.0	-0.381	8.824	13.616
600	25.363	1.1860	795	159.0	3.558	12.763	16.374
700	24.830	1.1882	1085	217.0	8.230	17.434	19.112

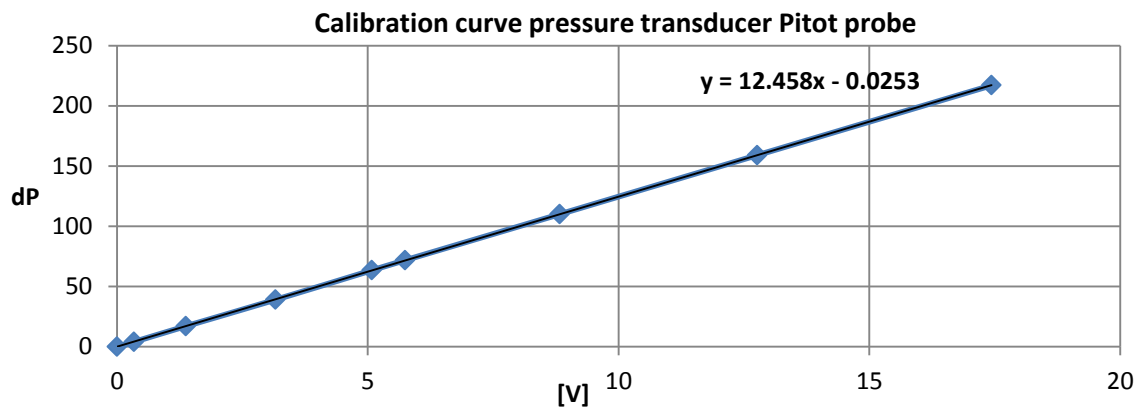


Figure A.3: Calibration curve for the pressure transducer Pitot probe

The calibration coefficient for the pressure transducer using a Pitot probe was 12.458 Pa/V.

This is the calibration used to find the correlation between the velocities calculated based on the values given by the contraction and the free stream velocity at $x = 3.75$ m downstream the inlet to the test section.

A.1.4. Pressure transducer contraction

Gain = 5 was used on the amplifier connected to the pressure transducer. The calibration was conducted in an empty wind tunnel. The data for the calibration is given in Table A.4 and the calibration curve is given in Figure A.4.

Table A.4: Calibration data for the pressure transducer for contraction in the wind tunnel

RPM wind tunnel	Temp [°C]	ρ [kg/m ³]	mm [Pa]	dP	V [V]	Delta V	U [m/s]	Ratio [-]
0	23.73	1.193	0	0.0	-9.158	0	0	
100	24.06	1.191	20	4.0	-8.834	0.323	2.662	1.028
200	23.94	1.192	81	16.2	-7.873	1.285	5.357	1.003
300	23.99	1.192	192	38.4	-6.267	2.890	8.248	1.019
380	24.25	1.190	295	59.0	-4.514	4.644	10.230	0.990
404	24.40	1.190	331	66.2	-3.926	5.231	10.837	0.986
500	24.93	1.188	510	102.0	-1.177	7.981	13.464	0.989
600	25.75	1.184	720	144.0	2.1862	11.344	16.020	0.978
700	26.95	1.180	978	195.6	6.1693	15.327	18.708	0.979

The ratio given in the table is the ratio between the velocity given by the contraction divided by the velocity given by the Pitot probe at $x = 3.75$ m downstream the inlet to the test section in the wind tunnel. At free stream velocity of 10.23 m/s the ratio between the velocities are $U_{x=3.75} = U_{\text{ref_cont}} / 0.99$.

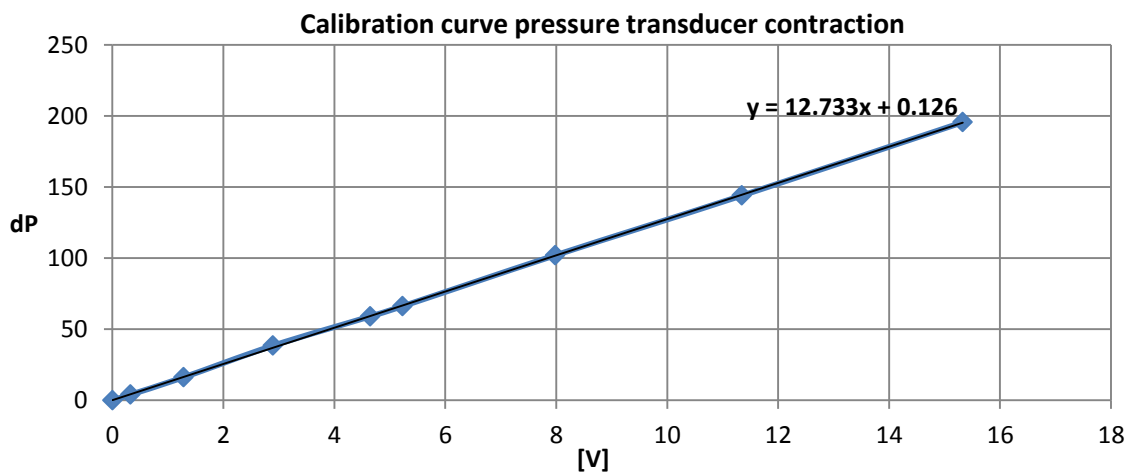


Figure A.4: Calibration curve for the pressure transducer for the contraction of the wind tunnel

The calibration coefficient for the pressure transducer for the contraction was 12.733 Pa/V.

It was also conducted measurements of the velocities given by the contraction of the wind tunnel and the Pitot probe located at $x = 3.75$ m with the grid installed in the inlet section. This gave the ratio; $U_{x=3.75} = U_{\text{ref_cont}} / 1.15$.

A.1.5. Hot-wire anemometry

Due to the numerous calibrations of hot-wire probes, and that the probes need to be calibrated every hour, only one of the calibration curves are shown in the appendix. It illustrates how the velocity and the voltage signal are correlated.

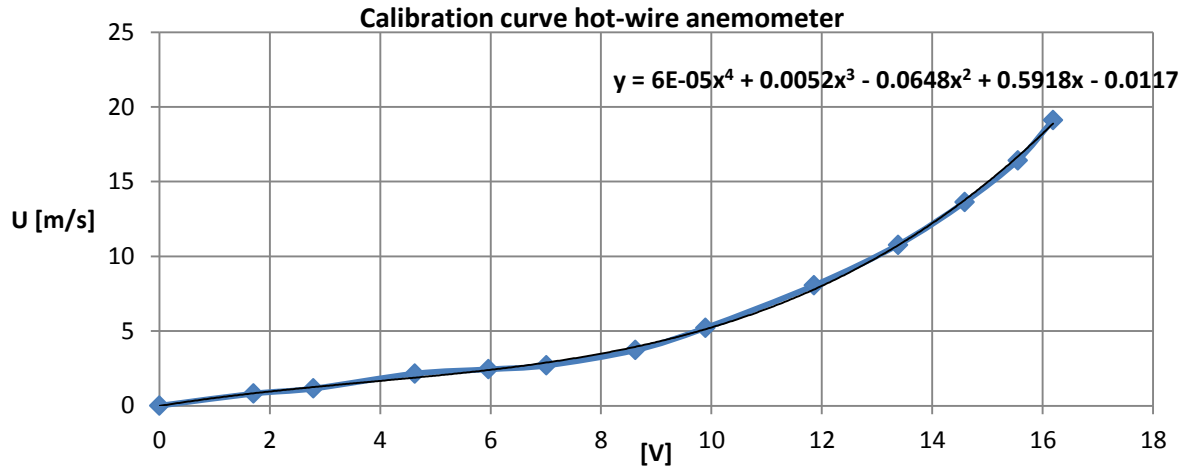


Figure A.5: Calibration curve for hot-wire probe

The calibration is done by using a Pitot probe to measure the mean velocity, and then finding the correlation between the acquiring voltage from the hot-wire probe and the mean wind speed.

The four calibration coefficients are given in the figure. As can be seen, this is a four degree polynomial. The probe is, as seen from the curve, more sensitive to low velocities.

The gain used on the amplifier, which was included in the anemometers, varied from $G = 12$ to $G = 16$ for the different hot-wire probes.

A.2. Comparison normal stress

A comparison between the phase averaged normal stress and the time averaged normal stress was conducted to make sure that the phase averaging of the measurements conducted in Matlab was correct. The values given in the figures from the phase averaging is not normalized, thus the level in of the normal stress between the two averages are not correct. However, the shape of the curves correlates well as seen Figure A.6 to Figure A.17.

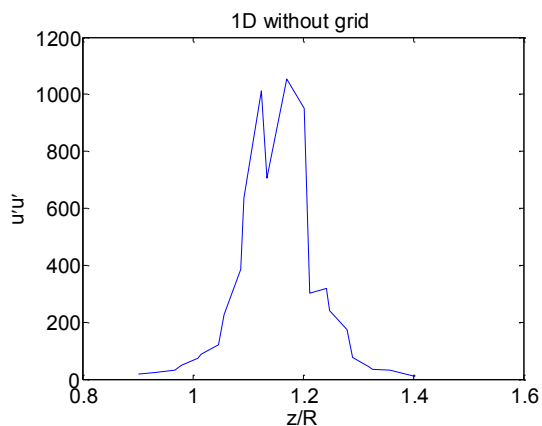


Figure A.6: Normal stress at $X/D = 1$ without grid turbulence, phase averaged

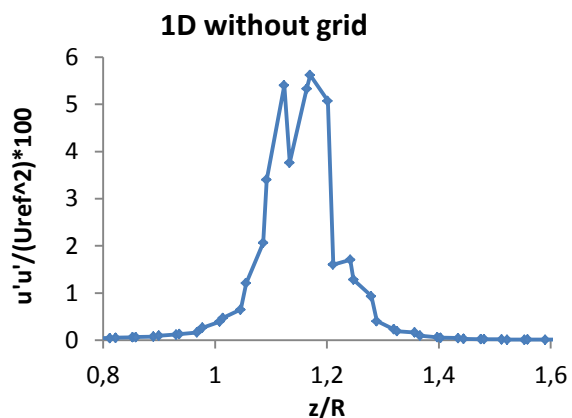


Figure A.7: Normalized normal stress at $X/D = 1$ without grid turbulence, time averaged

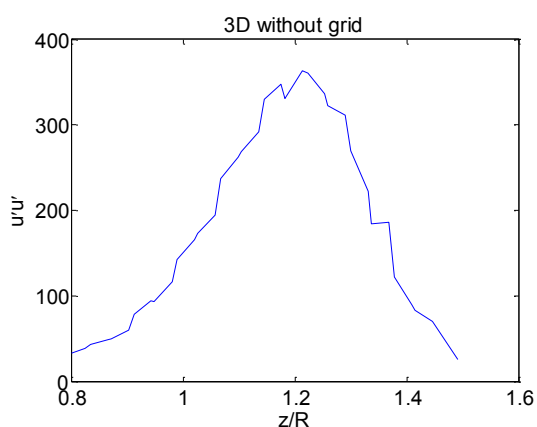


Figure A.8: Normal stress at $X/D = 3$ without grid turbulence, phase averaged

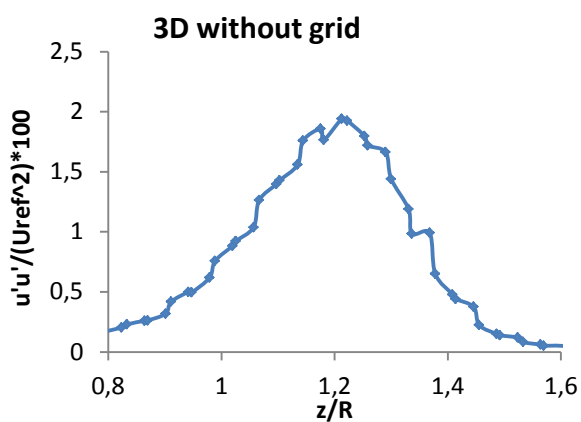


Figure A.9: Normalized normal stress at $X/D = 3$ without grid turbulence, time averaged

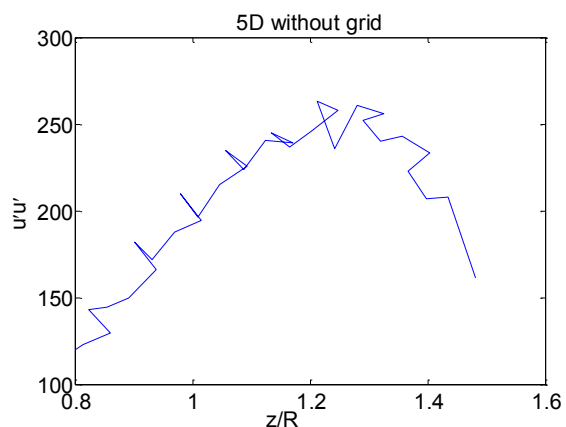


Figure A.10: Normal stress at $X/D = 5$ without grid turbulence, phase averaged

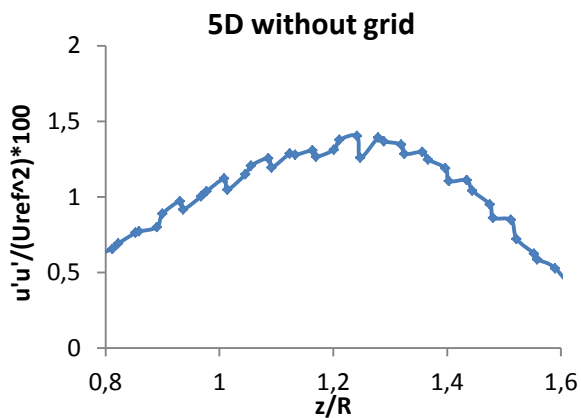


Figure A.11: Normalized normal stress at $X/D = 5$ without grid turbulence, time averaged

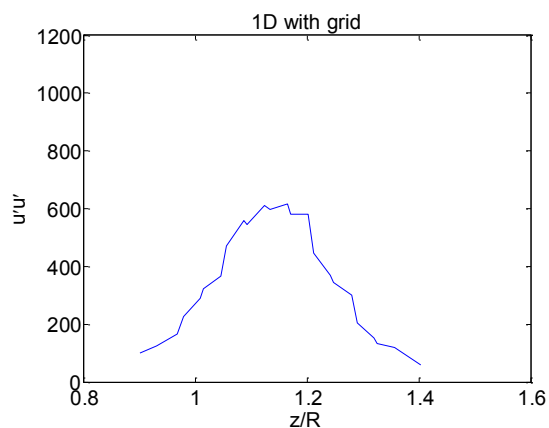


Figure A.12: Normal stress at $X/D = 1$ with grid turbulence, phase averaged

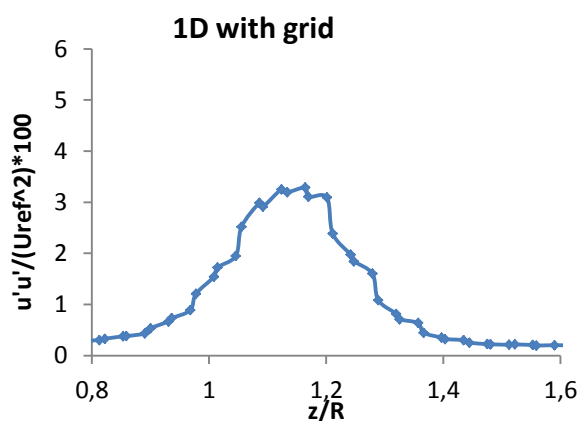


Figure A.13: Normalized normal stress at $X/D = 1$ with grid turbulence, time averaged

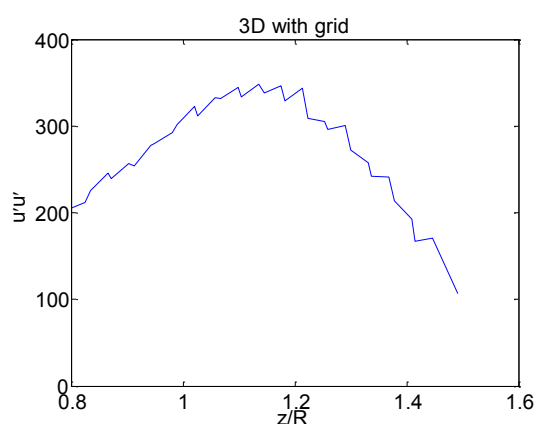


Figure A.14: Normal stress at $X/D = 3$ with grid turbulence, phase averaged

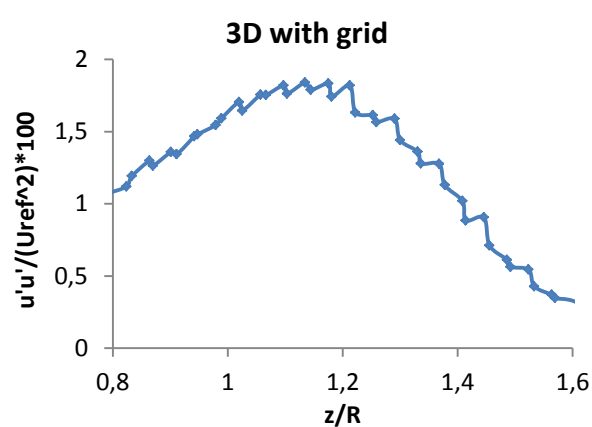


Figure A.15: Normalized normal stress at $X/D = 3$ with grid turbulence, time averaged

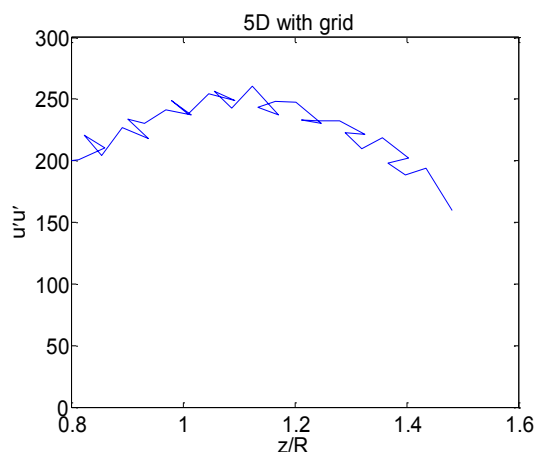


Figure A.16: Normal stress at $X/D = 5$ with grid turbulence, phase averaged

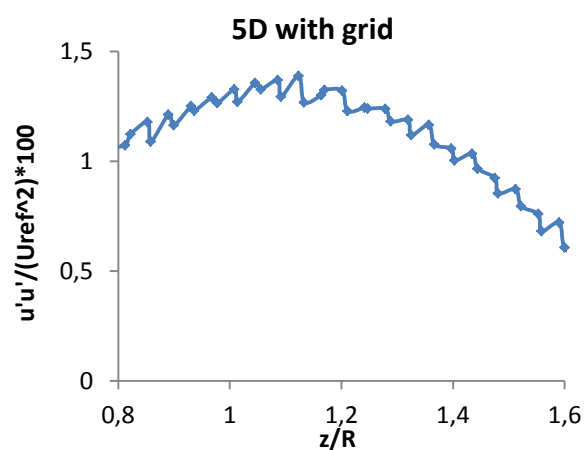


Figure A.17: Normalized normal stress at $X/D = 5$ with grid turbulence, time averaged

A.3. Uncertainty calculations

During the experiment conducted to find the performance characteristics of the model wind turbine, both the mean values and the standard deviations (rms) of the different scalars were measured. These values were used to calculate the random errors during the experiment.

The estimate for the total uncertainties for the measurements conducted to calculate the power coefficient are computed with the root of the sum of squares (RSS) formula given by Equation 1;

$$\omega_x = \sqrt{B_x^2 + P_x^2} \quad \text{Equation 1}$$

where B is the systematic uncertainties, or the so called bias, and the P is the random uncertainties, which are also called precision or probabilistic errors. The random uncertainty was calculated for the pressure (venturi), rotational speed and torque based on the RMS values obtained from the measurements with a confidence interval of 95 % and the t-distribution. The random uncertainties in the temperature and density measurements were neglected since they were relatively constant throughout the experiments. The systematic uncertainties for the torque, thrust and pressure transducer for the contraction were found from calibration by using the maximum deviations between the measured points and the fitting curve of the calibrations. The systematic error in the RPM measurement was neglected due to lack of information. Finally, the uncertainties were combined to find the uncertainty for the wind speed and C_p by the RSS formula given by Equation 2;

$$\omega_R = \left(\sum_{i=1}^n \left[\omega_{xi} \frac{\partial R}{\partial x_i} \right]^2 \right)^{\frac{1}{2}} \quad \text{Equation 2}$$

[35]

A.4. Fully developed pipe flow measurements

As a learning step and introduction to the use of hot-wire anemometry, it was conducted hot-wire measurements on a fully developed pipe flow. It was executed two different measurements on the same flow; one with the hot-wire probe in horizontal direction, and one with the probe in the vertical direction. The measurements were compared to previous measurements conducted on the same flow, which are validated measurements and used as the correct properties of the flow.

The dimension of the pipe was 0.186 m. The conditions during the measurements and the properties used in the calculations are given in Table A.5.

Table A.5: Properties for the measurement in the fully developed pip flow

Property	Horizontal	Vertical
v [m²/s]	1.45E-05	1.45E-05
U=Q/A [m/s]	7.57E+00	8.05E+00
ReD [-]	9.71E+04	1.03E+05
Cf [-]	4.48E-03	4.41E-03
u* [-]	3.58E-01	3.78E-01
u*(used) [-]	3.73E-01	3.78E-01
y correction [-]	-1.50E+00	7.00E-01
τ_w [-]	1.52E-01	1.69E-01
u* corr [-]	1.50E-02	0.00E+00

In Figure A.18 to Figure A.21 the results are compared to the previous measurement conducted on the pipe flow. The values are normalized to be able to compare the measurements.

Figure A.18 shows the normalized velocity profile in the pipe. As seen in the figure, there is a good coherence between the previous measurements, known as the correct measurements, and the once conducted during this master thesis.

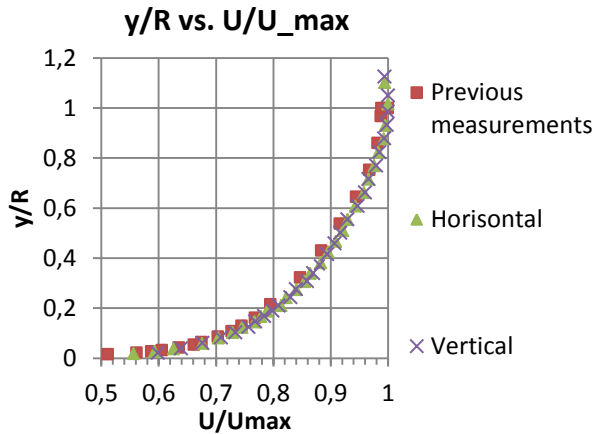
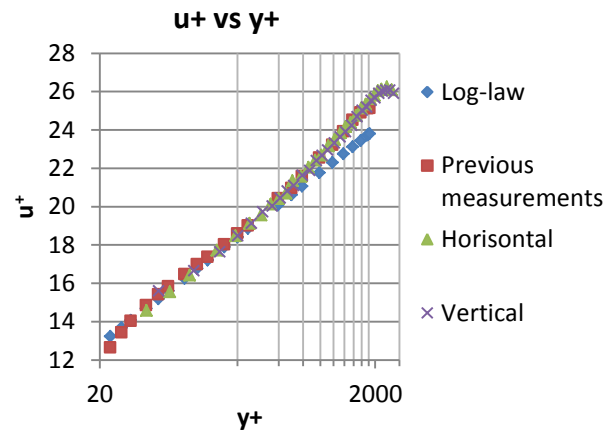
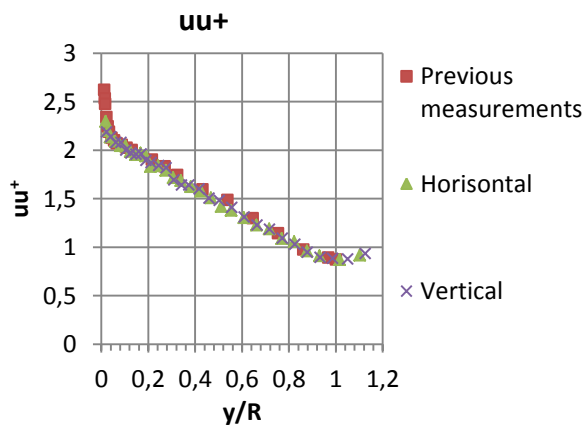
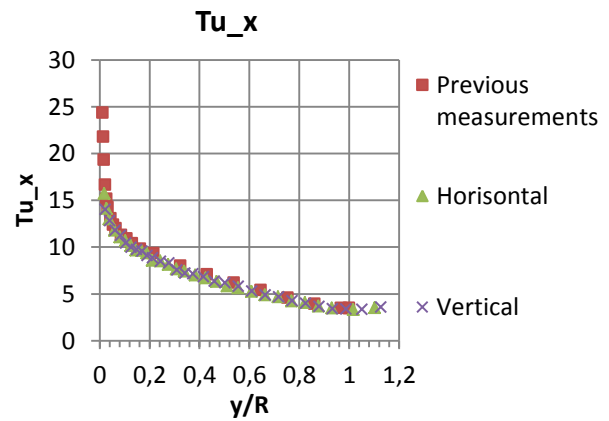


Figure A.18: Normalized velocity profile

Figure A.19: u^+ versus normalized y coordinateFigure A.20: Normalized normal stress as a function of y/R Figure A.21: Turbulence intensity based on the friction velocity as a function of y/R

In Figure A.19 the dimensionless velocity u^+ is plotted versus the wall coordinate y^+ together with the log law. The figure shows that there is a good coherence between both the previous measurements and the measurements conducted with the probe directed both vertical and horizontal, and with the log law up to round $y^+ = 600$.

Figure A.20 shows the normalized normal stress given by Equation 3;

$$uu^+ = \sqrt{\frac{u'u'}{u_*^2}} \quad \text{Equation 3}$$

The figure shows that there is a good coherence between the measurements conducted previously and the once conducted during this master thesis.

Figure A.21 gives the turbulence intensity, based on the friction velocity, as a function of y/R , and is calculated by the use of Equation 4;

$$Tu_x = \sqrt{\frac{u'u'}{u_*^2}} * 100$$

Equation 4

Also in this figure there is a good coherence between the measurements conducted earlier and the once conducted during this master thesis.

As seen from the figures, the measurements coincide well with the previous measurement conducted on the same flow.

A.6. Risk assessment of laboratory setup and experiment

Before initiating the experiments in the wind tunnel, an internet based safety course named *NTNU-SINTEF- Helse, miljø og sikkerhet i laboratorier* and a guided tour of the fluid dynamics lab was accomplished. By completing this, I was approved as an operator of the experimental setup. The setup of the experiment has been risk evaluated and is approved of the leader at the institute.